Master's Thesis

Development and First Deployment of an Innovative Airborne δ^{13}C(CH_4) In Situ Measurement Setup

Entwicklung und erster Einsatz eines innovativen, luftfahrtgestützten in situ δ^{13}C(CH_4) Messverfahrens

Department of Physics
Ludwig-Maximilians-Universität München
in cooperation with the
Institute of Atmospheric Physics
of the German Aerospace center (DLR)

Paul Waldmann

Munich, 29.12.2022

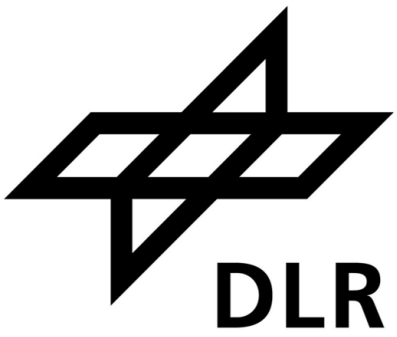

Submitted in partial fulfillment of the requirements for the degree of M. Sc.
Supervised by Prof. Dr. Martin Dameris
Advisor (DLR): Dr. Alina Fiehn

Abstract

This thesis introduces an innovative in situ airborne system for the measurement of the stable carbon isotope ratio of methane emitters, called MIRACLE (measurement of **m**ethane stable carbon **i**sotope **r**atio by **a**irborne implementation of a **c**avity ring down **l**as**e**r spectrometer). A conventional Picarro greenhouse gas analyser was used for the measurement of methane and the methane carbon isotope ratio aboard the research aircraft HALO during the CoMet 2.0 Arctic campaign. Precise $\delta^{13}C(CH_4)$ measurements were achieved by the supplement of a new type of sample collector to the analyser, which makes it possible to take up to six gas samples in a short time, for an extended period of subsequent analysis. The extended measurement period allows analysis with a $\delta^{13}C(CH_4)$ 1σ uncertainty of 0.34 ‰ aboard the aircraft. The MIRACLE instrument was tested for contamination of the samples but showed no distortion of the methane concentration or the isotope ratio. For two of the successful research flights of the campaign, the isotopic signatures of the target areas were analysed using the data of MIRACLE, in order to highlight the measurement uncertainties of the instrument and to discuss the results in the context of the literature. The $\delta^{13}C(CH_4)$ signature of the lake Winnipeg wetland area was found to be -61.95 $\pm$ 2.56 ‰, which is in accordance with comparable studies. The $\delta^{13}C(CH_4)$ signature of a biomass burning fire plume was found to be -35.33 $\pm$ 8.58 ‰, also consistent with the literature. The MIRACLE instrument combines the advantages of high precision $\delta^{13}C(CH_4)$ measurements, which were previously only possible under stable laboratory conditions, with the in situ, real time data analysis and large-scale sampling of secluded areas, due to the airborne deployment.

Contents

1 Motivation

Counteracting the global temperature rise as a consequence of climate change is probably the most challenging task of the 21st century. This can be implemented by greenhouse gases (GHG) emission reduction in sectors such as energy, transport, buildings, industry, waste management, agriculture, forestry and via feedback mechanisms this also influences natural GHG emitters. Therefore it is tangent to almost every facet of our life, as it demands political courage, social acceptance, technical innovation, individual rethinking and sometimes personal renunciation to achieve these decline in GHG emissions. All these goals are based on profound scientific understanding and observation of the underlying physical processes of climate change and in particular the role of GHGs. The aim of the presented work is, to contribute to this understanding by introducing a new airborne GHG measurement setup.
Besides carbon dioxide (CO_2), methane (CH_4) is the second most important anthropogenic greenhouse gas, responsible for an estimated global mean surface temperature rise of roughly 0.3°C since 1750, which is more than 20% of the overall warming. Therefore the analysis of methane emission processes are of major scientific interest, and as a part of this, it is essential to determine the methane producing sources, whether they are anthropogenic or natural, and their respective trends. The ratio of the carbon isotopes ^{12}C and ^{13}C contained in atmospheric methane provides information on the origin of CH_4. There are three main methane producing pathways, biogenic produced methane, thermogenic and pyrogenic. Each of them with specific amounts of the heavier and the lighter carbon isotope.
Thus, the methane carbon isotope ratio offers a possibility to determine whether methane enhancements are due to, e.g. wetland, livestock, fossil fuel or biomass burning emissions. In addition to local source attribution, the long-term trend in isotope ratio can also be used to infer past, present, and by extrapolation, future globally significant methane emitters. In this way, actions for methane emission reduction in specific sectors can be tested for their effectiveness. Besides that, climate models are better constrained in their global methane budgets when accounting for the methane carbon isotope ratio. As only 1.11% of atmospheric methane includes the ^{13}C atom, and differences in the isotopic signature are small, sensitive detectors are necessary for the analysis. Apart from mass spectrometry, modern cavity ring down systems, based on infrared absorption technique, can also be used to determine the isotopic signature. The latter one was used to perform first airborne measurements of methane carbon isotope ratios during the CoMet 2.0 Arctic campaign, a program to study the distribution and variability of carbon dioxide and methane in the arctic. To take advantage of the analyzer's high measurement precision, it was supplemented with an innovative sampler unit. The thesis starts with an introductory chapter on sources and sinks of atmospheric methane, as well as the importance of methane as a greenhouse gas. Chapter 2.2 presents the basics of methane carbon isotope ratio in the context of the different methane emitters and the corresponding trend. Chapter 3 gives a short outline of the CoMet 2.0 campaign, in the course of which the measurements took place. The characterization and performance of the instrument and the development of the sampler unit are described in Chapter 4. In Chapter 5 the data of two selected research flights are analysed for their isotopic signature, including estimation of error ranges and the discussion in context of literature. The last chapter summarises the results and presents an comparison with other airborne measurements of the methane carbon isotope ratio and possibilities for improvement of MIRACLE.

2 Atmospheric Methane

2.1 Methane as a greenhouse gas

This chapter provides an introduction to the relevance of methane as a greenhouse gas and an overview of its sources and sinks.

2.1.1 Climate impact of Methane

Methane absorbs in the infrared wavelength regime, with the 7.6 μm peak accounting for over 98 % of the total absorption. It also absorbs incoming solar radiation, in it's near infrared absorption lines around 1.7, 2.3 and 3.3 μm (Byrom and Shine, 2022).Therefore it affects the radiative forcing (RF), which is the change in the energy flux through the earth's atmosphere, thus a measure for the climate impact. Quantitatively the methane RF is found to be 0.54 W/m² (IPCC AR6 Working Group I, 2021) and therefore contributes to a global surface air temperature increase of 0.28 °C with respect to the time period since 1750 to 2019. For comparison, the RF for CO_2 is 2.16 W/m² resulting in a temperature rise of 1.01 °C. Total global surface air temperature difference is observed to be 1.27 °C, thus CH_4 is responsible for more than 20 % of total temperature increase.
This significant participation of methane is due to it's high direct warming potential, which is 28 times higher than the one of carbon dioxide, seen over one century. The warming potential is the heat absorbed by a GHG in the atmosphere as a multiple of the heat which would be absorbed by the same mass of CO_2. The reason for the high warming potential of CH_4 is the stronger infrared absorbance compared to CO_2 (Myhre, 2014). Accounting also for the indirect effects contributing to the methane global warming potential, which are the result of methane oxidation processes (see Section 2.1.3), the warming potential increases further to the 34-fold compared to CO_2. Considering the short globally averaged lifetime of CH_4, which is 9.1 ± 0.9 yr (Prather et al., 2012), it's global warming potential is all the more revealing. A short lifetime in conjunction with a high warming potential means, that methane holds the potential to quickly decelerate global warming, by reducing methane emissions. The comparison with the longer lifetime of carbon dioxide, estimated to be 5-200 yrs by the Intergovernmental Panel on Climate Change (IPCC) (Archer et al., 2009), highlights this possibility once again. Vice versa rising methane emissions can raise its own lifetime. The reason for this is the depletion in tropospheric hydroxyl radicals (OH), which is caused by rising methane levels. As the hydroxyl radicals are the major sink of methane (see Section 2.1.3), the consumption of OH leads to a longer CH_4 lifetime (Stecher et al., 2021).
The recent mean CH_4 atmospheric concentration of 1906 ppb CH_4 is determined by Lan, X., K.W. Thoning, and E.J. Dlugokencky 2022 for June 2022. Historical concentrations for methane indicate, that the percentage of methane gas in the atmosphere has increased by a factor of more than 2.5 until today from roughly 695 ppb before 1800 A.D.. As the 695 ppb atmospheric CH_4 concentration was relatively stable the last millennium before 1800 A.D., there is scientific consistency that the methane enrichment of the past 200 yrs is man-made (Etheridge et al. 1998, Saunois et al. 2020). In this period since the industrial revolution began, the CH_4 mixing ratio scaled up with an average rate of approximately 5.4 ppb/yr. Since continuous methane observations, spanning the whole globe, started in 1983 by the NOAA Global Monitoring Laboratory (Turner et al., 2019) there were maximum growth rates around

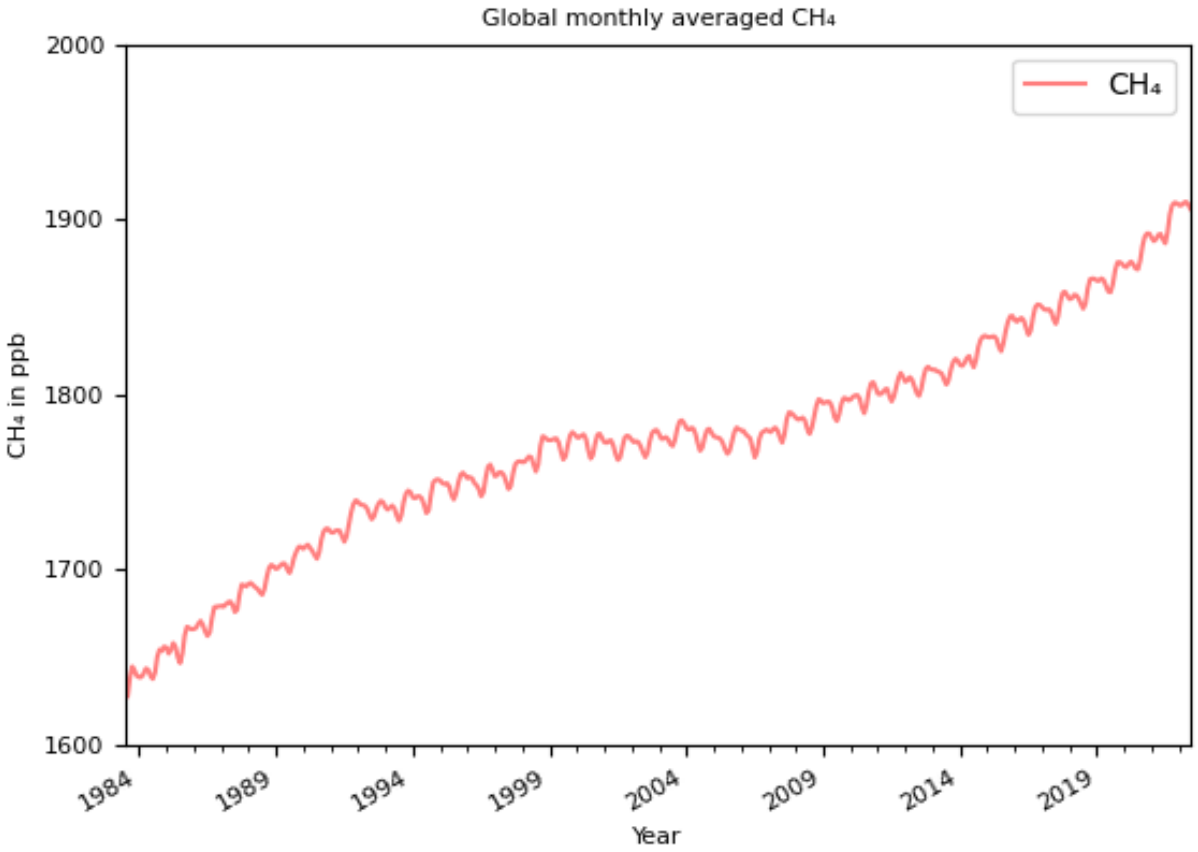

Figure 1: Methane global monthly trend from 1983 to 2021, taken from Lan, X., K.W. Thoning, and E.J. Dlugokencky 2022.

13 ppb/yr detected during the 1980s and in the period after 2007 (E. G. Nisbet et al., 2019). In Figure 1 these both phases of rising methane concentrations are recognizable. Furthermore it can be noted, that the methane concentration flattens during the 1990s and turns into a plateau with relatively constant methane levels around 1750 ppb between 2000 and 2007. The cause of this "stabilization" and in particular that of the "renewed growth" since 2007 are subject of current scientific debate (Turner et al., 2019). Chapter 2.2.3 explains different interpretations for these recent trends and to what extent the methane isotope signature offers a tool to attribute the growth periods to one source or another.

2.1.2 Methane sources

Methane is formed in different ways, these processes can be classified into three groups: *biogenic, thermogenic* and *pyrogenic*. One type of genesis is the anoxic microbial production of CH_4 by *archaea*. Most of these microbes metabolize ether acetates or CO_2 and H_2 during the last steps of biomass decomposition to methane and byproducts (Formolo, 2010). This microbial produced methane is referred to as *biogenic* CH_4. Biogenic methane emerges during enteric fermentation in digestive tracts, in organic waste deposits and under anaerob conditions in freshwater systems, wetlands, rice patties, ocean or coastal sediments. Thermal breakdown of organic matter builds the second pathway of methane formation. Long-chain polymers of organic mass are split at greater depths under high pressure and temperatures in the range of 100-200 °C (Stolper et al., 2014) with methane as a product. Methane formed this way occurs in fossil fuel and geological gas deposits. It is called *thermogenic* CH_4. The third origin of methane is the incomplete combustion of biomass, which produces not only carbon dioxide, but because of oxygen deficiency also carbon monoxide and inter alia methane. Wild and peat fires, deforestation by fire clearance and biofuel burning are the main sources of *pyrogenic* methane.

Methane generating processes are known and also the different types of sources, in which these processes take places (Saunois et al., 2020). However, it is less understood, what the extent of the emissions from the respective origins is. There are two different ways, to estimate the individual methane outputs. Top-down calculations are done on emission measurements combined with inverse modelling, whereas bottom-up approaches use process based models, accounting for land surface emissions, atmospheric chemistry, inventories and data extrapolations. 576 Tg/yr are the global annual methane emissions calculated based on top-down approaches for the decade from 2008-2017. Of these, 359 Tg/yr (i.e. 62 %) are emitted by anthropogenic sources, including waste management, agriculture and the usage of fossil and biomass fuel. According to Saunois et al. 2020, 218 Tg/yr (i.e. 38 %) were emitted by natural sources - averaged over the same decade and again based on top-down inversions. Bottom-up models calculate an overall methane emission of 737 Tg/yr, of which 366 Tg/yr (50 %) are attributed to anthropogenic sources and 371 Tg/yr (50 %) to natural. Comparing the top-down with the bottom-up estimates, disagreements are observed. Figure 2 depicts the top-down and bottom-up estimates for the different methane sources.

Wetland emissions are the dominant natural source of methane and also the largest single emitter, with 181 Tg/yr estimated by top-down calculations, whereas bottom-up models rating 149 Tg/yr. Other natural emissions leg further behind wetlands with 27 Tg/yr estimated by top-down studies, contrary bottom-up ratings are 222 Tg/yr. The CH_4 release from agriculture and waste management is 217 Tg/yr (top-down) and is summed up over the emissions from enteric fermentation and manure, landfills, waste deposits and rice cultivation. For these emissions, bottom-up estimates are 206 Tg/yr. In addition to agriculture and waste, the exploitation and usage of fossil fuels is also a anthropogenic source of methane. Top-down estimates are 111 Tg/yr, respectively 128 Tg/yr for bottom-up. Coal mining and oil and gas production are major contributors to the 111 Tg/yr, whereas industry and transport are minor emitters. Biomass and biofuel burning emissions are 30 Tg/yr for both, top-down and bottom-up estimates.

Large discrepancies are particularly noticeable for wetlands and other natural sources. Also the large uncertainties in emission determinations are more pronounced for the natural emis-

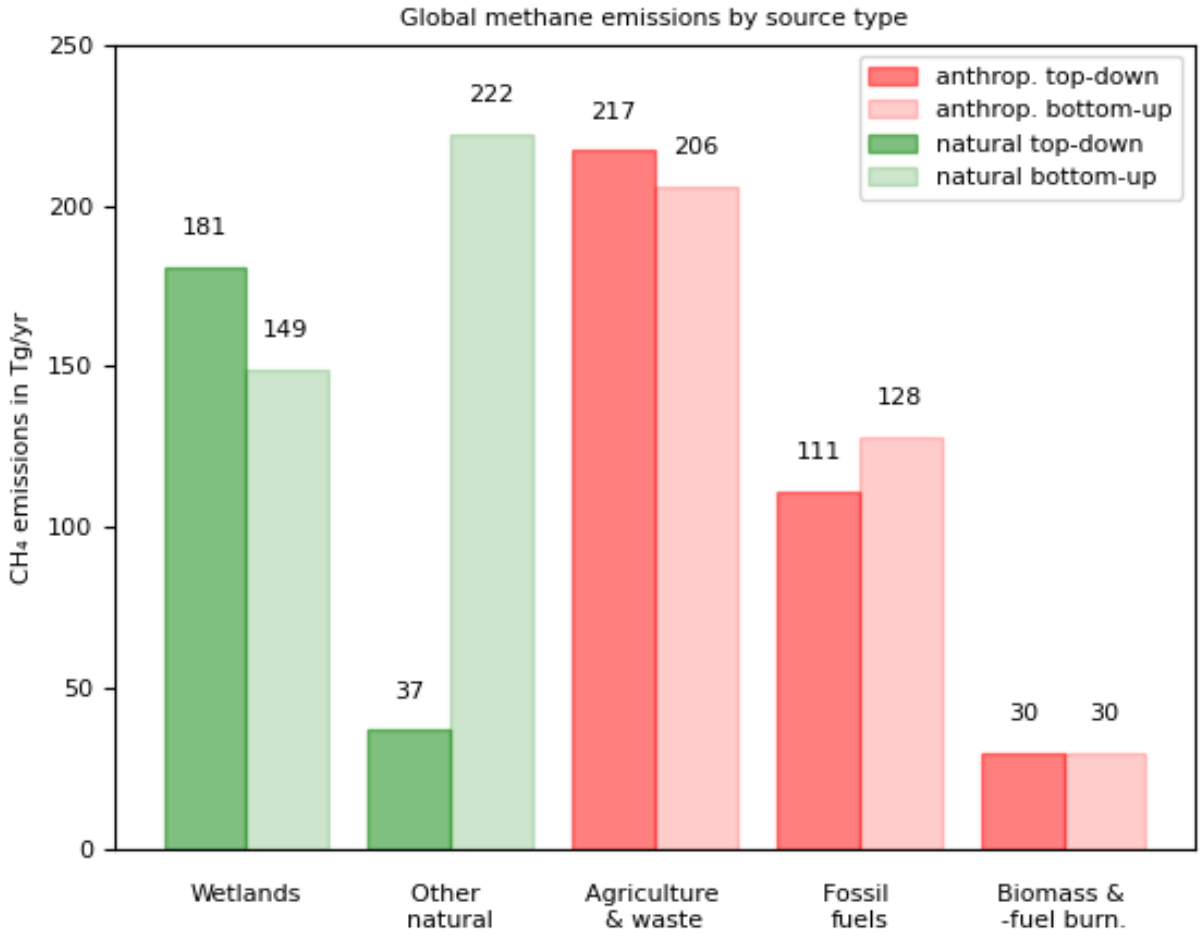

Figure 2: Top-down and bottom-up estimated methane emissions by source, following Saunois et al. 2020. The green bars represent natural sources, the red bars anthropogenic. Large differences between top-down and bottom-up sums are visible especially for the natural sources.

sions and the fossil fuel sector, as Table 1 shows. Possible reasons for that uncertainties are unconstrained wetland area extents, and therefore unconstrained CH_4 producing surface and difficulties in parameterisation of aerobic and anaerobic conditions (Saunois et al., 2020). The overestimation of the bottom-up models can be explained by double counting of freshwater area for both, wetlands and other natural freshwater systems. Wetland emissions are also difficult to estimate because climate change creates feedback mechanisms, such as rising temperatures and changes in precipitation, upon which wetland emissions are highly sensitive (Gedney et al., 2019).

	Bottom-up	Top-down
Wetlands	102-182	159-200
Other natural	143-306	21-50
Agricult. & waste	191-223	207-240
Foissl fuels	113-154	81-131
Biomass & -fuel burn.	26-40	22-36

Table 1: Range of emissions by source in Tg/yr, following Saunois et al. 2020.

2.1.3 Methane sinks

Saunois et al. 2020 stated global, annual methane removals of 556 Tg/yr for top-down estimates and 625 Tg/yr from bottom-up models. More than 90 % of the methane sink is due to the reduction of methane by hydroxyl radicals in the troposphere. Other mechanisms that lead to methane destruction are the oxidation reactions with chlorine, stratospheric photochemical reactions and uptake by methanotrophic bacteria in soils (Rigby et al., 2017). The oxidation reaction with OH is described by Ravishankara 1988:

$$OH + CH_4 \longrightarrow CH_3 + H_2O \tag{1}$$

Ambient atmospheric concentrations of the hydroxyl radical are < 1 ppt and its lifetime is < 1 s (Li et al., 2018). The initial step to the major production of OH is the ozone (O_3) photolysis by UV radiation to the excited O(^{1}D) state (Ravishankara, 1988):

$$O_3 + h\nu(< 336nm) \longrightarrow O(^1D) + O_2 \tag{2}$$

In a next step O(^{1}D) reacts with water vapor to the hydroxyl radical:

$$O(^1D) + H_2O \longrightarrow 2OH \tag{3}$$

Besides CH_4, OH is also the main oxidant for carbon monoxide (CO), nitrogen oxides (NO_x) and stratospheric ozone depleting compounds. Hence, climate and air quality strongly dependent on the OH radical (Li et al., 2018). There are various reasons why the methane concentration in particular is very dependent on oxidation with OH. As Equation (1) shows, the oxidation of methane by OH releases water vapor, which in turn is involved in OH production. Therefore this effect reduces the methane lifetime, by favouring OH production. The production of OH is also increased by tropospheric warming due to CH_4, which lead to more OH precursors, such as water vapour. Another process of tropospheric warming is the enhanced reaction rate of methane oxidation by OH, again leading to a shortening of methane lifetime (Stecher et al., 2021). An extended CH_4 lifetime is the consequence of rising atmospheric methane concentrations, because OH is depleted by the oxidation of methane (Winterstein et al., 2019). Constraining the hydroxyl radical concentration is challenging, because of the short lifetime, the high reactivity of OH and the variety of feedback mechanisms, influencing it. As OH reduction represents the bulk (518 Tg/yr) chemical CH_4 loss (together with stratospheric loss and oxidation by Cl) and calculated by top-down inversions as the mean for the years 2008-2017, OH plays a dominant role for the methane budget. The remaining deficit of 38 Tg/yr is attributable to the methane uptake in soils (Saunois et al., 2020).

2.2 Methane carbon isotope ^{13}C and $\delta^{13}C(CH_4)$

2.2.1 Introduction to ^{13}C and $\delta^{13}C(CH_4)$

The CH_4 molecule consists of one carbon atom, tetrahedrally embedded between four hydrogen atoms. Atmospheric methane consists to 98.83 % of the stable ^{12}C carbon isotope, another 1.11 % is built with ^{13}C, also a stable isotope (Gordon E.I., 2022).^{13}C containing methane is heavier than ^{12}C-CH_4, because of one additional neutron in the carbon atomic nucleus. The atomic masses are 17.034 u and 16.0428 u respectively. This mass difference causes a different physicochemical behaviour, called *isotope fractionation* (Mook, 2000). The reactivity of a molecule depends on its mobility and on the binding energies. Considering the kinetic energy of a molecule, which is given by Equation (4), taken from Mook 2000,

$$kT = \frac{1}{2}mv^2 \tag{4}$$

it is evident, that a heavier molecule can only comply with the conservation of energy by having lower velocity. This in turn means, that its diffusion velocity is lower and its collision frequency is reduced, both making a chemical reaction less likely to occur in a certain time period. Additionally, most of the heavier atoms have higher binding energies, equivalent to more activation energy required to break bonds. This is due to the lower vibrational energy states, which form in the heavier molecules, thus a larger potential well has to be surpassed for bond breaking (Mook, 2000). Because of this different behaviour of the two methane isotopes, they are favored to different extents to enter into chemical reactions or to be metabolised. Divergent isotope ratios result for the various methane-producing and -dissolving processes, therefore providing a quantity for distinguish between these processes. The ^{13}C to ^{12}C isotope ratio is commonly represented by the δ -notation (Werner and Brand, 2001):

$$\delta^{13}C(CH_4) = \left(\frac{(\frac{^{13}CH_4}{^{12}CH_4})_{meas}}{(\frac{^{13}CH_4}{^{12}CH_4})_{ref}} - 1 \right) \times 1000 \tag{5}$$

Here the isotopic ratio is given as the deviation in parts per thousand (‰) from a reference standard. The standard typically used is called the Vienna Pee Dee Belemnite (VPDB), which is very rich in ^{13}C (Werner and Brand, 2001):

$$\left(\frac{^{13}CH_4}{^{12}CH_4} \right)_{VPDB} = 0.0111802 \tag{6}$$

2.2.2 The isotopic ratio of methane sources

Isotope specific physicochemical behaviour leads to fractionation processes when methane is part of a chemical reaction or gets metabolized. The different isotopic ratios for the various methane sources, listed in Chapter 2, are subject of this subsection. Figure 3 shows the normalised probability density distributions of the various emitters (see Sherwood et al. 2017). They are built upon numerous of thousands of measurements of δ^{13}C(CH_4) distributed around the globe.

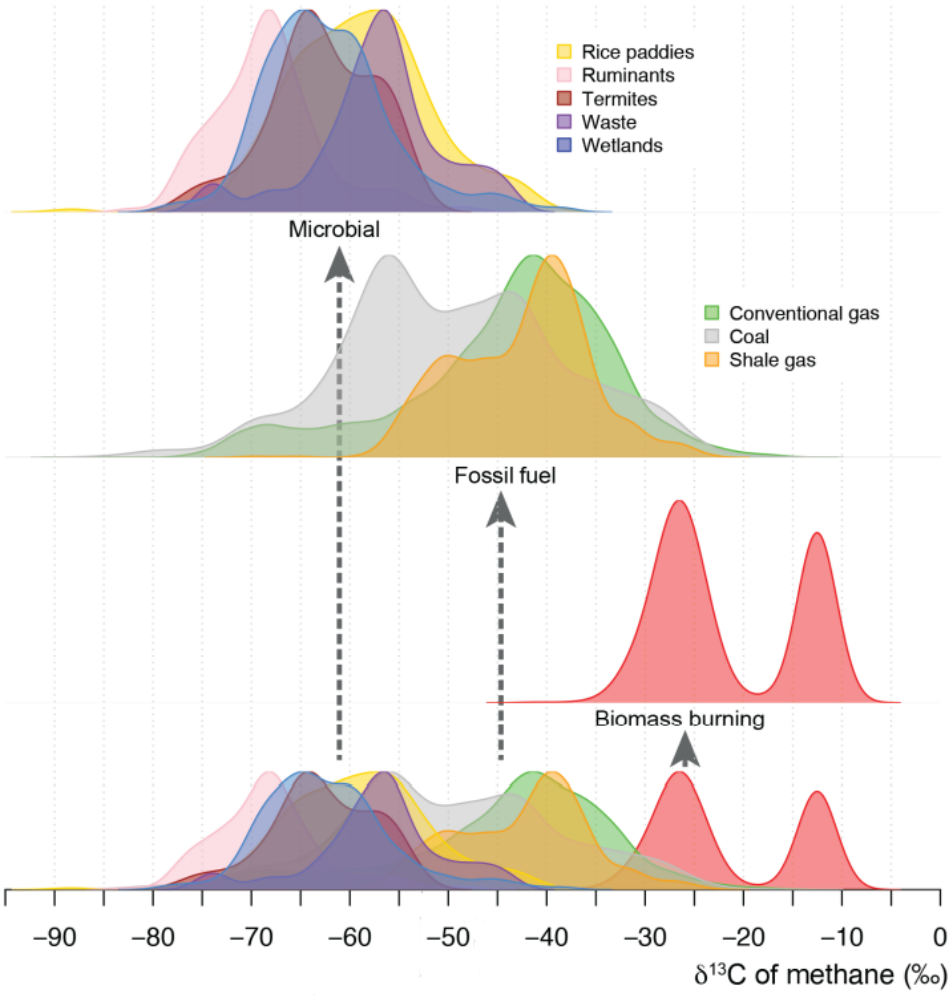

Figure 3: δ^{13}C(CH_4) signatures for the different methane sources, taken from Sherwood et al. 2017. Each type of methane production shows its individual isotopic composition. Microbial methane is more depleted in ^{13}C, methane from biomass burning is relatively rich in ^{13}C, and fossil fuel related methane ranges in between. The strong scattering of the signatures of the individual formation processes and their overlap are remarkable.

The three main pathways of methane formation, introduced in Chapter 2.2.2, are identified by their ratio of ^{13}C. Biogenic methane that comes from microbial production in wetlands, waste, rice paddies and the metabolism of organic matter by ruminants and termites is poor in the

heavier methane isotope. Pyrogenic CH_4 forms two peaks in the signature, resulting from the combustion of either C3 or C4 plants. The former ones have a lighter isotopic composition, the latter are more enriched in heavier methane. Fossil fuel related methane has signatures located between pyrogenic and biogenic methane and covers a wider spectrum of signatures. The reason for that is the biodegradation of petroleum, gas and coal by microbes (Milkov, 2011). Thereby secondary methane is formed, which is of microbial origin and consequently shifting the isotopic ratio. The individual range of single source signatures is determined by boundary conditions such as temperature, pressure, type of converted biomass, degree of anaerobicity et cetera. Due to similar methanogenesis pathways, the signatures of the individual sources can overlap significantly. For a better overview of where the individual source signatures are located, Table 2 presents the mean values of the measurements, following Sherwood et al. 2017.

CH_4 source	Mean($\delta^{13}C(CH_4)$) in ‰
Wetlands	-61.5
Waste	-56.0
Termites	-63.4
Ruminants	-65.4
Rice paddies	-62.2
Conventional oil & gas	-44.0
Coal	-49.5
Shale gas	-42.5
C3 biomass burning	-26.7
C4 biomass burning	-12.5

Table 2: Mean values of methane source signatures, following Sherwood et al. 2017.

Because of the widths of single source signature distributions and the overlaps with other source types, it is essential to provide spatially and temporally high resolved measurements of $\delta^{13}C(CH_4)$. Only then can the isotope ratio be used as a key instrument for the source allocation of methane and thus unleash the full potential as a tool for a better understanding of global methane budgets. (Sherwood et al. 2017, Ganesan et al. 2018, Saunois et al. 2020).

2.2.3 $\delta^{13}C(CH_4)$ atmospheric trend

In Chapter 2.2.1 it was explicated, that because of individual *isotope fractionation*, there are pathways which lead to more ^{13}C enriched or depleted methane. These different emissions are mixed in the atmosphere and can be averaged globally and temporally. The mean isotopic signature of the global methane producing fluxes is estimated by Schwietzke et al. 2016 to be -53.5 ‰in 2016. In contrast, the global mean atmospheric $\delta^{13}C(CH_4)$ is determined to be -47.3 ‰for the same year (Lan et al., 2021). The difference is caused by the methane sink mechanisms, which favour reactions with the lighter molecule, therefore creating a surplus of the heavier methane isotope remaining in the atmosphere (Quay et al., 1999). The majority of atmospheric methane is emitted in the northern hemisphere, therefore a north-south gradient forms, with more ^{12}C enriched methane in the north, and more ^{13}C enriched methane in the southern hemisphere. Since methane is released from ground sources, and is oxidized with time, while getting lifted and transported into the upper troposphere and beyond into the stratosphere, there is also a gradient in $\delta^{13}C(CH_4)$ by altitude. The heavier isotopes are less present relative to the lighter ones near the ground, while they are more common in the stratosphere (Quay et al., 1999). Ice core measurements provide data for pre-industrial $\delta^{13}C(CH_4)$ values, which are -49.6 ‰ 300 yrs ago. Since then, the isotopic ratio of methane has remained almost constant until approximately 100 yrs ago, going along with a doubling in atmospheric methane concentration. The lower ^{13}C contribution to methane 300 yrs ago suggests more biogenic sources compared to the recent times. The doubling in atmospheric methane concentration between approximately 1700 A.D. and 1900 A.D. can be explained by emissions from identical sources as before, but increased in methane output, by, e.g. expanded livestock and biomass burning (Craig et al., 1988). Growth rates started to increase rapidly during the last century, with shifting $\delta^{13}C(CH_4)$ towards heavier isotopic composition. Different possible explanations exist and there is no clear consensus in determining the sources that led to this increase, except it is caused by human activities. Enhanced biomass burning is suspected to have played a major role (Ghosh et al., 2015). Towards the end of the twentieth century, the methane growth slowed down and the globally averaged isotopic ratio stabilised at -47.1 ‰, which could be attributed to less burning of biomass and less fugitive emissions of oil and gas industry (Worden et al. 2017,Dlugokencky 2003). This stabilisation lasted until 2007. Since then, a complementary trend than in the previous century is observable: indirect proportionality describes the course of the renewed increase in methane to the isotope ratio, which decreases towards more ^{13}C depleted CH_4 (see Figure 4).
Both, methane rise and isotopic depletion since 2007 are not yet fully understood and sundry emission scenarios are discussed (E. G. Nisbet et al., 2019). Changed sources of fossil energy carriers, lighter in the isotope ratio, e.g. shale gas, but also a decreased OH concentration alone offer insufficient explanations (Nickl 2022, Nisbet et al. 2016). Because of the decreasing $\delta^{13}C(CH_4)$ value since 2007, there is indication, that biogenic sources are major contributors to the renewed methane rise. Nisbet et al. 2016 and Schaefer et al. 2016 attribute the increase mostly to agricultural and wetland sources, depleted in ^{13}C, and therefore consistent with growth in the CH_4 concentration and loss in isotopic weight. Zhang et al. 2022, on the other hand, argued, based on bottom-up models fed with CH_4 source signature data, that agriculture, landfills and waste contribute to 53 % to the post 2007 growth, fossil fuel emissions 34 % and wetland emissions only 13 %. In contrast, recent research results (Basu et al., 2022), built on the inverse modelling framework TM5-4DVAR and including $\delta^{13}C(CH_4)$ data, attest

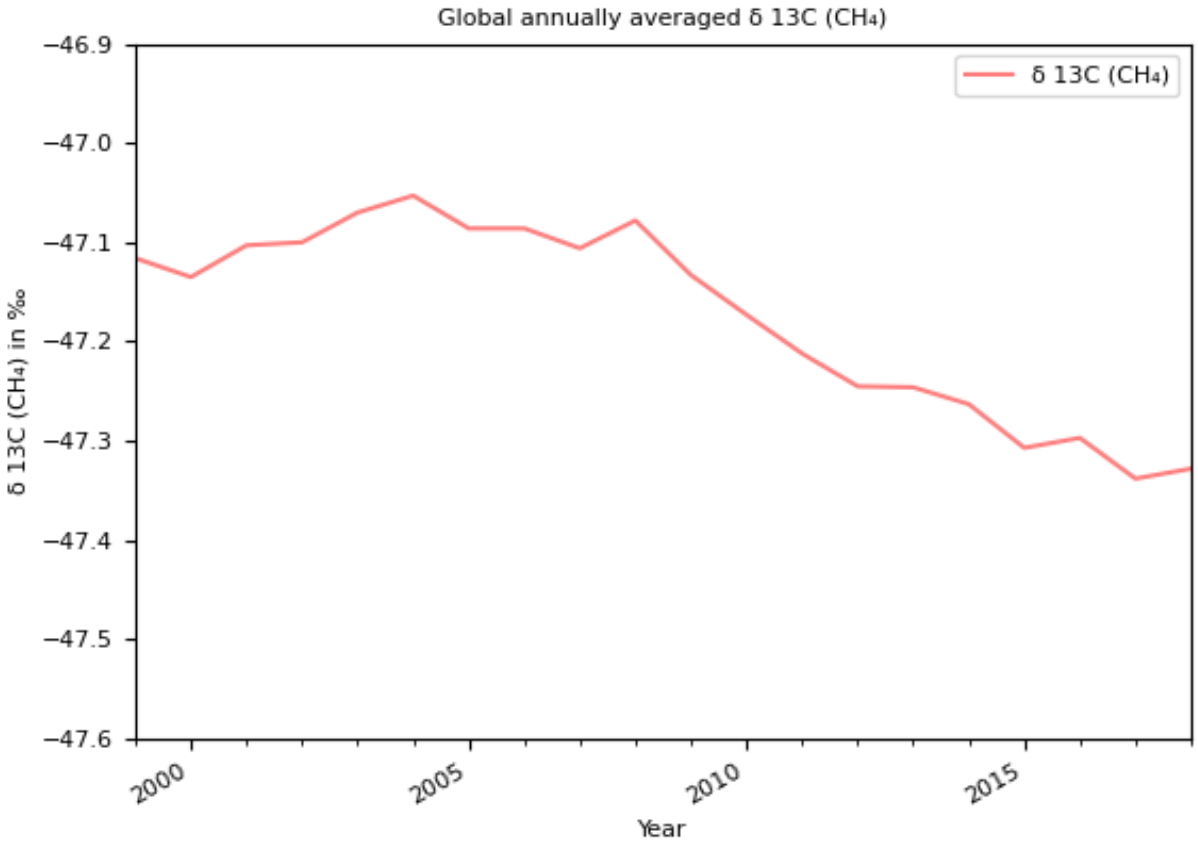

Figure 4: Globally and annually averaged atmospheric δ^{13}C(CH$_4$), data taken from Lan et al. (2021). The stabilization in methane before 2007 can also be observed in the isotope ratio, which is relatively stable at -47.1 ‰ before 2007. Since then, the trend is towards methane more depleted in ^{13}C.

85 % of the increase to microbial sources and only 15 % to fossil fuel related emissions. The various possible explanations and allocation of emissions to different sources underlines the need for spatially and temporally close measurement of methane isotopes for source attribution (Sherwood et al. 2017,Saunois et al. 2020) and especially those of areal biogenic sources, such as husbandry and wetlands, as these play an important role in the current methane trend and at the same time show great uncertainties in relation to their emissions (Ganesan et al. 2018, see Chapter 2).

2.2.4 Determination of the $\delta^{13}C(CH_4)$ signature

The isotopic signature of a methane source is rarely present in pure form, but is usually mixed into a methane background fed from various sources. The challenge is to determine the unadulterated isotope ratio from the methane source of interest. This can be done with the method of the Keeling plot, which is subject of this section. Atmospheric GHG concentrations (c_a) are made up of the background concentration (c_b) and the enhancement from the source (c_s). They are related to each other as Equation (7), adapted from Pataki et al. 2003, shows:

$$c_a = c_b + c_s \tag{7}$$

Accounting for the conservation of mass, the equation is still valid, when multiplying each contribution with the corresponding $\delta^{13}C(CH_4)$ values.

$$\delta_a c_a = \delta_b c_b + \delta_s c_s \tag{8}$$

Here δ_a, δ_b and δ_s are the isotopic signatures of the atmosphere, the background without additional methane from the source of interest, and the signature of the enhancement by the source respectively. Combining Equations (7) and (8) together, the concentration increase due to the source of interest, c_s, has not longer to be known, and the isotope ratio of the latter can be determined by the remaining components:

$$\delta_a = \frac{c_b}{c_a}(\delta_b - \delta_s) + \delta_s \tag{9}$$

The isotopic signature and concentration of the background can be detected by, e.g. a measurement upwind of the source of interest. δ_a and c_a are the measured quantities when taking samples downwind of the source, i.e. detecting the superposition of background and source. Equation (9) converges towards the second term of the right side, i.e. δ_s, for high total methane concentration c_a. As the methane background is relatively constant, this means, that high total methane concentrations are caused by increased emission from the source of interest, c_s. For the sampling strategy (see Chapter 5.1), this is an important condition, since the ideal case of measurement, where $\delta_a = \delta_s$ is valid, can be approached for strong concentration enhancements of the source.
The above mentioned method to determine δ_s, is accounting for only one single measurement. For a solid data situation it is meaningful to include several measurements from the same source. A Keeling plot provides the graphical solution of Equation (9), whilst recording δ_a of a measured sample versus the reciprocal absolute concentration c_a. If at least two samples are taken from the same source, one can extrapolate the source signature δ_s via a linear regression towards the intercept where $\frac{1}{c_a} = 0$, thus representing the pure source isotopic signature. An exemplary Keeling plot is shown in Figure 5.
The intercept of the linear regression model corresponds to the methane source signature, therefore the error range of the intercept is equivalent to the uncertainty of the determined signature. An erroneous regression results from imperfect correlation of the individual data points, i.e. the data points do not lie directly on the fitted straight line, but instead have non zero residuals. Following Skoog and Leary 1996, the error of the intercept, σ_i, is calculated as follows:

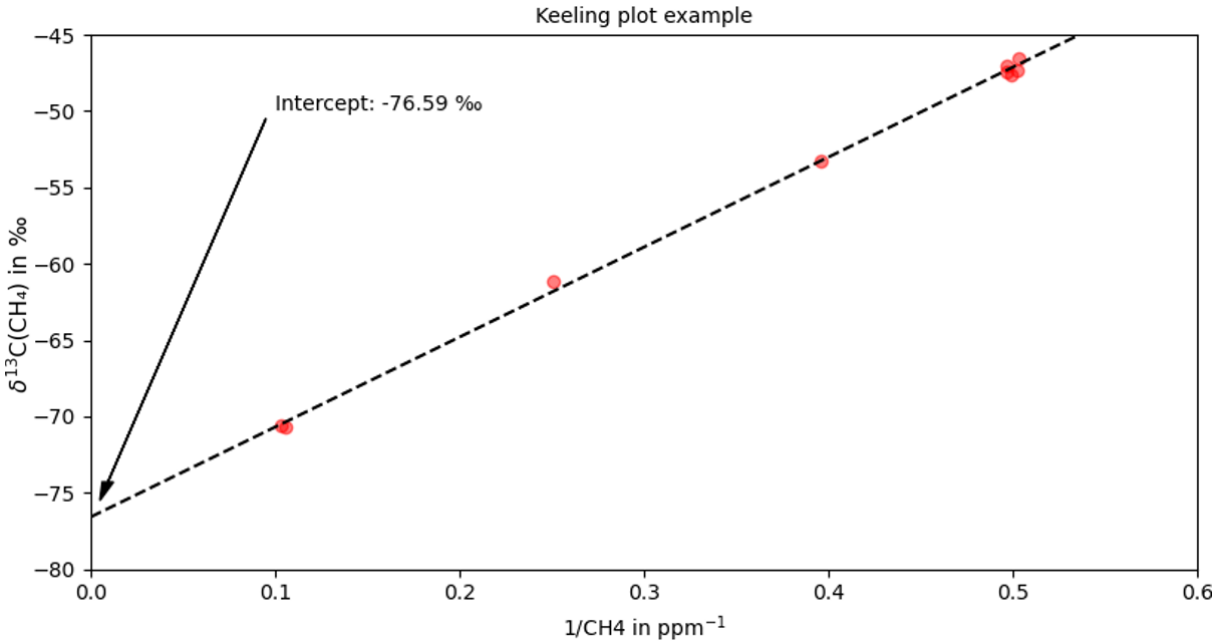

Figure 5: Exemplary Keeling plot for methane: Via a linear extrapolation the pure source signature can be determined by calculating the intercept. The red dots represent single measurements of one source, with different enhancements compared to the background. The resulting signature in this case is -76.59 ‰.

$$\sigma_i = \sqrt{\frac{\Sigma(y_i - y_{i,fit})^2 \Sigma(x_i)^2}{(N-2)(N\Sigma(x_i)^2 - (\Sigma x_i)^2)}} \tag{10}$$

In Equation (10), y_i and $y_{i,fit}$ are the measured isotope ratios, δ_a and the isotope ratios of the corresponding point on the linear fit function respectively. N is the number of data points and x_i the measured reciprocal methane concentrations. The equation shows, that larger residuals $(y_i - y_{i,fit})$ result in larger errors of the calculated intercept, i.e. larger uncertainty of the source signature δ_s.

2.3 The Planetary boundary layer

The planetary boundary layer (PBL), is the lowermost part of the troposphere and stays in contact with the surface. It develops during daytime, as the solar radiation causes surface heating and therefore thermal uplift of surface near warmer air and subsidence of colder air above. This mixed, turbulent layer (ML) increases further until the afternoon, and stops growing after sunset. By radiative cooling of the ground during the night, the mixing process stops, the ML becomes the convectively inactive residual layer (RL) and a stable stratified boundary layer (SBL) builds up from the surface. This process begins anew at sunrise, with the PBL being separated from the free troposphere by the entrainment zone (EZ). The latter allows exchange of air dependent on the strength of inversion. Temperature is decreasing with altitude in the ML, but increasing in the EZ, what causes static stability at the PBL top. (Wallace and Hobbs, 2008). A schematic diagram of the PBL is shown in Figure 6, taken from Stull 2015.

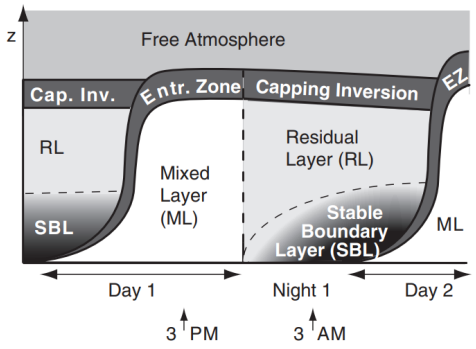

Figure 6: The evolution of the PBL is sketched. The representation is explained in the text.

The top of the PBL is determined by increased humidity, which is released from the surface into the atmosphere by evaporation. The temperature inversion in the EZ restricts the exchange between the PBL and the free troposphere, thus water vapour, GHGs and particles are trapped beyond the EZ. Relatively constant humidity and GHG concentration profiles within the ML are the consequence. Above the PBL top, the humidity decreases towards the dry level of the free troposphere. Figure 7 shows the temperature and humidity profiles throughout the PBL.

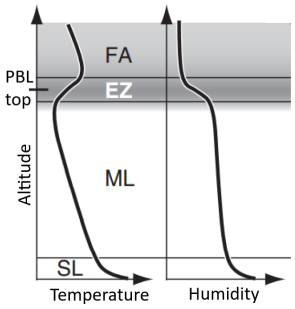

Figure 7: Temperature and humidity profiles for the PBL are sketched. Adapted from Stull 2015.

3 The CoMet 2.0 Arctic campaign

CoMet (**c**arb**o**n dioxide and **met**hane mission) 2.0 Arctic is a research program, led by the German Aerospace Center (DLR) with the aim to investigate the distribution and temporal variation of carbon dioxide and methane in the arctic in cooperation with the Max Planck Institute Jena (MPI), the Institute of Environmental Physics of the University of Bremen and the Meteorological Institute of the University of Munich. In the course of the campaign, the HALO aircraft (high altitude and long range research aircraft) serves as platform for different instruments to measure these two greenhouse gases, as well tracers of them. HALO can be seen in Figure 8.

Figure 8: The DLR research aircraft HALO at the landing approach over Edmonton. The protruding stalks on the roof are the trace gas inlets (TGI), the foremost of which is the one used to supply the MIRACLE instrument.

Both, in situ and remote sensing instruments are on board the aircraft to provide a variety of different measurement techniques, which can be compared with each other and furthermore are able to draw a comprehensive picture of the two most important greenhouse gases in the canadian arctic. Furthermore, the campaign involved collaboration with several international research teams, including the NASA with the Above research program (arctic boreal vulnerability experiment), the TCCON network (total carbon column observing network) and the greenhouse gases observing satellite (GOSAT).
The payload of HALO includes the airborne demonstrator for the Methane Remote Sensing Lidar mission (MERLIN), a french-german collaboration, called CHARM-F. This active remote sensing instrument uses the technique of integrated path differential absorption, thus is independent on solar radiation and offers high accuracy data. With MAMAP2DL a passive remote sensor for the two dimensional imaging of CH_4 and CO_2 sources was also part of the instrumentation. The specMACS hyperspectral imager can investigate cloud properties and delivers data on ground albedo and spatial extend of methane point sources. At in situ instruments, a Picarro greenhouse gas analyzer of the MPI is on board, which can detect methane and carbon dioxide as well as carbon monoxide. The Jena air sampler (JAS) collects spot samples for laboratory analysis of CH_4, CO_2, CO, N_2O, H_2, SF_6 and the isotopologues of the first

two. MIRACLE contributes with the in situ measurement of CH_4, CO_2, C_2H_6 and $\delta^{13}C(CH_4)$. Basic meteorological data like pressure, temperature, the wind vector and aircraft parameters are recorded by the BAHAMAS instrument (basic HALO measurement and sensor system). Dropsondes can give information on temperature, pressure and relative humidity profiles.
The scientific targets included both, natural and anthropogenic greenhouse gas sources and especially the extended boreal and arctic wetland areas and permafrost regions of high northern latitudes, which are major methane emitters, but less constrained than other sources, as discussed in Section 2.1.2. The campaign was based in Edmonton, Alberta, and took place in August and September 2022. With the high range of 10000 km of HALO, major parts of Canada could be covered. Sampled areas included the Hudson Bay Lowlands and Lake Winnipeg wetlands in the east, coal mines and oil and gas production facilities in and near the Rockie Mountains in the west, and boreal and arctic wetlands in the Peace Athabasca river delta respectively in the McKenzie river delta in the north. A total of 140 flying hours were held, including a test flight, as well as the arrival and return flights. A map with the the flight patterns from all research flights is shown in Figure 9.

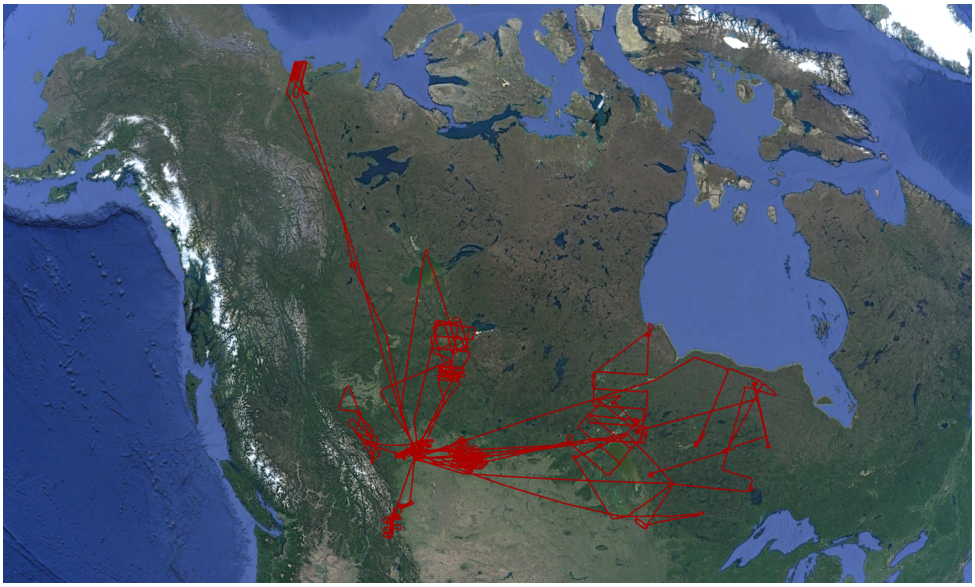

Figure 9: All flight tracks of the CoMet 2.0 arctic campaign are shown on a map of Canada.

Chapter 5 describes in more detail some of these target areas, for which the isotopic signature of the methane source, determined by the MIRACLE instrument, are discussed in Sections 5.2 and 5.3. The next chapter discusses the functioning of the MIRACLE instrument and its characterization.

4 Concept and Characterisation of the MIRACLE Instrument

A new and innovative airborne measurement setup was constructed to achieve precise $\delta^{13}C(CH_4)$ data aboard the DLR research aircraft HALO. The first part of this chapter deals with the function and performance of the Picarro G2210-i GHG analyzer. To achieve high measurement precision, a sampler unit was constructed around the analyzer, which is subject of the second part of this section.

4.1 The greenhouse gas analyzer Picarro G2210-i

The measurements were done with a Picarro G2210-i greenhouse gas analyzer, which measures methane, ethane, carbon dioxide, water vapor and $\delta^{13}C(CH_4)$ by the principle of cavity ring down spectroscopy (CRDS). Since the aim of this work is to validate the measurement setup described here for the measurement of the methane carbon isotope ratio, only the relevant parameters, i. e. methane and $\delta^{13}C(CH_4)$ are discussed in the context of the characterization of the instrument and in Chapter 5 for the evaluation of two example flights.

4.1.1 The principle of cavity ring down spectroscopy

Conventional spectroscopy is based on the measurement of the magnitude of absorption. The amount of transmitted light can be measured as a function of the frequency, and an absorption spectrum can be thus be deduced (Berden et al., 2000). Via the Lambert-Beers Law,

$$I_t = I_0 e^{-\sigma L N} \tag{11}$$

one can derive the particle density N in [cm^{-3}] of the absorbing species. I_t describes the transmitted intensity of the light beam, I_0 the initial intensity, L in [cm] the absorption path length and σ in [cm^2] the absorption cross section of the absorbing species (Demtröder, 2010). A major problem of the conventional spectroscopy is the limited sensitivity. If the radiation attenuation is weak, because of low particle concentration, then a small difference between I_t and I_0 has to be resolved. This can be remedied by increasing the path length L, by application of modulation schemes or by using secondary absorption events such as fluorescence, photoacoustic effects or resonant enhanced multi photon ionization. The latter techniques on the other hand require complex calibrations (Berden et al., 2000). CRDS circumvents the limited sensitivity by measuring the ring down time of the light beam in the cavity, thus is based on the measurement of the rate of absorption. The laser couples pulses into the cavity, on the opposite sides of which are highly reflective mirrors placed in such a way, that constructive interference takes place. After each pulse, the intensity of the light beam rings down in a certain time interval, because a small proportion transmits through the mirrors and escape from the cavity. Figure 10 depicts the ring down of the signal schematically.
Considering absorption by gas inside the cavity, the ring down time τ_r, after which the input intensity has dropped to the $\frac{1}{e}$ part, will be less then the one without absorbing species in the cell (τ_0). τ_r can be derived by considering Equation (11) and adding intensity loss due to transmission through the mirrors (T) and absorption by the mirrors (A), yielding the intensity after one round trip, i.e. after two reflections (I_r)

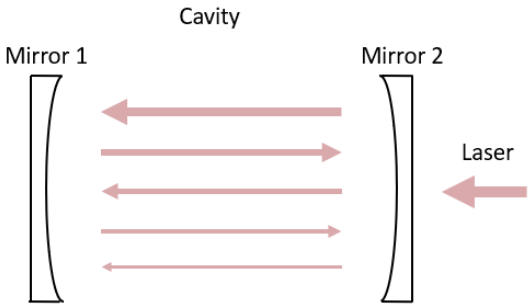

Figure 10: Sketch of the ring down in the optical cavity. By repeated reflections between the two mirrors, the intensity of the induced laser beam decreases, indicated by the thinner arrows.

$$I_r = I_0 e^{-2(\sigma LN + T + A)}. \tag{12}$$

While the light passes the cavity back and forth, with the speed of light c, the round trip time, t_r, elapses:

$$t_r = \frac{2L}{c} \tag{13}$$

In Equation (13), it is assumed that the length of the cavity and the absorption path length are the same. Finally the time dependent intensity attenuation is given by:

$$I_r(t) = I_0 e^{-2(\sigma LN + T + A)} e^{-\frac{t}{t_r}}. \tag{14}$$

The conditions $I_r(\tau_r) = I_0 \frac{1}{e}$ and $T + A = 1 - R$, with reflectivity of the mirrors R, results in the following:

$$\tau_r = \frac{L}{c(1 - R + \sigma LN)} \tag{15}$$

Eventually the difference in reciprocal ring down times leads to:

$$\frac{1}{\tau_r} - \frac{1}{\tau_0} = c\sigma N \tag{16}$$

Thus, measuring both ring down times, with and without the absorbing gas in the cavity, gives the particle number density N. The concentration X in [mol mol^{-1}] of the species can than be derived via

$$X = \frac{N}{N_{air}}, \tag{17}$$

with N_{air} being the number density of air. Since the concentration measurement depends only on the ring down times, which can be recorded by a photodetector, the CRDS technique is not affected by the light amplitude inside the cavity. Due to the very long effective path length, L, even small concentrations in the ppb and ppt regime can be detected (Berden et al., 2000).

4.1.2 Picarro G2210-i

The Picarro G2210-i measures the isotopic ratio of ^{13}C to ^{12}C in methane, thus providing a tool for methane source determination. Besides the $\delta^{13}C(CH_4)$ value and the concentration of CH_4, the concentrations of ethane (C_2H_6), CO_2 and water vapor (H_2O) are detected by the technique of CRDS (see Section 4.1.1). The cavity of the Picarro is kept at a constant pressure of 197.3 hPa and cavity temperature of 45 °C. Stable pressure and temperature conditions are a prerequisite for well defined absorption lines, as line broadening increases with enhanced pressure and temperature (Demtröder, 2010). Picarro indicates a stability of $\pm$ 0.2 hPa for the pressure and $\pm$ 0.005 °C for the temperature. Within the analyzer, three continuous wave lasers are implemented, emitting in the wavenumber spectra of 6027-6031 cm^{-1}, 6055-6059 cm^{-1} and 6249-6254 cm^{-1} (personal communication with Picarro Inc., March 2022). $^{13}CH_4$ is detected via the absorption around 6029,1 cm^{-1}, i.e. at a wavelength of 1658.6 nm. $^{12}CH_4$ on the other hand is measured by four strong absorption lines around 6057.07 cm^{-1}, corresponding to a wavelength of 1650.9 nm. The concentration of water results from the 6027-6031 cm^{-1} regime, the one of carbon dioxide from 6055-6059 cm^{-1} scanning, and ethane from the 6249-6254 cm^{-1} range. A precise wavelength monitoring unit ensures sub-picometer wavelength control within microseconds (Rella et al. (2015)). Three mirrors with reflectivities of more than 99.999 % (Picarro Inc. (2022)) enable an effective path length of up to 30 kilometers and the cavity volume is 35 cm^3 (Picarro Inc., 2020), thus a fast sample turnover time can be realized and an isotope ratio measurement frequency of 0p8 Hz is possible.
The intensity of the radiation increases during the built up phase, when the laser light is coupled into the cavity. After a certain threshold intensity is reached, the laser beam is decoupled from the optical resonator (cavity), from this point on the intensity begins to drop down and the ring down time τ_r can be measured. Approximately 200 ring down events take place per second and by tuning the laser in 10-20 wavenumber intervals of 0.02 cm^{-1} around the location of the peak, the whole absorption width is scanned (Rella et al., 2015). τ_0 is determined with ring down measurements at wavelengths, where the sample gas does not absorb the light (Klausner, 2020).
Figure 11 shows the main components of the instrument. The upper part of the picture displays the back view, including the inlet port (1) and the outlet port (2), on the latter, the gas to be sampled is drawn through the analyser with a vacuum pump. The flow is managed by the two valves. Furthermore the power connection (3) and the computer ports (4) can bee seen. In the lower part the interior setup can be observed. Number (5) depicts the laser diode for the measurement of C_2H_6, number (6) the one for $^{12}CH_4$ and number (7) the one for $^{13}CH_4$. (8) is the wavelength monitoring unit and (9) shows the optical cavity.

Figure 11: Back view (top) and inside view (bottom) of the Picarro G2210-i greenhouse gas analyser. The numbers indicating the individual components.

4.2 Instrument characterization of the Picarro G2210-i

4.2.1 Calibration procedure

To provide correct absolute measurements of GHG concentrations, a frequent calibration of the analyzer against well defined, accepted standards is essential. The National Oceanic and Atmospheric Administration (NOAA) produces such gas standards, consistent with the regulations about quality observance set by the Global Atmosphere Watch (GAW) program (Klausner, 2020). These, so called primary standards were used for the calibration of the Picarro G2210-i. As the primary standards are expensive, secondary standards, manufactured by Air Liquide (AL) provided the regular calibration standards during the campaign. Because the GHG concentrations of the AL standards are less well defined ($\pm 2\,\%$ for CH_4, vs. $\pm 0.2\,\%$ for NOAA standards), the gases were cross calibrated before the campaign. Two bottles with different GHG concentration were measured with the Picarro for a period of ten minutes, of which the last five minutes were taken into account for the analysis. The NOAA certified

concentration were assumed to be true, therefore a linear regression was obtained from the two-point NOAA calibration, as shown in Figure 12 for methane. C_2H_6 and CO_2 have been calibrated in the same way.

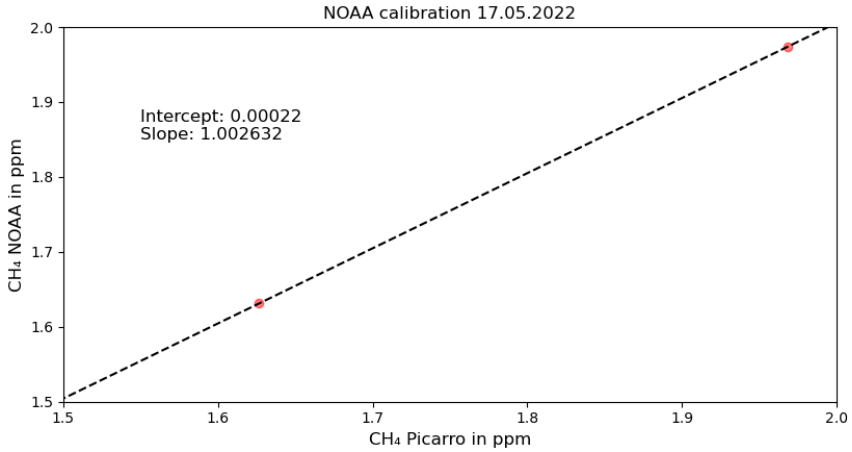

Figure 12: Calibration of the analyser with the NOAA standards, before the campaign (17.05.2022). The NOAA stated concentrations of CH_4 are plotted versus the measured concentrations, indicated by the red dots for the two flasks. Intercept and Slope are determined via linear regression.

Slope (m) and intercept (c) are received from the linear regression model. Subsequently, the secondary standards, used for calibration during the campaign were measured against the NOAA calibrated Picarro. The AL concentrations detected by the analyzer (X_{meas}) can be corrected related to the NOAA flasks (X_{corr}) in the following manner:

$$X_{corr} = X_{meas}m + c \tag{18}$$

NOAA corrected values of the three Air Liquide bottles, which were used as calibration standards during the CoMet 2.0 campaign, are presented in Table 3. The values are from the measurement before the campaign started (17.05.2022).

NOAA flask number	CH_4 in ppm
CB11361	1.9739
CB11542	1.6310
AL flask number	**$CH_{4,corr}$ in ppm**
D3FGM08	1.9650
D5RDK1N	1.5844
D4NTUE2	2.4236

Table 3: CH_4 concentrations of the NOAA standards, and NOAA corrected Air Liquide flask concentrations, used for the campaign. The measurements were done on 17.05.2022, ahead of the campaign.

During the measurement campaign, the Picarro was calibrated once a week against the Air Liquide bottles. Thus a campaign averaged linear regression could be calculated. This was

done by taking every weekly calibration data into account for the model, and plotting these data versus the NOAA corrected concentrations, determined before the mission. If one assumes that the amounts of gases in the AL bottles remain constant over time, the calibration procedure as mentioned above would be complete. To carry out the calibration even more accurately, a second calibration against the NOAA bottles after the campaign would also be useful, to detect any possible drift of the secondary standards. Thereby the time dependent concentrations of the AL gases could be determined via a linear relation between the cross calibration before and after the measurement phase. Within the timescale of this work, it was not possible to carry out a second cross calibration of the AL standards against the primary NOAA standards, because the transport of the AL bottles back home by ship was delayed. Hence the concentrations presented in this work are calibrated with the assumption of stable secondary AL standards, which were only aligned to the more accurate NOAA standards once before the campaign. Figure 13 shows the linear regression plot for the calibration data of the mission phase.

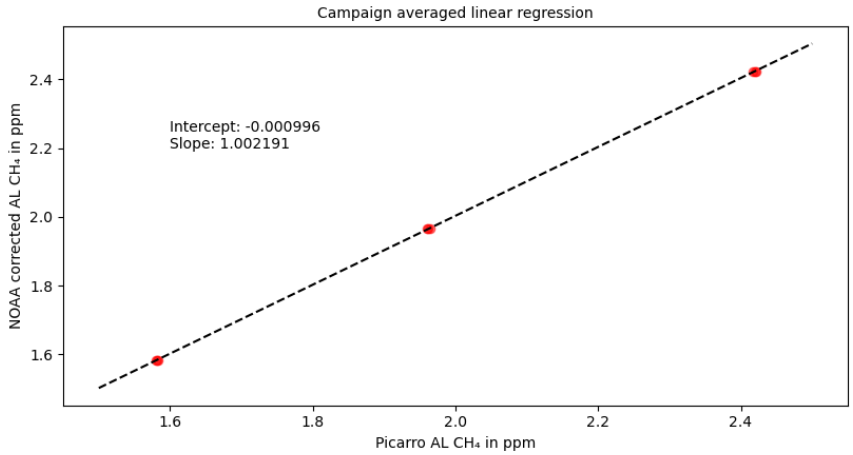

Figure 13: Methane calibration of the Picarro with the AL bottles during the campaign. The measured concentrations versus the NOAA corrected values are plotted. From the calibration procedures during the mission, an averaged linear regression model is deduced. The intercept c_{avg} and the slope m_{avg} of the model are noted down in the graph. CH_4 data of all research flights are corrected via Equation 19.

With the campaign averaged intercept, c_{avg}, and slope, m_{avg}, the obtained data are corrected with the coefficients of the linear regression by adjusting the ambient concentration measured by the analyser (X_{meas}) via Equation (19).

$$X_{corr} = X_{meas} m_{avg} + c_{avg} \tag{19}$$

This correction was done for all methane data presented in this work. At the time of submission of this work, the DLR IPA trace gas laboratory did not have any reference gases for $\delta^{13}C(CH_4)$, neither primary nor secondary. Thus, a calibration of the isotopic ratio was not possible. NOAA cylinders, which are currently being analyzed for their isotope ratio by means of a mass spectrometer at the Max Planck Institute Jena, may be used to cross calibrate the same AL cylinders used for the methane calibration, so that the $\delta^{13}C(CH_4)$ measurements can be calibrated subsequently.

4.2.2 Drift, response time, noise and overall measurement uncertainty for CH_4 and $\delta^{13}C(CH_4)$

Drift

To investigate the long-term behavior of the analyzer, the drift is measured. For this purpose, a 28 h measurement was carried out, during which the Picarro was supplied with zero air, a gas, which consists only of oxygen and nitrogen. Since the concentrations of the gas bottle are nearly constant over time scales of hours and days, the concentrations measured by Picarro should ideally also be constant. If the concentration measurement changes, drift is present. To calculate the drift of the analyzer, the mean methane concentration was determined for every five minute interval within the whole measurement time. At the end of the measurement time, the concentration was increased by 0.51 ppb in methane compared to the concentration at the beginning of the process. Since the measurement time was 28 hours, the drift in methane is determined to be 0.018 ppb/h.

Response time

The response time of the Picarro is the time that elapses between sending a new signal and capturing it by the instrument. To determine this value, a three-way valve is placed directly in front of the analyzer's inlet valve. At the beginning of the experiment, the analyzer is fed with ambient air via the three-way valve. At a certain time, the valve switches from one port to the other one, where zero air is connected. The response time is the period of time between switching to zero air and the time, when 90 % of the new gas concentration is detected by the analyser. This procedure was done ten times, and the averaged response time was determined to be 51.72 s.

Noise

The noise of a measurement are small fluctuations in the output signal, which do not correspond to actual change in the quantity to be measured, but to change in the signal caused by the limited precision of the instrument (e.g. short term pressure or temperature fluctuations in the cavity). Estimating the precision of the Picarro was done via the averaged 1σ standard deviation of 300 s measurement intervals within a 28 hours lasting measurement. The noise could be determined to be 0.16 ppb CH_4. The noise of the $\delta^{13}C(CH_4)$ measurement was calculated identically. The 1σ standard deviation of a 300 s measurement period is 3.7 ‰, what can be comprehended in Figure 14.
For one research flight (RF) of the CoMet 2.0 campaign, the isotopic ratio is shown in light red over the full period of the flight. The dark red line shows the measured methane concentration versus time. During the first part of the flight, ambient air was analyzed directly via a vacuum scroll pump. Approximately at 19:20 UTC, the mode was switched towards measurement of the tanks, were air samples are stored for an extended measurement subsequently (see Section 4.3 for more details). Each tank was analyzed for 10 minutes, therefore the methane concentration is constant during these periods. The noise of the raw $\delta^{13}C(CH_4)$ data is observable with hardly any dependence on the methane concentration. To circumvent this problem, it is necessary to average over longer intervals and thus improve the limited precision of the raw measurement. In the case of methane sources with small spatial extend,

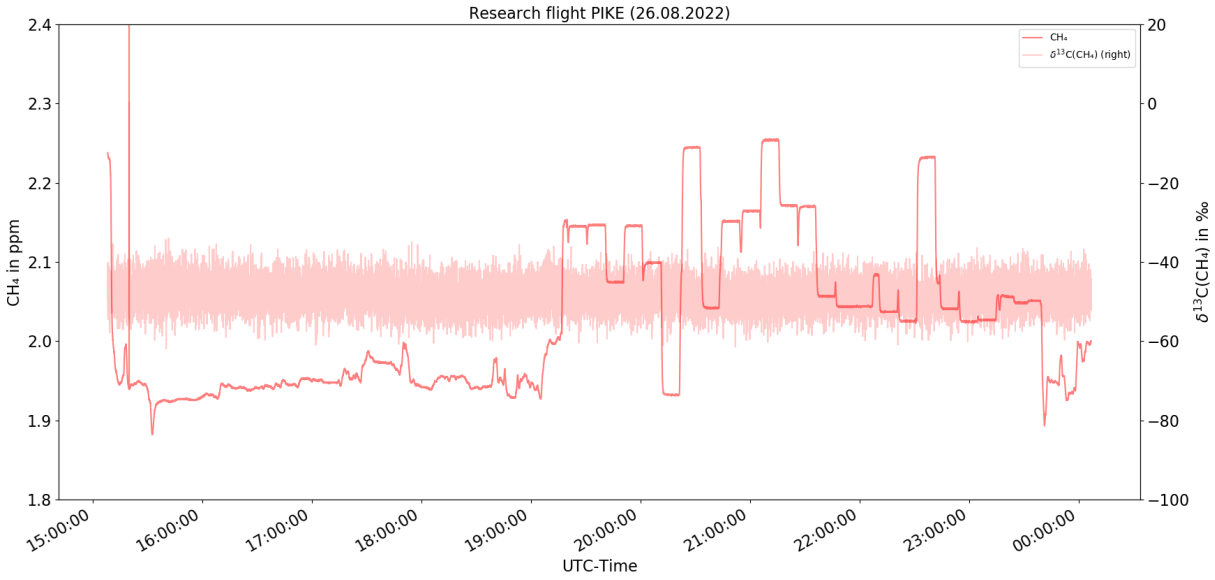

Figure 14: CH_4 and raw $\delta^{13}C(CH_4)$ signal versus time of research flight "PIKE". The measurement was switched from ambient to the sampled tanks at approximately 19:20 UTC. The strong noise of the isotopic ratio can be seen.

such as point sources (gas wells, pipelines, landfills), direct averaging over a period of several minutes without sampling smears the signal due to the high flight speed. To resolve the signal precisely, the air affected by the point source must be collected quickly and analysed as long as possible. Figure 15 shows the same flight as Figure 14, but in this case a 5 minute running mean over the raw data is plotted. Now trends and shifts in the signature are visible with the disadvantage of no longer having temporally high-resolution measurements. A ^{13}C depleted signature goes hand in hand with the tanks with high methane concentration. The noise for the measurement, if a 5 min mean from the raw $\delta^{13}C(CH_4)$ data is considered as a new measurement point, was determined to be 0.28 ‰. For this purpose, a test gas was measured for 90 min, the raw data of the isotope ratio were averaged over five minutes in each case, and then again the 1σ standard deviation of these means was calculated. Comparing the 0.28 ‰precision with the 3.7 ‰of the high frequency data, the method with averaging lowers the noise by an order of magnitude, thus bringing the measurement error into a range where source signatures can be distinguished from each other. The disadvantage of this is that the high temporal resolution data are no longer available, which in turn underlines the need for a sample collector with the possibility of intermediate storage in airborne applications.

Overall measurement uncertainty

To determine the total measurement uncertainty (u_{tot}) for methane and the carbon isotope ratio of the GHG analyzer, Equation (20) was adapted from Andrews et al. 2014. Contributions arise from the measurement precision (σ), the drift of the instrument, and the reproducibility of the primary gas standards, rep_{prim}. The latter one is taken from the manufacturers information. The last term, u_{H2O} is the error resulting from Picarros water vapour correction function, taken from Rella 2010 for a mean water vapour content of 1 % in volume, averaged over the whole mission phase.

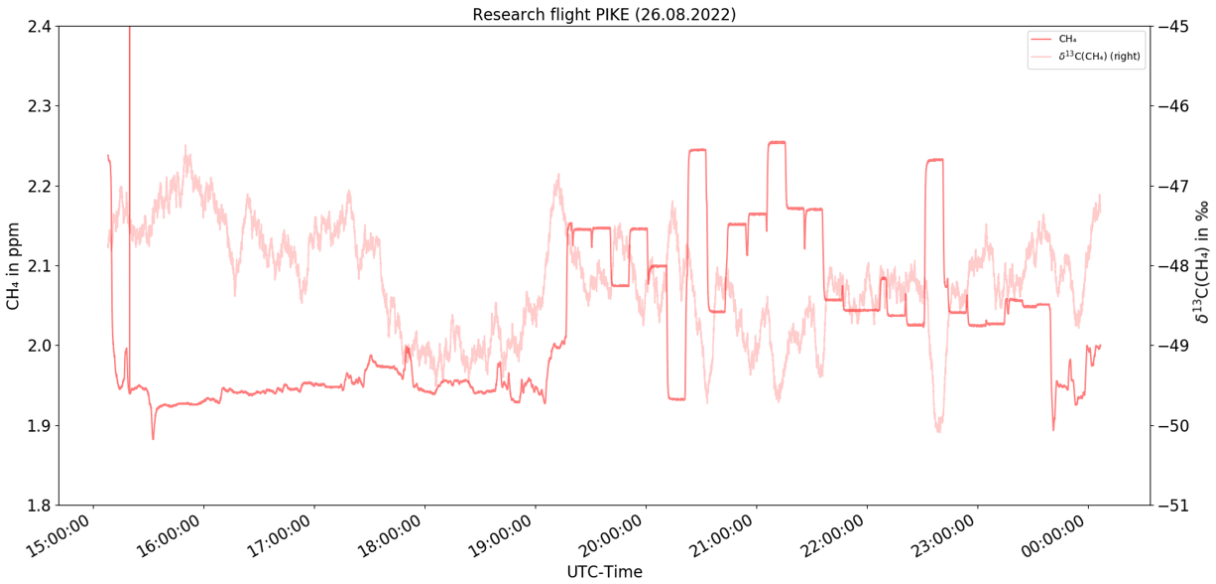

Figure 15: CH_4 and 5 minute running mean of $\delta^{13}C(CH_4)$ versus time of research flight "PIKE". The measurement was switched from ambient to the sampled tanks at approximately 19:20 UTC. By the rolling mean, a correlation between methane concentration in the tanks and the isotopic ratio is observable. The three tanks with highest methane concentrations showing $^{13}CH_4$ depleted signatures. The time delay between methane concentration and peak in the isotope ratio is caused by the rolling mean, which averages over the last 5 min.

$$u_{tot} = \sqrt{\sigma^2 + drift^2 + rep^2_{prim} + u^2_{H2O}} \tag{20}$$

Table 4 lists the contributions for the total CH_4 measurement uncertainty quantitatively. Hereby the error resulting from the drift is calculated with the evaluated drift of the instrument of 0.018 ppb/h multiplied with the typical duration of a research flight, being 10 hours. Thus, a overall uncertainty for the methane measurement is calculated to be 0.64 ppb.

	ΔCH_4 in ppp
Precision	0.16
Drift	0.18
Reproducibility	0.2
Water vapour	0.56
u_{tot}	0.64

Table 4: Contributors to the total CH_4 measurement uncertainty

In the same manner as for methane, the overall uncertainty for the $\delta^{13}C(CH_4)$ data could be obtained. As already mentioned in Section 4.2.1, no reference gases with known isotope ratios were available within the time frame of this work. Thus, there is no error resulting from the reproducibility of calibration gases known. The measurement precision σ was obtained in the laboratory and the uncertainty resulting from the drift of the analyser is taken from Picarro Inc. 2021, with 0.02 ‰/h, assuming again an averaged flight duration of 10 hours. As

dilution effects of other gases, including water vapour, tend to have the same effects on both methane carbon isotopes, and also the influence on the spectral line shapes are hardly equal for both molecules (Rella et al., 2015), the uncertainty resulting from the water vapour content is neglected for the isotope ratio. Consequently the total uncertainty u_{tot} for $\delta^{13}C(CH_4)$ is estimated to be 0.34 ‰. Table 5 summarises the total uncertainty for the carbon isotope measurement.

	$\Delta\delta^{13}C(CH_4)$ in ‰
Precision	0.28
Drift	0.20
u_{tot}	0.34

Table 5: Contributors to the total $\delta^{13}C(CH_4)$ measurement uncertainty

4.3 The MIRACLE sampler

In Section 4.2.2 it was shown, that for high precision $\delta^{13}C(CH_4)$ measurement, a longer analysis of the sample is necessary. Considering the intended use of the Picarro on the aircraft, it is evident, that averaging mixes signals of sources that are spatially close to each other. When targeting small scale or point sources to characterize their isotopic composition, such as single well gas facilities, refineries or landfills, the high speed of the aircraft results in short smoke trail traversal times and therefore makes longer, several-minute measurements of the source of interest impossible. To measure these small scale sources with high accuracy, the Picarro greenhouse gas analyzer has been supplemented with a sampler unit. Within some ten seconds, air samples are collected, for the extended measurement time in the further course of the flight. This sampler and the combination with the Picarro G2210-i to the overall instrument, called MIRACLE, are presented in this chapter.

4.3.1 Structure of the MIRACLE sampler unit

Sampling of air is necessary to achieve high precision measurements with the Picarro G2210-i for methane ^{13}C isotope, which are needed to provide specific and spatially resolved source signatures for methane budget calculations. The core of the sampler unit are six two liter stainless steel tanks, which are pressurised by a metal bellows pump. The tanks and the pump are shown in Figure 16.

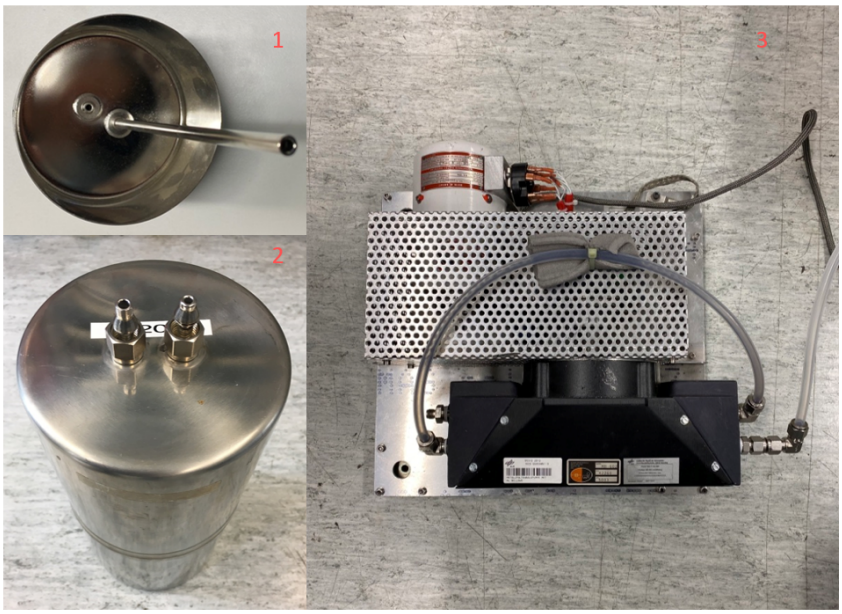

Figure 16: Picture 1 shows the interior of a stainless steel tank. The two pipes, for inlet and outlet, are of different lengths. Number 2 shows the whole cylinder and number 3 the metal bellows pump.

After the filling procedure, one tank can be analyzed, while more samples can be taken via the other five tanks. The measurement of one specimen therefore does not prevent the collection of further samples during the measurement period. Three-way solenoid valves are responsible for opening and closing the tanks. A mass flow controller (MFC) controls the outlet of the

tanks and the feed to the measuring device. Alternatively to using the sampler, ambient air can be analyzed directly, without being collected in advance. The latter option is realized via a vacuum scroll pump, which transports air directly from the inlet to the Picarro. This option is suitable for measurements where no source signatures are to be determined, but for large-scale gradients, e. g. in the free troposphere. A schematic gas flow plan is shown in Figure 17.

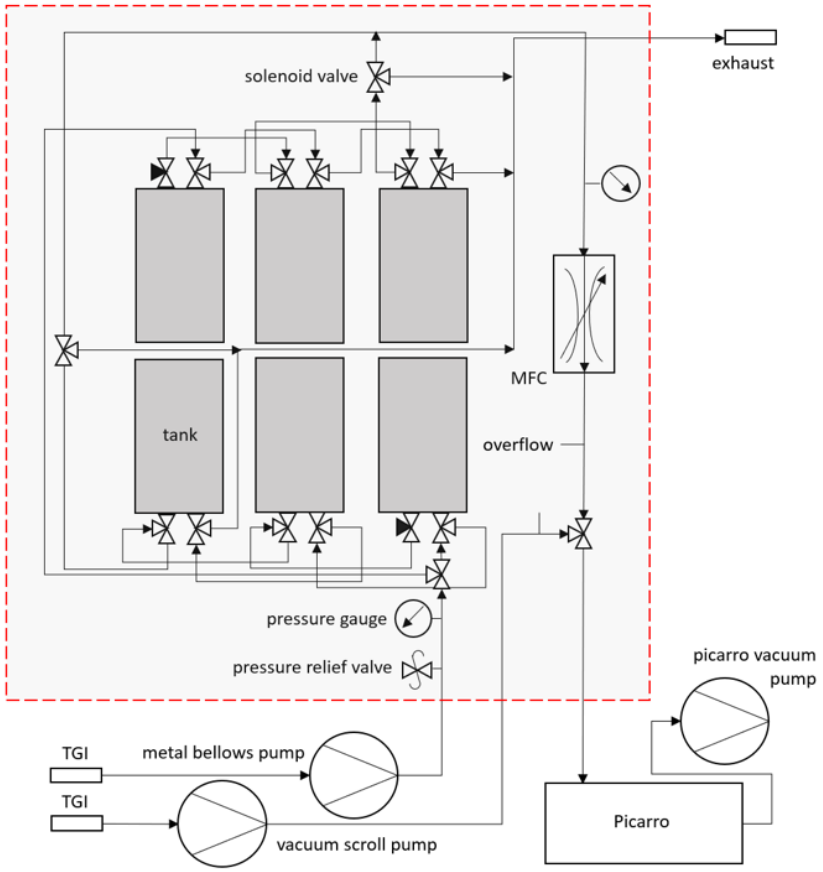

Figure 17: Gas flow sketch of the MIRACLE instrument. The red dotted line indicates the sampler unit, including the six tanks, valves, the mass flow controller (MFC) and the pressure gauges. The Picarro along with the Picarro vacuum pump, the metal bellows pump and the vacuum scroll pump are located outside the sampler box. The latter two pump the air from the trace gas inlets (TGI) of the plane to the sampler respectively the analyser.

As mentioned above, the metal bellows pump sucks air from the trace gas inlet (TGI) of the HALO aircraft and pressurizes the tanks. A pressure relief valve is installed in front of the tanks to protect the pump from damage in the event of strong excess pressure in the system. In the direction of the gas flow, a pressure gauge is installed, to monitor the inlet pressure, while the tanks are filled or flushed. Further downstream, a solenoid valve switches between the upper row, containing three tanks, and the lower row, also containing three tanks. Each tank has two solenoid valves, one on the inlet side, the other on the outlet side. The inlet and outlet valves of each row of tanks are connected in series, i.e. to fill the left tank of the lower row, the air also flows through the inlet valves of the middle and right tank of the lower row. On the output side, the valve of the left tank (lower row) is in first place, i.e. if the tanks

are flushed, for each tank the same number of valves is passed through. This guarantees the same flushing times for each tank. Downstream of the two tank rows, there is a valve that can direct the gas either towards exhaust (in case of flushing) or towards the MFC (in case of measurement). In front of the MFC, another pressure sensor is installed to check the outlet pressures of the tanks. Therewith it is registered whether there is pressure loss due to leakage, or if the system is operating well and the tanks have been pressurized to allow long measuring times. The last solenoid valve can supply the Picarro either with gas from the sample collector or directly with ambient gas that is provided by the vacuum scroll pump at the second TGI. Overflows on both sides, at the sampler unit and at the vacuum scroll pump, ensure that excess gas, which exceeds Picarro's flow of 25 ml/min are drained. The complete insertion, implemented on board HALO, as well as the inside of the sampler box is shown in Figure 18.

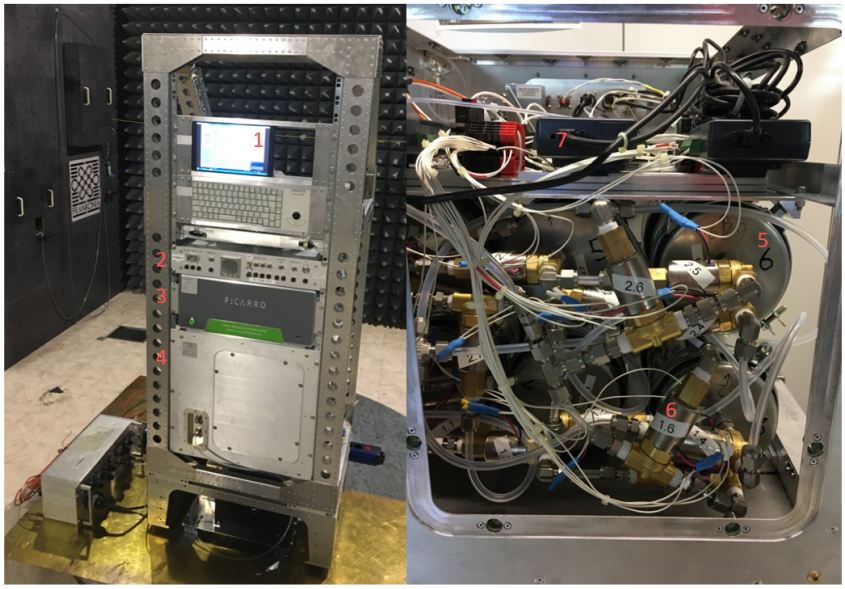

Figure 18: The left part of the picture shows the complete MIRACLE rack at the electromagnetic interference test laboratory, with the mission monitor(1), the power supply with computer (2), the Picarro analyzer (3) and the sampler box (4). On the right, the stainless steel tanks (5) and the solenoid valves (6) are shown, mounted in the box. The measuring cards, the mass flow controller, the pressure sensors and the pressure relief valve are installed on the intermediate level (7).

To ensure clean, contamination-free measurements with the MIRACLE sampler, the following chapter examines the performance of the individual components.

4.3.2 Performance of the MIRACLE sampler

Metal bellows pump

The metal bellows pump collects the gas, which is to be examined for the isotope signature, therefore it must be ensured that no gas from the cabin enters via leakage, nor that the sample gas is contaminated by particles released from the pump. There must furthermore

be no aggregation in the bellows. The metal bellows pumps operates without oil or lubricants having contact to the gas sample. Both, the inlet and the outlet valves, as well as the bellows themselves, are made from corrosion free stainless steel. Only the gasket material is Teflon. Therefore the pump is well suited for the use in sample collection, even if there can be methane release due to metal-metal friction in the bellows (Tohjima et al., 1991). The pump can generate flows of up to 60 l/min, thus offers the possibility to quickly flush and pressurize the tanks in the sampler. The flow is an important quantity, because it determines the duration of tank flushing. Thereby residual gas is removed from the tank, so that the new sample can be stored without adulteration and mixing. The pump flow is reduced by the resistance due to the tanks, hoses and valves and it also depends on the inlet pressure and hence on the altitude, i.e. the flight level (FL). The flow for the flush mode through the tanks, i.e. when the pump transports gas through one tank while inlet and outlet valves are open, was examined with a flow meter in the laboratory. Averaged over the six tanks, the mean flow was 19.1 l/min. There were differences between the individual cylinders of $\pm$ 0.3 l/min. By mounting a throttle and a pressure sensor at the beginning of the inlet hose, the flow that the pump can generate through the sampler could be simulated for different inlet pressures. At 850 hPa the flux was still 17.5 l/min, at 650 hPa it decreased to 12.3 l/min and for 450 hPa further to 7.6 l/min. In a separate series of experiments, the response time of the sampler as a function of the pump flow was investigated. Like the response time for the Picarro, the time after which 90 % of the new concentration were established was measured for the tank unit. This was done for different flows. For 10, 15 and 20 l/min, the response time of the tanks is 40, 20 and 15 seconds respectively. For the sampling strategy with the MIRACLE instrument, it is essential to know the flushing time for different FLs, to provide unadulterated samples.

Stainless steel tanks

The steel cylinders allow the storage and thus the extension of the measuring time of an air sample. With longer measurement time, averaging is possible and therewith the measurement is not longer restricted by the precision limits of the real time analysis. Since the sample gas remains in the tanks longer than in the other components of the sampler, and there are also large contact surfaces, it is important to also test the tanks for possible contamination. The storage time of samples within the tanks is in the order of some ten minutes up to a few hours (not longer than the duration of a RF with the aircraft), thus calibration gas was stored in the tanks for 90 minutes and analyzed afterwards, in order to see if concentration distorting processes arise. The methane concentration of the used AL bottle without storage in the tank was 1816.6 ppb. After 90 minutes dwell time, the concentration was 1816.5 ppb, hence within the precision limits of the Picarro (see Section 4.2.2) in agreement with the measurement without the tanks. For investigating whether isotope fractionation processes take place in the stainless steel tanks, $\delta^{13}C(CH_4)$ was also measured before and after the 90 minutes storage period. The analysis of the first mentioned case gave a signature of -51.51 ‰, the case including tank storage a signature of -51.03 ‰. Accounting for the precision for the 5 minute mean $\delta^{13}C(CH_4)$ measurement, which is 0.28 ‰, the isotope ratio was as well unaffected by the tanks. The interior of the cylinders is designed in such a way that the inlet consists of a thin pipe that reaches far into the tank, while only a short pipe is used for the outlet. Thus, while flushing the tank, mixing is guaranteed, and no stratification builds up.

Solenoid valves and tubing

SMC VDW 300 valves were used for opening and closing the tanks, as well as switching between the two modes of operation. They are made of brass and have seals that are made of nitrile butadiene rubber. The latter does not undergo reactions with hydrocarbons and is therefore well suited for the use in the MIRACLE sampler (American rubber Corp, n.d.). Perfluoroalkoxy alkane (PFA) is the material, of which the tubing of the sampler unit and the connections to the TGIs is made of.

Comparison of measurements with JIG

Aboard the aircraft, a second Picarro GHG analyzer was operated. The Jena Instrument for GHG measurements (JIG) is based on the same principle as the Picarro used for this work, but instead of the isotopic ratio and ethane, it detects the ambient carbon monoxide (CO) concentration. As both Picarros aboard HALO are able to record the methane concentration, a comparison of the measurement of the two instruments was done. Since JIG is a well established system (Amediek et al. 2017, Gałkowski et al. 2021) and does not have a sampler unit for storing the gas, as MIRACLE does, this measurement comparison can be used in particular to determine the extent to which the components of the sampler unit eventually influence the methane measurements. For the main components of the MIRACLE sampler, this was done also in the laboratory, in particular for the essential parts, the metal bellows pump and the stainless steel cylinders. Nevertheless it was not possible to study the influence of the sampler on the methane measurement under real flight conditions, i.e. including the complete instrument as a whole, the TGIs and the changes in external pressure, temperature, etc. associated with the flight. Thus, JIG data are valuable to validate and characterize the measuring principle of the newly constructed MIRACLE sampler. JIG methane and carbon dioxide measurements and those of MIRACLE should follow the same shape, when MIRACLE is operating in the mode without intermediate storage, i.e. gas is transported via the vacuum scroll pump directly to the analyzer. In Figure 19 the methane data from JIG (light red) and MIRACLE (dark red) are plotted versus time for the research flight "PIKE", which took place on 26.08.2022.
During the first part of the flight, MIRACLE was operating without sampling in the tanks, therefore the curvature of both measurements look the same. But the measurements of MIRACLE show a slightly backward time lag compared to JIG. This lag is the result of differences in the flows of the analyzers and in the length of the inlet pipes. The time delay between a signal is detected by the instruments is approximately 94 s. When the plot is corrected for the lag, the measurements are identical, what can be seen in Figure 20, were the part of the flight during which the MIRACLE instrument analyses ambient air is depicted.
For the directly comparable phase of the flight, the mean of the absolute concentration difference between both analyzers was found to be 1,6 ppb. Accounting for the the total CH_4 measurement uncertainty of 0.64 ppb from the MIRACLE instrument (see Section 4.2.2), and considering the indication of the operators of JIG, that its precision is 1 ppb for methane, the deviation of the the two measurements agrees already within the scope of the inaccuracies.

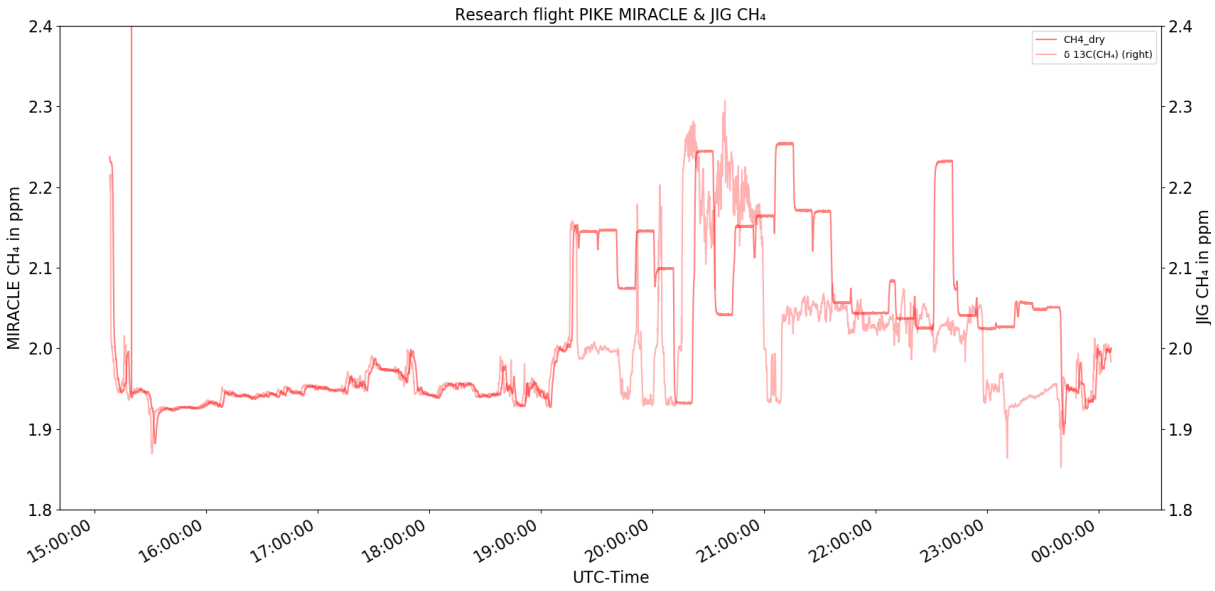

Figure 19: For the research flight PIKE, the CH_4 data computed by JIG and MIRACLE are shown versus time. Until approximately 19:20 UTC, the measurement mode of MIRACLE was excluding the tanks, thus sampling gas directly from ambient. The methane curves have the same shape, but there is a time lag observable.

Furthermore Figure 20 shows, that the extremes of the two measurements differ in their peak concentrations. JIG shows higher concentrations for the peaks, and lower ones for the dips, than MIRACLE does. This is again related to the different fluxes of the two instruments. JIG has a higher flow rate and a higher measurement frequency, therefore the sample turnover time within the cavity is shorter. As a result, JIG is more sensitive to sharp peaks in concentration than MIRACLE. The low gas flow of the latter causes such sharp signals to be flattened and smeared. The smearing of the signals is not excluded from the calculation of the difference in CH_4 concentrations, thus the calculated deviation of 1,6 ppb would be even lower without the signal flattening from MIRACLE. The consistency of the measurement results while MIRACLE was operating in the second mode, i. e. during the analysis of intermediate stored gas from the tanks, can also be verified using the data from JIG. For this purpose, the mean CH_4 concentration of each tank is compared to the averaged methane concentrations, measured by JIG during the period, when the respective tank has been flushed and filled. These averaged concentrations are of course less comparable than the measurements from ambient, which is due to different reasons. While the tanks are flushed, the gas is transported through the sampler, but at the time when the outlet valve closes the tank, the air which is in the cylinder at this moment, remains there and thus is part of the analysis. If a sharp but high signal is sucked through the tank during flushing, it is crucial whether this signal was part of the flushing gas at the beginning or at the end of the process. If the latter scenario was the case, more enhancement of the signal will remain in the tank and contribute to the overall mean tank concentration, while only small parts of a signal at the beginning at the flushing process will remain in the tank until closing. On the other hand, the averaged concentration measured by JIG during the flushing and filling will always include the undiluted signal in full. The second reason for the reduced comparability has a similar cause as the first, but it occurs

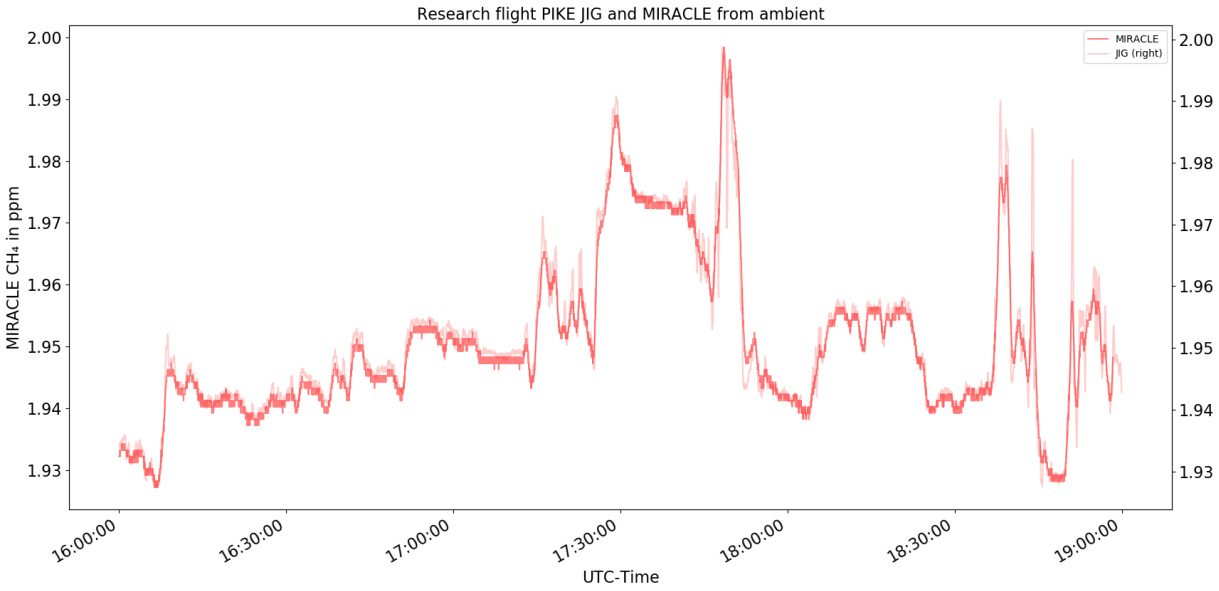

Figure 20: The part of RF PIKE, were the concentrations evaluated by JIG and MIRACLE are comparable directly, is shown with the time lag correction of 94 s. The peaks and dips in methane are congruent time wise.

during filling. After the tank outlet is closed, the metal bellows pump pressurises the tank. With increasing tank pressure, the flow, which the pump generates, decreases. Thus during the filling, a methane enhanced or depleted signal will influence the tank concentration more dominant, if it is part of the beginning of the process. This effect is further amplified if the pressure relief valve, installed in front of the tanks takes effect, i.e. the tank is already filled and gas is pumped only into the exhaust pipe for the remainder of the filling process. Again, JIG will detect the signal without weighting caused by time dependent fluxes or dilution. Both effects mentioned here cannot be extracted from the data without considerable effort, which results in the lower comparability of the concentration measurements for the case of analysis of the tanks compared to the analysis of ambient air. Nevertheless, it provides information about whether the concentrations are grossly distorted by the design of the MIRACLE sampler, or are in the same order of magnitude as those recorded by JIG. Figure 21 shows the second part of the research flight "PIKE", when MIRACLE was in the mode of sampling and measuring the tanks. The CH_4 concentrations, measured from the MIRACLE tanks (red points) are located on the continuous methane measurement curve of JIG (light red). There is no suspicion that the sampler unit distorts the actual methane concentration.
To investigate the difference between the concentrations measured ambient and those from the tanks, the 20 cylinders filled during the research flight "PIKE" are compared to the corresponding JIG measurements. If there were a reproducible, systemic distortion of methane concentrations, one would expect that the deviation of methane in the tanks from that measured by JIG would tend in one direction, i.e. systematic methane enrichment or deposition. Furthermore, the deviation should be in the same order of magnitude for each pair of tank and JIG measurement. During the flight, the flushing and filling time were set to 20 s each. Hence the total time of the sampling process was 40 s. For these 40 seconds, the JIG methane data were averaged, so the concentration can be compared with those of the tanks. The mean

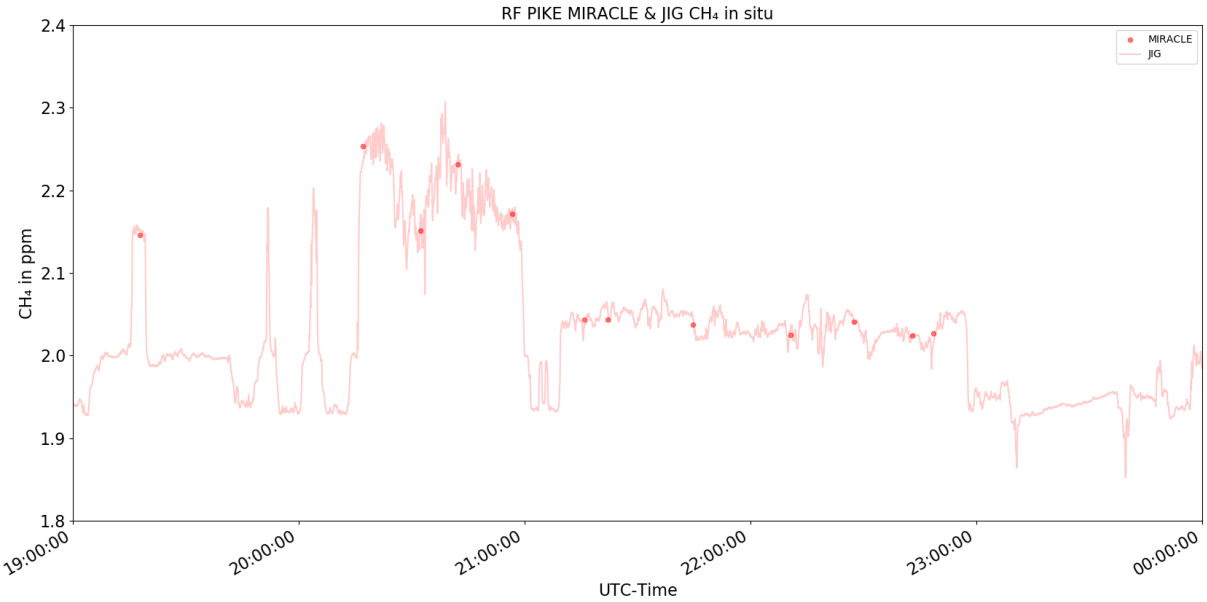

Figure 21: The part of RF "PIKE" is shown, were MIRACLE analyses samples of the tanks. Ambient continuous CH_4 measurement from JIG is depicted in light red. The red dots indicate the measured methane concentration of the tanks. Tank concentrations and simultaneous ambient concentrations measured by JIG are consistent.

difference in CH_4 measured by both instruments was found to be -2.7 ppb, with MIRACLE measuring the higher concentrations, averaged. For 14 of the 20 tanks, the discrepancy was less than 10 ppb. One of the two tanks with the largest difference to JIG data showed a deviation of -54.1 ppb, the second pair was separated by +49.3 ppb. Therefore, no shift towards methane enriched or depleted samples is observable. The mean deviation of -2.7 ppb is small, almost in the range of measurement inaccuracies of the two instruments. Figure 22 shows the density distribution of the differences in CH_4 concentrations measured by JIG and MIRACLE.

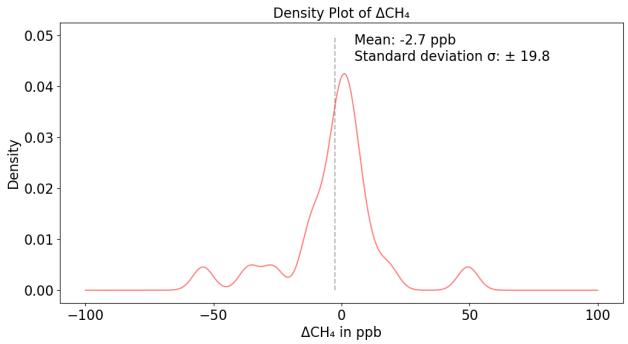

Figure 22: Density distribution for the differences between the tank CH_4 concentrations of MIRACLE and the concentrations measured by JIG during the filling in ppb. The grey dashed line indicates the mean deviation of -2.7 ppb. The standard deviation is $\pm$ 19.8 ppb.

Taking into account the limitations of comparability between the two measurements, the observed differences do not indicate contamination of the gas by the MIRACLE sampler unit.

5 $\delta^{13}C(CH_4)$ determination for selected targets of CoMet 2.0 arctic

After it was shown in Chapter 4, that the MIRACLE instrument is well suited for the precise assessment of methane carbon isotope ratio, this chapter describes different methane source signatures determined by MIRACLE in the course of the CoMet 2.0 campaign, including the corresponding error estimation and the discussion in context of literature.
The first part of the chapter presents the selected target areas, which are used to demonstrate the calculation of the isotope signature using the data obtained there and the designated flight patterns.
In the second part, the determined isotope ratios are discussed in terms of their uncertainties and assigned to the respective methane formation processes.

5.1 Study site description and sample strategy for the MIRACLE instrument

The previous Chapter 4 gave an introduction to the measurement technology of the MIRACLE instrument, presented the measurement uncertainties and showed that the arrangement of the analyzer and the sampler allows precise and unbiased methane carbon isotope signature identification. Section 3 gave a rough overview of the CoMet 2.0 campaign and already presented some of the probed areas. This section is now intended to show how the instrument was used on the research flights with the aim of determining $\delta^{13}C(CH_4)$ signatures.

General sampling strategy

Methane shows highest concentrations in the PBL, since the sources are typically located on the ground. As discussed in Section 2.2.4, high GHG concentrations of the source of interest are favourable for the determination of the isotopic signature of the corresponding emitter. For point sources, such as refineries, landfills, coal mines etc., highest concentrations are found in the exhaust plume, which follows the wind direction and gets diluted in the PBL by time. Therefore in case of point sources, the aim for $\delta^{13}C(CH_4)$ measurement is, to take samples in the exhaust plume, near the location of emission, to get samples with high concentration enhancement. Because the PBL height determines the volume in which the emissions are distributed, a lower boundary layer height leads to increased GHG concentrations. Thus for areal sources, like wetlands, rice paddies or agricultural regions, the varying boundary layer height can be used to optimize the sampling. In the early morning, accumulation of emissions in the shallow SBL causes higher concentrations of trace gases trapped within the boundary layer, than during a fully expanded ML in the afternoon. Additionally the near surface winds are also driven by solar radiation, which means higher wind speeds, which counteract the accumulation of emissions and favour their mixing, tend to occur during daytime. A situation with shallow boundary layer height and low wind speeds is thus the advantageous scenario to do airborne $\delta^{13}C(CH_4)$ measurement on areal methane sources. In both cases, for the point sources as well as for the areal sources, the sampling times were determined based on the real time measurements of JIG. JIG has a much faster response time (7-14 s) than the Picarro of

the MIRACLE instrument has (51.72 s) and in addition the instrument flow is higher, which means that the sample tunrover time within the cavity is faster and therefore sharp and extreme signals are less broadened compared to MIRACLE. Thus, tanks which are filled based on the measurements of JIG are temporally closer linked to the actual ambient air concentrations due to the lower time delay, which makes filling more predictable. Especially in the case when MIRACLE measures already filled tanks, it is dependent on JIG for simultaneous further sampling. Since MIRACLE no longer records ambient concentrations during the analysis of tanks, only blind sampling would be possible without JIG at this point.
In Section 4.2.2 it was discussed, that for precise determination of the isotope ratio, averaging over longer analysis times is suitable. Thereupon Section 4.3.2 showed how this extended measuring time can be implemented with the help of a sampler unit while maintaining the purity of the measuring gas. In the course of the latter discussion, the flow dependent flushing time, which is necessary to prepare thoroughly flushed tanks was probed for different altitudes. The flushing time for the boundary layer flights in the course of CoMet 2.0 was determined to be 20 s. This in turn means that at least 90 % of the tank concentrations should have been adapted to the currently collected gas, for all flight levels up to 750 hPa, i.e. approximately up to 2500 m above mean sea level. Since the overall measurement uncertainty for 5 min averaged $\delta^{13}\mathrm{C}(\mathrm{CH}_4)$, with 0.34 ‰ is proportionate for clear methane source signature determination, the tank measurement time was set to be 10 min. This ensures the possibility of a 5 min averaging, after a stabilization period of a few minutes beforehand. Thus, for all study sites, which were probed within the PBL, the cylinders were flushed for 20 s and analyzed for 10 min. The flushing time was set to 40 s for samples, taken at elevated flight levels. The pressurisation of the tanks lasts 20 s, which corresponds to approximately 2400 m, when accounting for the speed of HALO at low FL, which is 120 m/s.

5.2 Study site 1: Lake Winnipeg wetlands

The first case of an isotope determination is performed for an areal natural methane source which was probed with HALO in the course of the campaign. The lake Winnipeg wetland area is located in Manitoba, around the three freshwater lakes, lake Winnipeg, lake Winnipegosis and lake Manitoba. The coastal marshes around these areas are believed to be the largest of North America (Wrubleski et al., 2016). Figure 23 gives an impression of the swampy landscape.

Figure 23: The Lake Winnipeg wetland area seen from HALO

On 26.08.2022 the ninth research flight of the campaign, called "PIKE" was completed with the aim of investigating the lake Winnipeg area for methane. The duration of the ferry flight from and back to Edmonton was approximately 1.5 hours each and the part of the flight, were the FL was optimized for the remote instruments at 8200 m above mean sea level, lasted another 3 h, there were 4 h remaining for the in situ flight pattern. The in situ part of the flight was performed at low FL and beforehand a low approach over Thompson municipal airport was executed. Figure 24 shows the flight path, starting from Edmonton, via the area north of Lake Winnipeg, which is the largest of the blue coloured bodies of water, back to Edmonton. The individual flight tracks have a northwest to southeast orientation, as the wind came constantly from southwest. The spike in the very north of the flown pattern results from the low approach over Thompson municipal airport, which was done in order to be able to collect data as close to the ground as possible. In the low approach, the aircraft is on approach, but does not touch down on the runway, instead pulls up and goes around just before it. As mentioned in the outline for the sampling strategy, MIRACLE sampling is to occur within the PBL, because the methane emissions of the source of interest are accumulated there. The PBL height was determined by the temperature and humidity profiles of the low approach over Thompson. The water vapour concentration is recorded by JIG and the ambient temperature by the BAHAMAS instrument, both profiles can be seen in Figure 25.

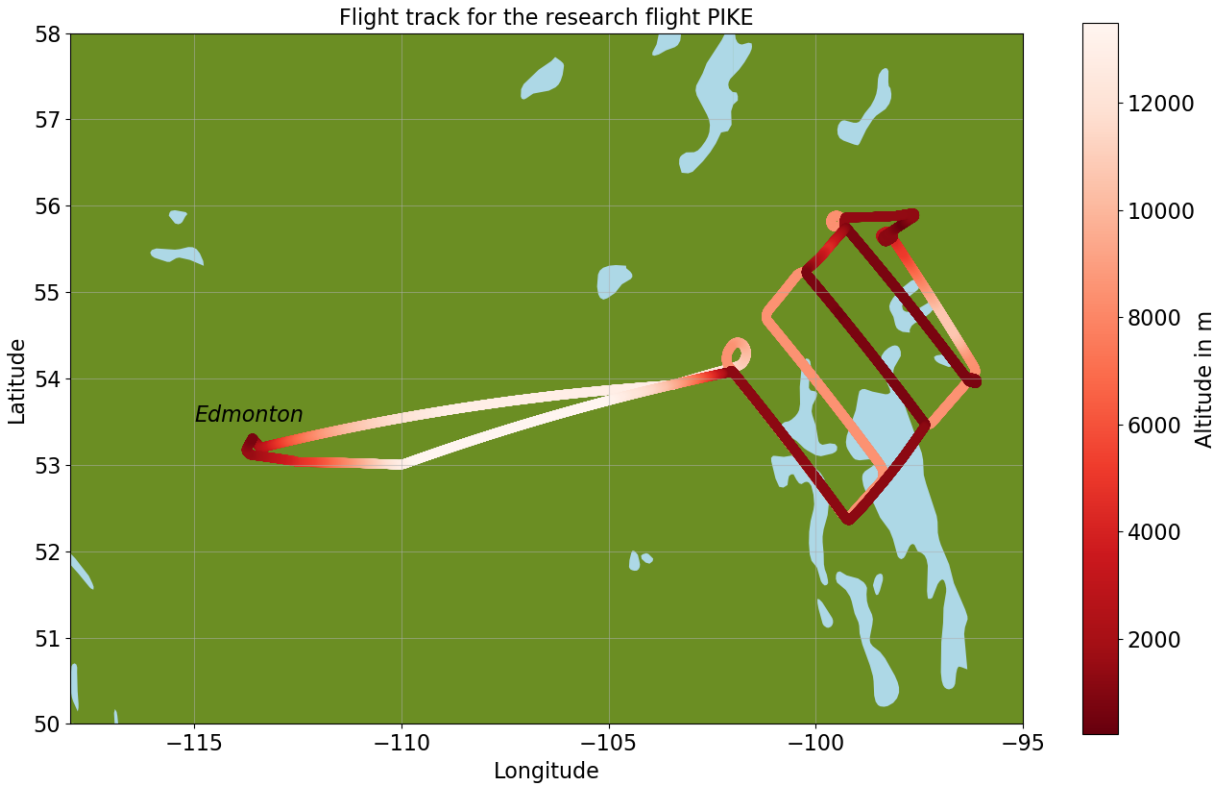

Figure 24: The HALO flight pattern of the research flight "PIKE" is shown. The colour code represents the altitudes above mean sea level, at which the corresponding parts were flown. The dark red colour over and in the north of lake Winnipeg indicates the part of the flight at low altitudes, i.e. during the in situ measurements.

The sharp temperature inversion and the steep increase in the H_2O concentration at an altitude of approximately 700 m above ground determine the PBL height (dashed line in Figure 25). The low approach took place at 19:18 UTC, thus at 12:18 CDT (central daylight time, local). The ML is therefore not fully developed, i.e. the PBL height of 700 m is a lower limit estimation for the subsequent in situ part of the flight. Figure 26 displays the flight level of HALO and the water vapour concentration measured by JIG for the in situ part of the RF "PIKE".
Large parts of the flight took place below the 900 m mark, hence clearly within the PBL. Towards the end of the in situ pattern at approximately 21:50 UTC the flight altitude had to be raised so that it was above 900 meters. The water vapour concentration remained mostly constant after the raise to approximately 1300 m, thus indicating that the flight was still beyond PBL top. Therefore the ML height evolved by time. Nevertheless, individual brief drops in water vapour concentration suggest that HALO was flying at the upper edge of the PBL. In summary, this confirms which samples were taken in the PBL and are therefore suitable for wetland isotopic signature analysis.
Methane was observed to be highest in the northeastern most, i.e. downwind track of the flight, with maxima of 2.3 ppm, which corresponds to roughly 250 ppb increase to the upwind part. Methane measurements from MIRACLE and JIG are plotted over the flight track in Figure 27.

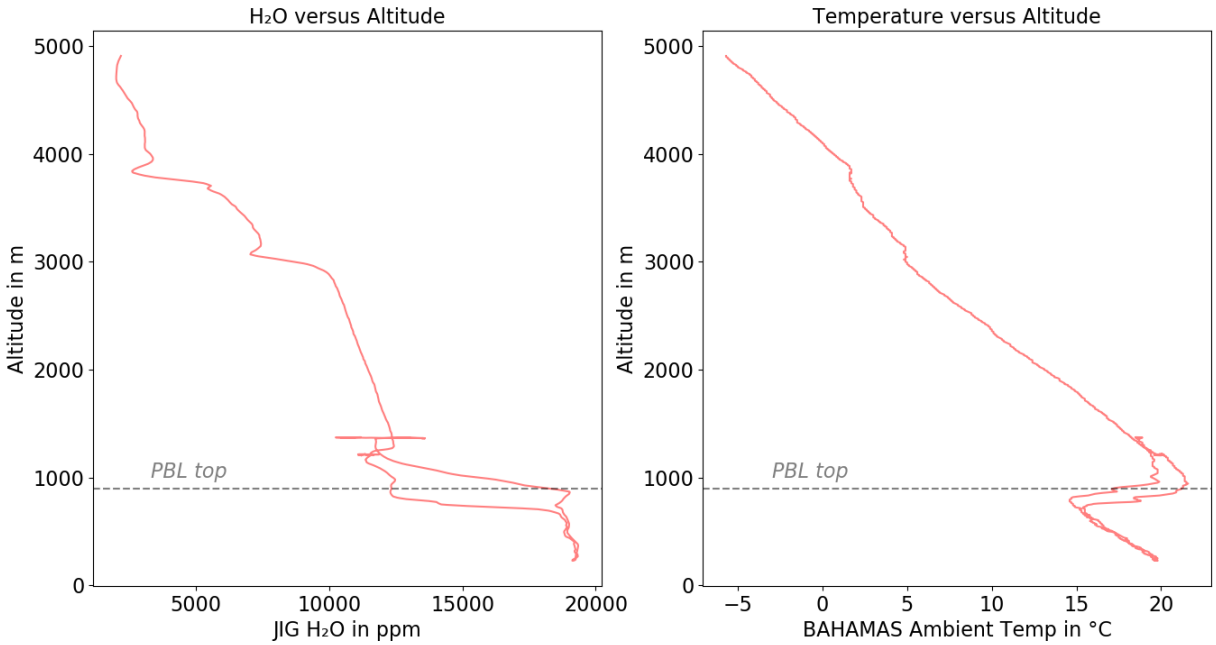

Figure 25: Humidity and temperature profiles are shown for the low approach at Thompson airport. The two lines for each plot correspond to the descend towards the airport and the ascent after the maneuver. The water vapour concentration shows a significant increase beyond 900 m. At the same altitude a clear temperature inversion is observable. Thus, the PBL top (dashed line) is found to be at 900 m above mean sea level, i.e. at 700 m above ground.

The continuous analysis of ambient air by JIG represents the actual spatial spread of methane over the area, while the concentrations determined by MIRACLE are only available for the single spots, where samples were taken. When plotting the 5 min averaged $\delta^{13}C(CH_4)$ values of each tank versus the spots of the associated sampling, the result is Figure 28. It is important to note that the tanks, with the most negative isotope signatures, were collected where the largest methane elevations were found, i.e. in the northeastern part of the area. For a change in the isotope composition one would also expect a change in the methane concentration, so this overlap suggests that both the increase and the shift in the signature are due to the same methane source.
The methane analysis of the tanks revealed maximum concentrations of 2.2539 ppm and minimal ones of 2.0245 ppm. The isotopic ratios ranged between -48.04 ‰ and -49.91 ‰, thus are clearly distinguishable with the precision of the 5 min averaged measurement (0.34 ‰). As set forth in Section 4.2.2, the precision of the not averaged data is 3.7 ‰, which implies that the differences in $\delta^{13}C(CH_4)$ observed during the research flight PIKE would not have been reliably separable from one another with this precision, once again highlighting the need of the sampler unit.

In order to determine the isotopic signature of the whole area, all of the data points shown in Figure 28 are included for the Keeling plot (see Section 2.2.4). The data and the corresponding linear regression are depicted in Figure 29.

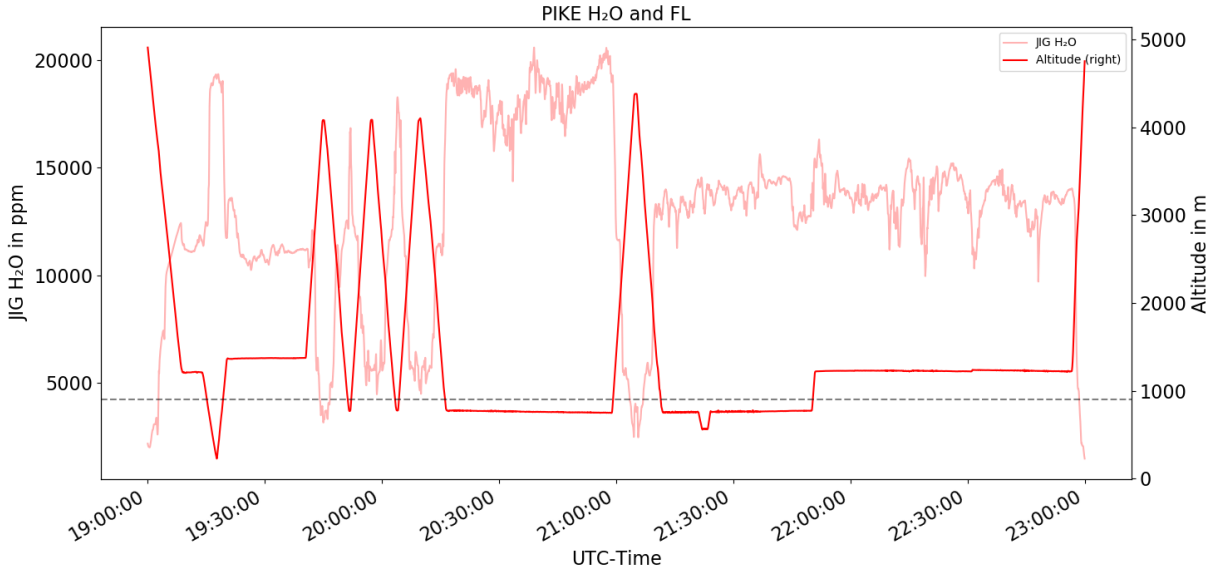

Figure 26: The HALO FL of the in situ part of the PF PIKE is shown on the right axis and depicted in bold red. The humidity measured by JIG is plotted in light red and scaled on the left axis. The lower limit estimation of the PBL height (900 m above mean sea level) is represented by the dashed line. A raise in the FL towards 1300 m took place at 21:50 UTC, after which the water vapour concentration exhibit short drops.

The linear regression yields an extrapolated intercept of -61.95 ‰with a standard error of the intercept of ± 1.70 ‰, calculated via Equation (10) in Section 2.2.4. The error is caused by the inaccuracy of the predicted regression, which is due to three reasons. The first one is the limited data coverage - by a larger range of methane enhancement and corresponding $\delta^{13}C(CH_4)$ values, the best fit linear regression is more reliable. The second contribution to the error arises from the limited instrument resolution, which can smear the correlation between the measurements. The third is reduced correlation, due to the mixing of varying amounts from different methane sources. The latter includes, that there might be samples influenced by different methane emitters with different isotopic signatures, and also emissions from the same source, but mixed into different backgrounds.
With the given error of 1.70 ‰, the intercept is identified within a 68 % confidence interval. An indication of the uniqueness of the data set is also given by the coefficient of determination, R^2. If R^2 is close to zero, the measurement points are insufficiently explained by the model, whereas for $R^2 = 1$, there is perfect correlation. Thus, for the data from the lake Winnipeg area, a high degree of correlation ($R^2 = 0.858$) between the methane concentration and the corresponding isotopic ratio is assessed.
The resulting error for the intercept, can be further analyzed in order to be examined for its individual contributions, i.e. what is the contribution of the measurement uncertainties or the mixture of sources. In this regard, the data points can be varied by the uncertainties of the measurement, to see their influence on the error range of the signature determination. The total measurement uncertainties were determined to be 0.64 ppb for methane and 0.34 ‰ for the isotope ratio respectively. The inaccuracy of the $\delta^{13}C(CH_4)$ values can be included directly. But as the reciprocals of the methane concentration are used for calculating the

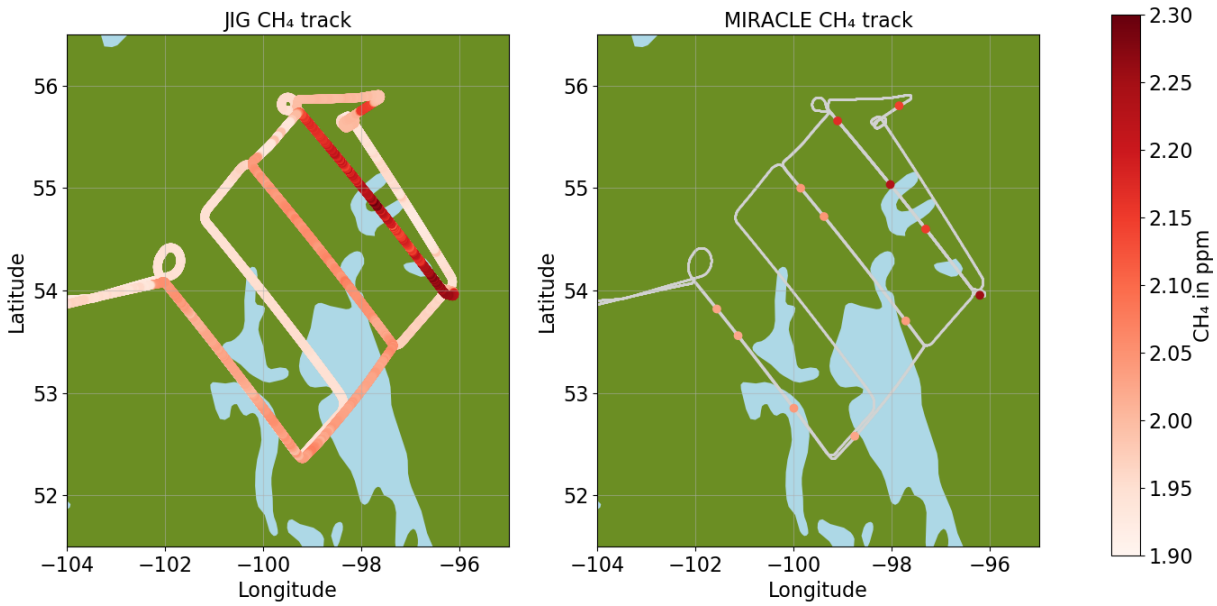

Figure 27: The CH_4 measured by JIG and MIRACLE is plotted over the flight track of HALO for the target region only. On the high altitude remote sensing flight level, the concentration is between 1.9 and 2.0 ppm, while for the low level part over the target area, there are maxima of up to 2.3 ppm, especially for the northeastern most flight tracks. The data of MIRACLE are only covering single spots, i.e. the measured concentrations correspond to the locations where the tanks were filled.

Keeling plot, the uncertainty for them is computed via a Taylor expansion for error propagation to the quadratic term, as higher order terms converge towards zero for small fluctuations. See Equation (21), adapted from Xue et al. 2015.

$$y(x+\Delta x) = y(x) + \frac{1}{1!}\frac{dy(x)}{dx}\Delta x + \frac{1}{2!}\frac{d^2y(x)}{dx^2}\Delta x^2, \tag{21}$$

Δx corresponds to the uncertainty of the methane measurement (x), and $y(x) = \frac{1}{x}$. Since the error ranges of both quantities, which are included in the Keeling plot, are known, the resulting uncertainty of the linear regression can be determined. Since every change in the measurements would lead to a slightly modified linear best fit model, the number of possible regressions is large. Therefore it is advisable to solve the problem numerically, e.g. by a Monte Carlo simulation, as presented in Landau and Binder 2021. To do so, an ensemble of linear regression models was calculated, each with different variations of the input parameters. The variations were implemented as normally distributed and are in the range of the total inaccuracies determined for methane and the isotope ratio, 0.64 ppb and 0.34 ‰ respectively. As the law of large numbers sates, that the average of outputs from a series of the same experiment converges to the expected value for a large number of trials, the number of trials was set to $N = 10000$. The input parameters were chosen to be the measured data, projected on the line of best fit. This means, the reciprocals of the measured methane data were used for computing the corresponding best fit $\delta^{13}C(CH_4)$ values, via the slope and gradient of the best fit regression. Table 6 provides an overview of the input parameters of the Monte Carlo simulation and the corresponding results.

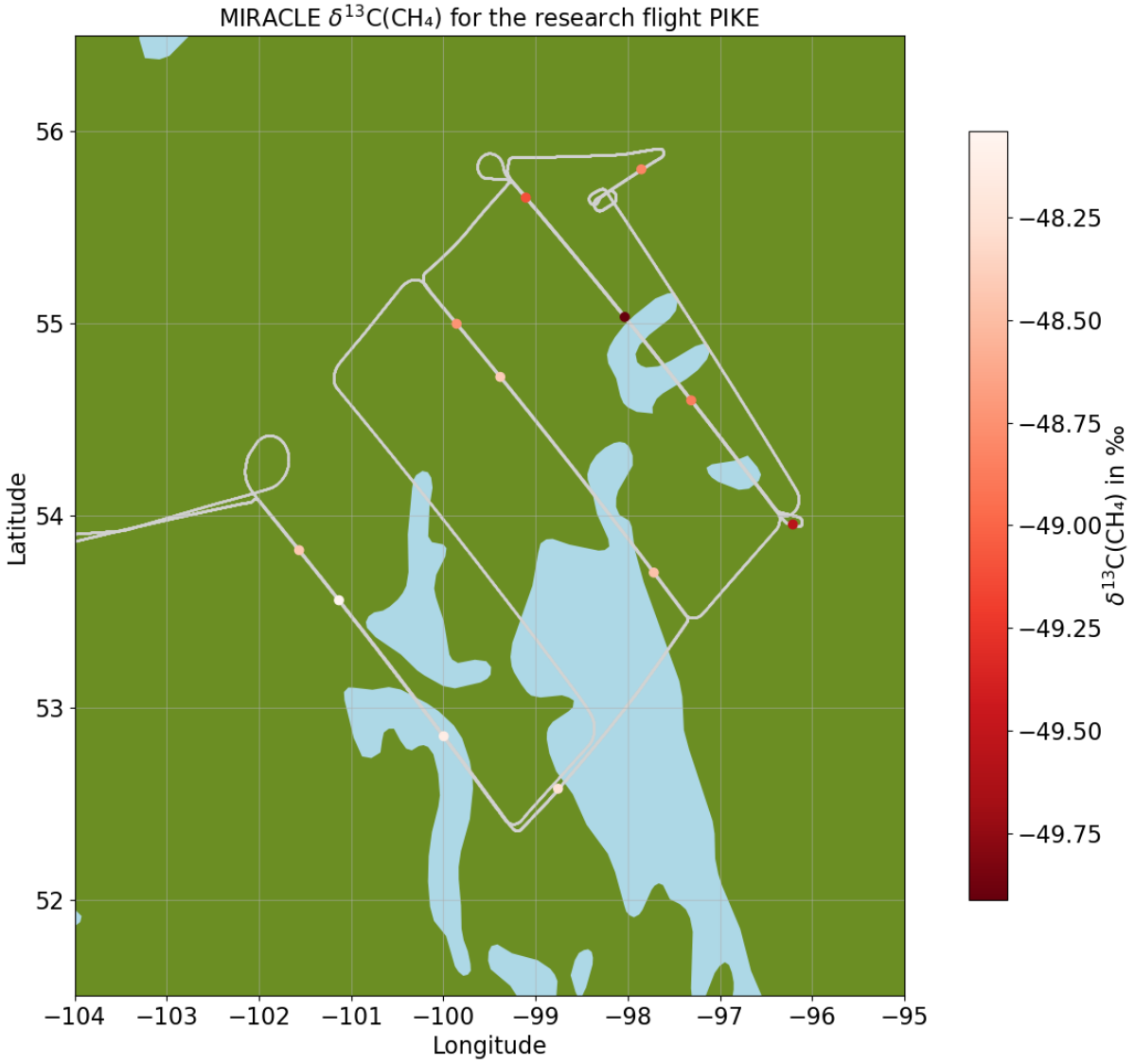

Figure 28: The spots where samples were taken are coded in color with their corresponding $\delta^{13}C(CH_4)$ ratio. A few of them are overlapping, thus there were more samples taken, than displayed in the plot. It should be noted that the tanks in which isotope ratios, which differ most from the background, were collected in the northeastern flight leg. The largest concentrations of methane have also been detected there.

By the use of the fitted data as input, it is assumed that there is perfect correlation between them, which in turn means, the data are collected only from one source of methane, mixed into a known and uniform background. By doing so, one can compare the error of the best fit, with the mean ensemble intercept error. Table 6 shows, that the best fit intercept error with ± 1.70 ‰ is smaller than the ensemble spread of the intercepts with 2.63 ‰. The averaged ensemble intercept error is found to be 2.56 ‰, with a corresponding standard deviation of 0,60 . This means that the error of the data taken into account for the analysis is explained by the pure measurement uncertainty with a probability of 7.6 %, as the best fit error lies within 1.43 standard deviations of the ensemble mean intercept error. Possible explanations are on

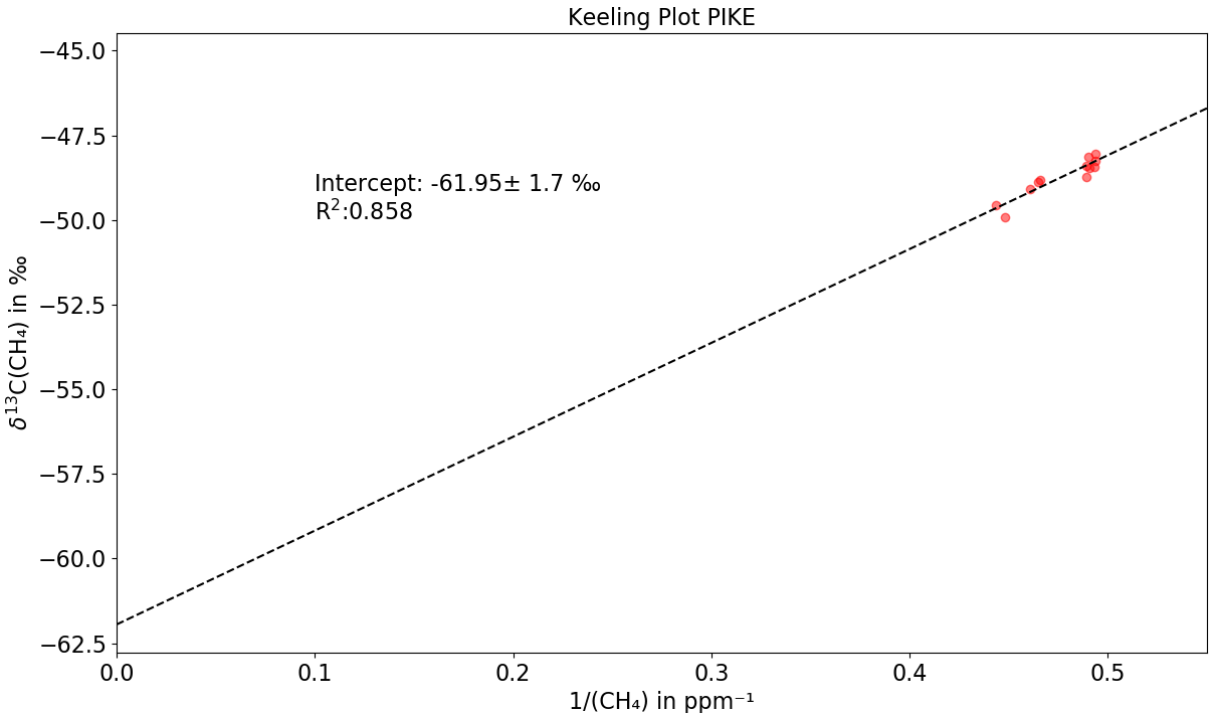

Figure 29: The Keeling plot for the measurements from RF PIKE is shown. Red dots indicate the single tank measurements, with the reciprocal CH_4 concentration mapped on the abscissa and the $\delta^{13}C(CH_4)$ ratio on the ordinate. The linear regression with the intercept is plotted as dashed line. R^2 value and the standard error of the intercept are also given.

the one hand, that the measurement uncertainty, investigated in the laboratory are estimated higher than the true one is, or, that there is correlation in between the measurement uncertainty, i.e. the data points do not have measurement errors which are independent of each other. The latter one could be the case, when the drift of the analyzer is not negligible on time scales between the measurement of the tanks. Nevertheless, the determination of the lake Winnipeg methane carbon isotope signature is still well constrained when accounting for the mean ensemble intercept error of 2.56 ‰.

In favor of a clearer representation, only 100 out of the 10000 performed Monte Carlo trials are plotted in Figure 30, which again shows the Keeling plot, but this time the intercept uncertainty was calculated via the Monte Carlo ensemble.
The uncertainty ranges are shown for the data obtained by MIRACLE as red bars. For the reciprocal methane concentrations, the errors investigated via Taylor expansion are small, thus not visible in the figure, but included in the Monte Carlo simulation. The spread of the intercepts of the Monte Carlo ensemble is used to determine the error range for the intercept. Figure 30 shows that the error of the source signature ($\pm$ 2.56 ‰) is larger than the best fit intercept error ($\pm$ 1.70 ‰), but still low enough to allow for clear methane source determination.

Monte Carlo simulation for PIKE	
Input:	
Ensemble size	N = 10000
Best fit intercept	-61.95 ‰
Best fit intercept error	1.70 ‰
Input parameters	data projected on best fit
Variations	$u_{tot}(1/CH_4)$, $u_{tot}(\delta^{13}C(CH_4))$
Output:	
Spread of ensemble intercepts	2.63 ‰
Mean of intercept error	2.56 ‰
Standard deviation of mean intercept error	0.60 ‰

Table 6: Setup and Output of the Monte Carlo simulation for the data of the lake Winnipeg wetlands.

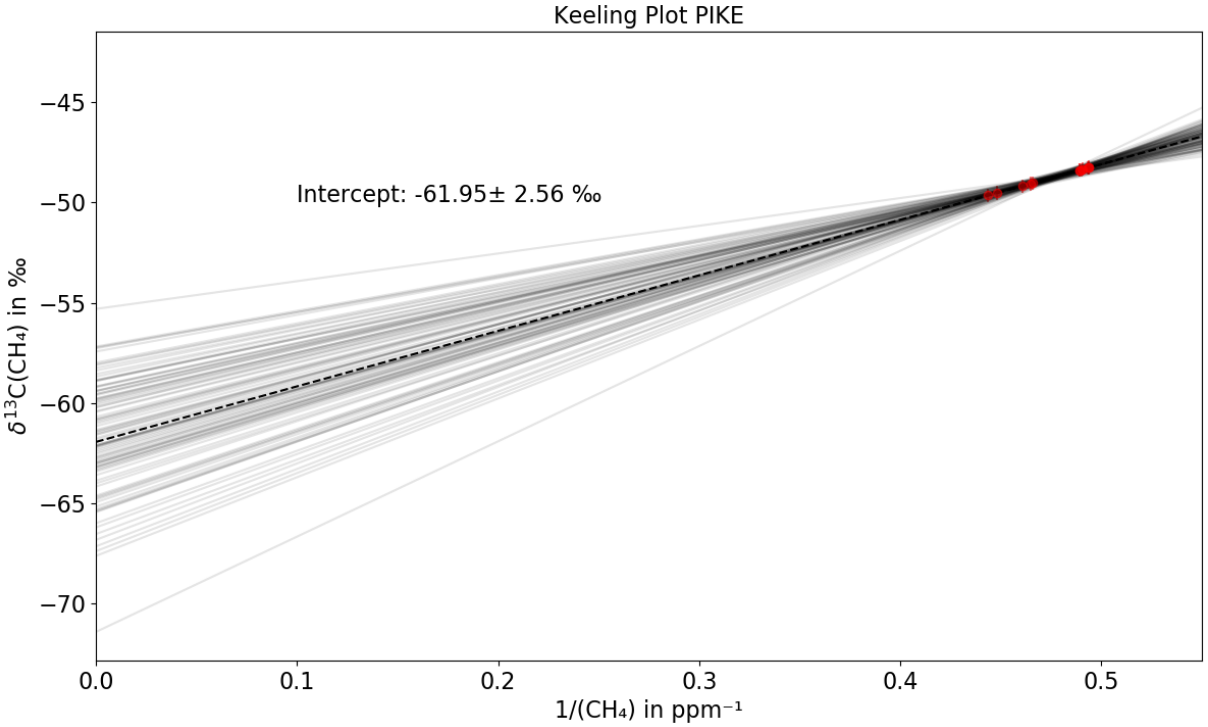

Figure 30: The Keeling plot for the measurements from RF PIKE is shown, as well as an ensemble of $N = 100$ linear regressions for variations of the input data, caused by measurement uncertainty. Red dots indicating the single tank measurements, with error bars indicating the range of uncertainty. The Taylor expanded error of the reciprocal methane concentrations is small, thus it is not visible in the graph. The best fit linear regression with the intercept is plotted as dashed line. The ensemble of regression lines is plotted in light gray, and only 100 out of 10000 are shown for a more accessible presentation. The range of the calculated best fit intercept (± 2.56 ‰) is this time given by the standard deviation of the ensemble intercepts.

Discussion and classification of the results in the context of literature

The analysis of the research flight "PIKE" propounded that methane source signatures, measured with the MIRACLE instrument, can be determined with a uncertainty of only a few ppt. In the following paragraph, the detected signature of -61.95 ‰ is discussed in the context of existing studies of the Lake Winnipeg area and ranked according to the methane sources discussed in Chapter 2.2.2. The list of $\delta^{13}C(CH_4)$ signatures, provided by Sherwood et al. 2017, give a first reference point to the classification of the detected signature. Because of the ^{13}C depleted isotopic composition, the indication, that the methane was emitted by a biogenic source, is strong. In the study, the mean methane carbon isotope signature was found to be -61.5 ‰ for wetlands, thus the calculated lake Winnipeg wetland signature of -61.95 ‰ agrees with Sherwood et al. 2017. Still, as the signatures of the individual sources have wide ranges, the methane could also be attributable to other methane sources, without knowing the category of emitters located in the Winnipeg area. Wahlen M. 1989 investigated tundra wetland $\delta^{13}C(CH_4)$ signatures to be -62.9 $\pm$ 1.9 ‰. The samples were taken approximately 500 km north of Thompson, thus not within the area probed by HALO. But since the analysis was also done for boreal wetland methane emissions, and the study site from "PIKE" extends 400 km in north south direction, the signatures of the two studies should not differ much. Within the errors of the analysis, the results are in agreement with each other. Bellisario (1996) studied boreal peatland methane fluxes from June to September 1994, in an area 30 km west of Thompson in Manitoba. Thus the study site overlaps with the region probed by MIRACLE aboard HALO on the research flight "PIKE". Part of the study at that time was also the examination of methane for carbon isotopes ^{12}C and ^{13}C. The sampling took place at four different locations within the area, each of them covering a different kind of wetland. i.e. bogs and fens with varying acidity. Samples were taken from soil pore water, which was equilibrated with pure nitrogen afterwards for analysis in the laboratory. The resulting isotope signatures were found to be -50.0 and - 56.0 as well as -61.9 ‰ for three bog areas, and -73.3 ‰ for a fen. Since the soil samples do not include a mixture of methane emitted by different sources, but only methane originating from the pathway specific for that location, data of a single soil sampling are difficult to compare with those of MIRACLE, collected in the mixed PBL. Assuming that the region sampled by HALO on a large scale (several thousand square kilometers) contains all the sources presented in Bellisario 1996, the averaged value of the individual source signatures offer an approach for a comparison with the MIRACLE measurement. The average value of the signatures described in Bellisario 1996, all equally weighted, amounts to -60.3 ‰. Thus, the signature agrees with the $\delta^{13}C(CH_4)$ measurement of MIRACLE (-61.95 ‰) when accounting for the uncertainty of the source signature determination of $\pm$ 2.56 ‰. Table 7 summarises the signatures for the lake Winnipeg wetland area determined in this work and from other studies.

The results of this work are in good agreement with the other studies. Thus existing research results for the lake Winnipeg wetland region could be confirmed with the innovative measurement technology of MIRACLE. Both Bellisario 1996 and Wahlen M. 1989 dates back more than 25 years, which means that the source signature determination of this work is not limited to the confirmation of them. Furthermore it was possible to show, that any possible climatic or vegetative changes of the last 25 years have not affected the isotopic composition of CH_4 emitted at the study site. This information is important for monitoring changes in biogenic

Comparison of the determined lake Winnipeg wetland δ^{13}C(CH_4 signature

Study	$\delta^{13}C(CH_4)$	$\Delta\delta^{13}C(CH_4)$
Wahlen M. 1989	-62.9 ‰	1.90 ‰
Bellisario 1996	-60.3 ‰ (averaged)	4.22 ‰
this work	-61.95 ‰	2.56 ‰

Table 7: Compilation of the signatures identified in this work and in other papers.

methane formation processes. In addition, the MIRACLE airborne measurements have the advantage of taking samples over an area of several tens of thousands of square kilometres. Thus, the obtained source signature is representative of a much larger area than measurements taken on the ground, which only make statements about smaller areas.

5.3 Study site 2: A forest fire plume

The second $\delta^{13}C(CH_4)$ signature analysis is done for a spatially sharply defined source of methane, a smoke plume of a forest fire. HALO completed the 15th research flight of CoMet 2.0 on 11.09.2022, the target was another sampling of the lake Winnipeg area, this time with a focus more on the southern part between lake Winnipeg and the neighboring lakes. After the first part of the flight, called "WOLVERINE", a tubular smoke plume was visible over the northern parts of lake Winnipeg, which can be seen in Figure 31. The satellite image shows that the plume has a main body, which appears opaque on the image, but it also has offshoots over the entire area.

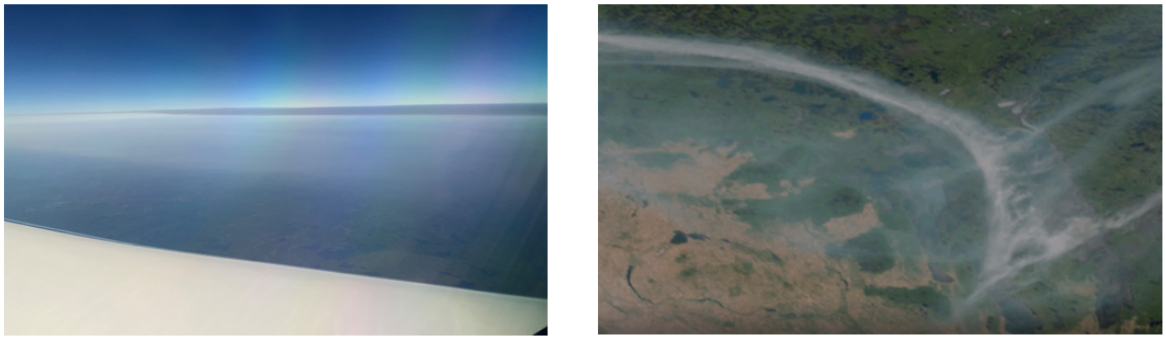

Figure 31: The left picture shows the fire plume, seen from HALO during the RF WOLVERINE. It can be seen, that the plume is vertically thin and appears as a dark layer on the horizon. The dark colour is caused by the high amount of aerosols, produced by the combustion. On the right side, the same plume was captured by a satellite image from NASA Worldview 2022, with lake Winnipeg directly below the frayed part of the plume. The plume comes from a fire near the Rocky Mountains and was transported southeastwards, while the form remained almost unchanged and the plume has not dissipated.

As wildfires are emitters of methane (see Chapter 2.1.2) and have a distinctive, ^{13}C rich $\delta^{13}C(CH_4)$ signature, the original flight over the wetlands could be extended to investigate the fire plume. After the first half of the remote sensing pattern, the plume was located underneath the plane and was then flown from top to bottom via a descending spiral. Almost three hours later, after completing the in situ pattern, the plume could be sampled a second time when HALO began to climb for the flight home. The flight pattern over the target area is depicted in Figure 32, where the carbon monoxide concentration measured by JIG is colour plotted over the path. CO was used to show the places of the plume crossing, as it is produced by the combustion of biomass and therefore a tracer for the fire plume. The first and the second crossings are marked in the figure and can be determined by their CO concentration of around 1000 ppb at the northern end of lake Winnipeg. Since there was a time difference of 3 h between the two crossings, the plume drifted eastwards with the wind between the two traverses. The smaller variations in CO, away from the plume, are probably also due to the emissions of the fire, which are smeared over the area and therefore diluted.
The left side of Figure 31 shows, that the plume has not sunk to the surface, but has a sharp lower and upper end in the troposphere. Thus, for the analysis of the biomass burning

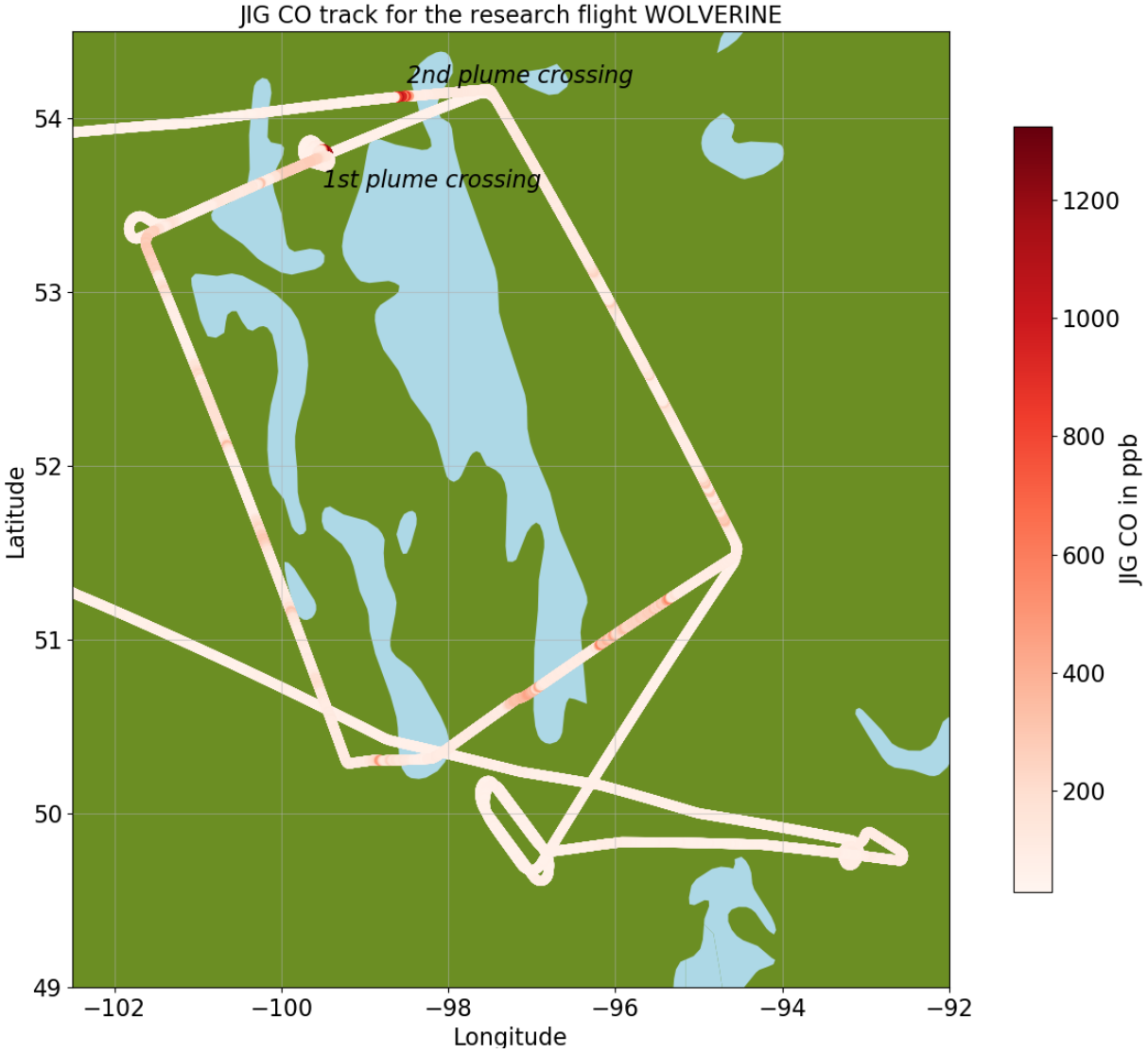

Figure 32: The target area of the research flight WOLVERINE is depicted. CO measured by JIG is colour coded in red over the flight track. The first and the second plume crossings can be identified by their enhanced CO concentration of around 1000 ppb. Variations in CO can also be seen in the rest of the region. Because of the second plume crossing took place 3 hours after the first one, the plume was shifted more to the east.

signature, it is important to know the spatial extent of the plume in order to know which tanks can be taken into account for the evaluation. To know the vertical dimension, the CO measured by JIG can act as a tracer. Vertical expansion is particularly important in order to know whether the plume is above or in the PBL, and thus if there is a mixture of methane from biomass burning and other sources, in this case emissions from wetlands. Figure 33 shows the vertical profile of the CO and methane measured by JIG for the time from 17:30 UTC to 19:00 UTC. The ascending spiral took place in the middle of that period.
By the profiles of CO and CH_4, the bottom of the plume can be located to be 3000 m above mean sea level, and the upper limit to approximately 4000 m, as CO shows high concentrations

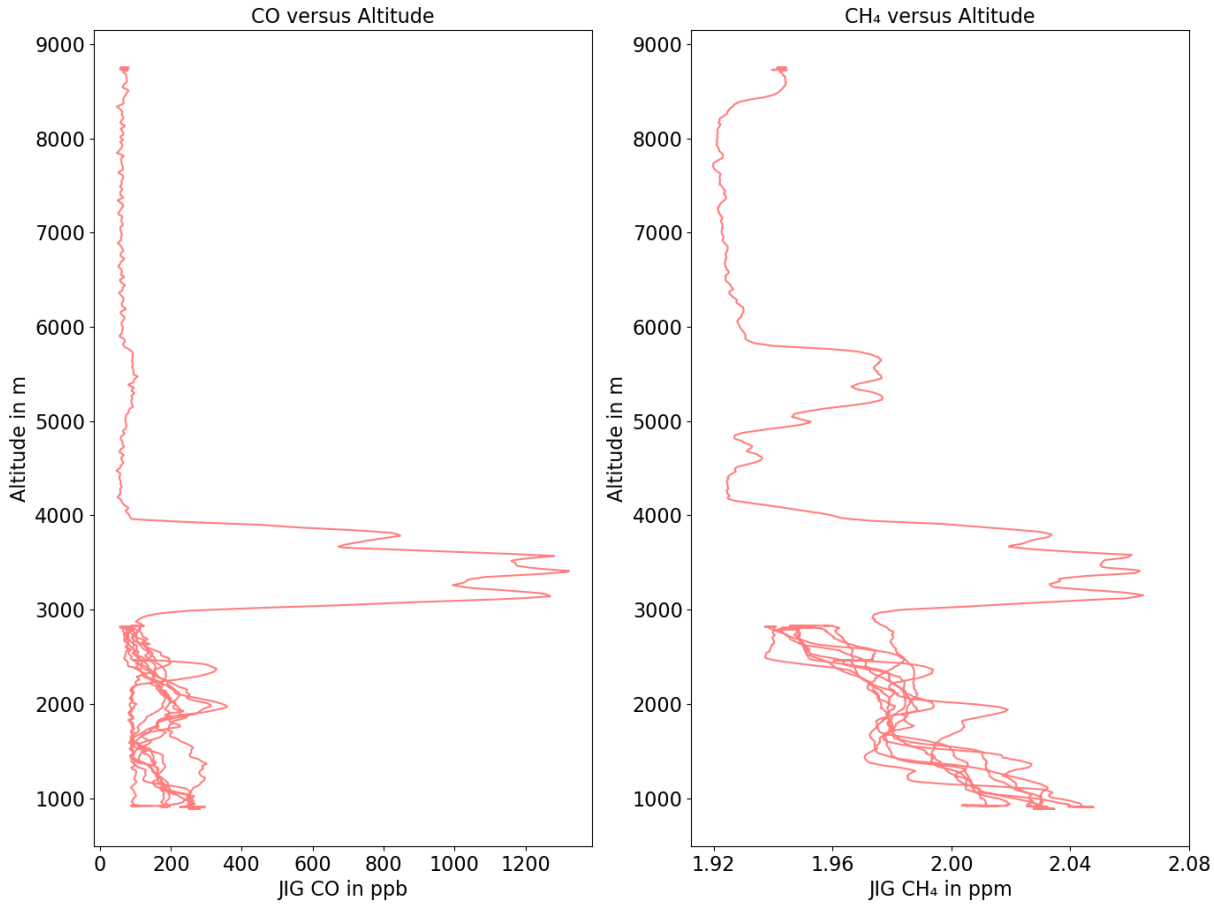

Figure 33: The measurements of CO and CH_4 from JIG are plotted as vertical profiles for time around the first plume crossing. The CO enhancements up to 1200 ppb allow the conclusion that the plume was located between 3000 and 4000 m above mean sea level. This is also consistent with methane measurement. CH_4 is also enhanced below the plume in the PBL, and above the plume, which could be due to long distance transport, i.e. from a different source.

of up to 1200 ppb in this regime and methane is also elevated up to 2.050 ppm. Both, CO and CH_4 are less above 4000 m and bellow 3000 m. Especially methane is increasing from a, vertically seen, local minimum directly below the plume towards the ground. The H_2O measurements and temperature profiles gave indication, that the PBL top was 1600 m at that time, thus the plume was above the planetary boundary layer and therefore not mixed with local wetland sources. Above the plume, between 5000 and 6000 m the measurements reveal an additional maximum of methane, which could for example be due to long distance transport, therefore the source is not known. Thus the vertical profiles constrain the tanks used for the analysis to samples taken between the top of the PBL and 5000 m altitude. For the signature calculation the tanks filled above 3000 m were used, since the PBL height was 1600 m above ground and the ground elevation is 200 - 300 m above mean sea level. Figure 34 displays the spots of sampling, colour coded with the corresponding isotopic signature. A heavier carbon isotope composition is measured in some of the tanks, taken during the plume crossings. The others are used as background samples.

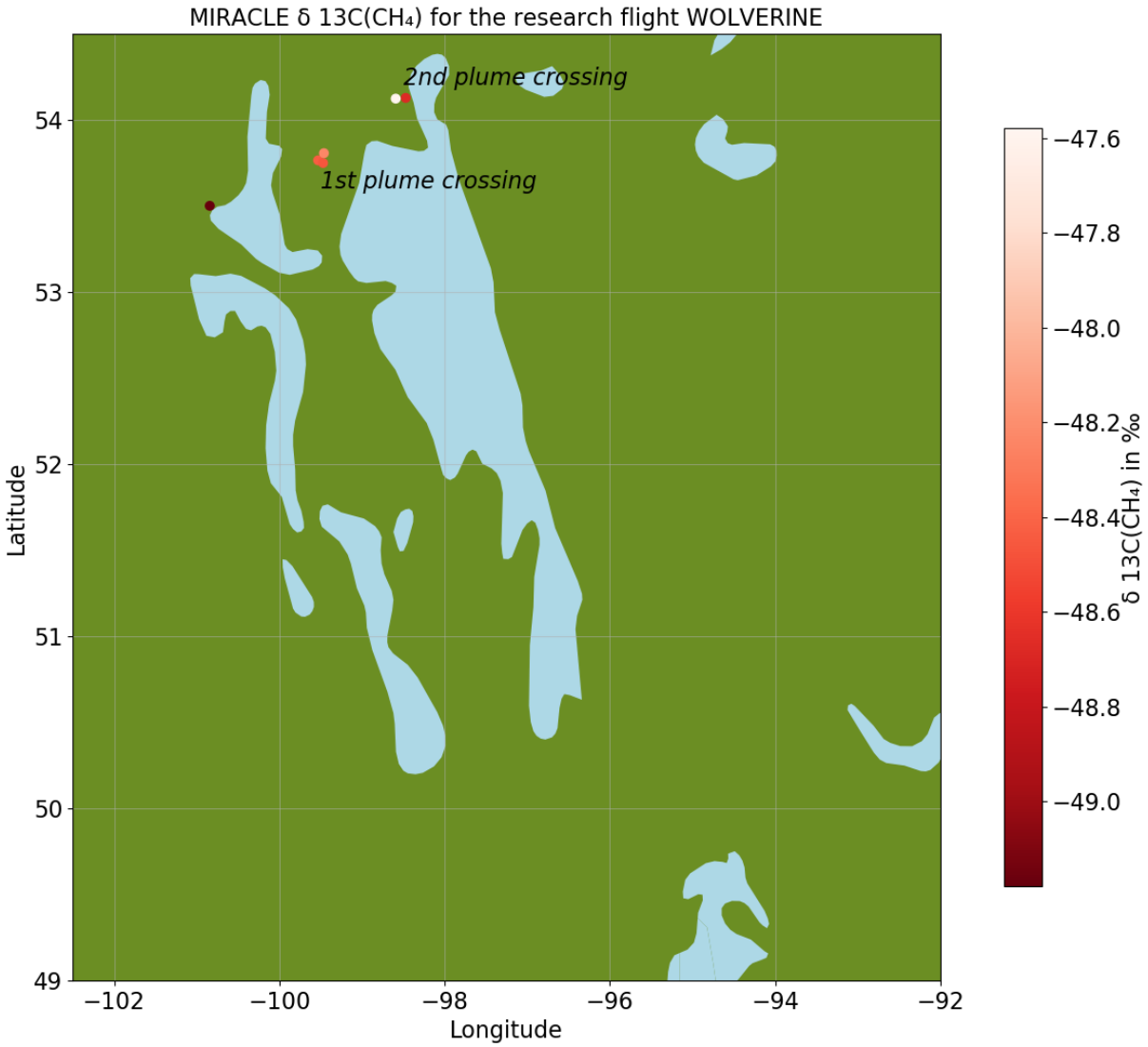

Figure 34: The spots where the tanks were filled, which are taken into account for the signature calculation of the fire plume, are shown. The $\delta^{13}C(CH_4)$ values of each tank are colour coded. ^{13}C rich signatures were measured for samples taken during the plume crossings.

Maximum and minimum CH_4 concentrations of the cylinders are 2.042 ppm and 1.928 ppm respectively, thus spanning a range of 114 ppb. The corresponding heaviest and lightest signatures are -47.58 and -49.18 ‰. Hence, the range of captured CH_4 concentrations as well as the range of $\delta^{13}C(CH_4)$ values is smaller than the ones measured during the RF PIKE over the Winnipeg wetlands. The samples taken are again consistent with the measurements of JIG, as the mean deviation between methane concentrations in the tanks and from JIG during the tank filling is -2.6 ppb. Thus, no bias towards enriched or depleted methane can be detected. The standard deviation of the difference in methane was found to be 13.9 ppb, which is due to the spatially constrained source, which involves large local concentration differences and therefore makes the comparison of the two instruments more difficult than for areal sources, with less strong gradients. The time series of methane measured by JIG is depicted in Figure 35, where

the red dots indicating the spots of sampling by MIRACLE. Furthermore the two black arrows denote the sharp methane peaks of the fire plume, which was passed through once at just before 18:00 UTC and once just before 21:00 UTC.

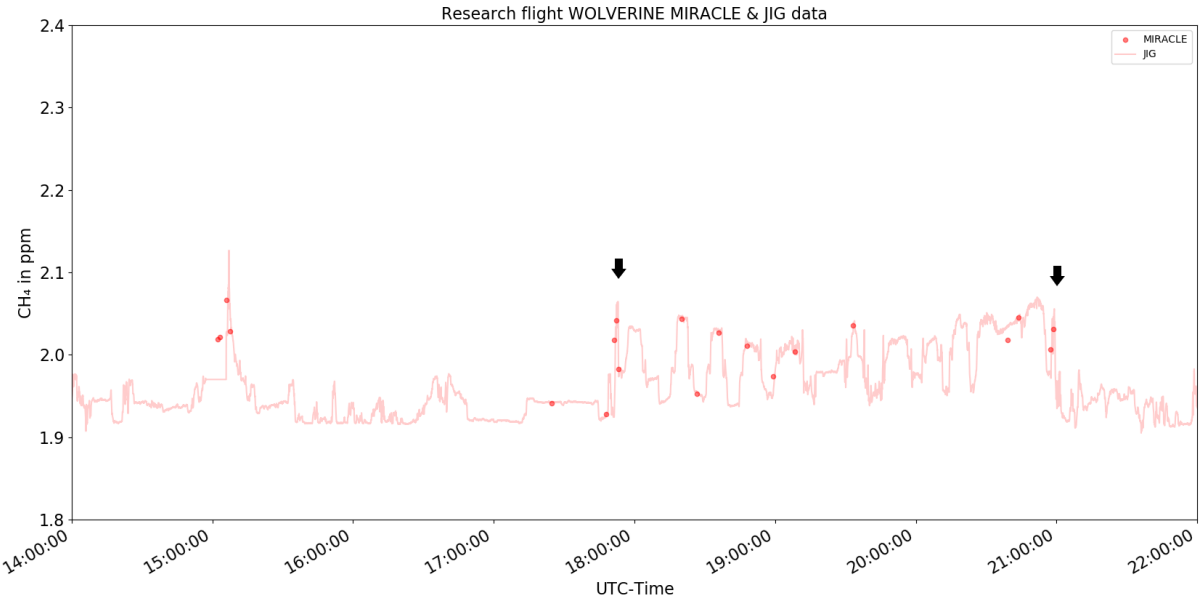

Figure 35: The time series of methane measured by JIG is shown in light red, whereas the samples taken by MIRACLE are plotted by bold red dots. The two arrows mark the two methane peaks just before 18:00 UTC and 21:00 UTC, which are due to the crossing of the fire plume.

The Keeling Plot, which contains the measurements of the samples taken above 3000 m within and around the fire plume, is shown in Figure 36.
Intercept and the uncertainty of the intercept are found to be -35.33 $\pm$ 8.58 ‰. The large uncertainty interval is either due to the fact that the resolution of the instrument is too low, i.e. the measured delta values are shifted against each other, which makes the Keeling Plot less accurate, or there is a mixing of different source signatures. A combination of both sources of error is also possible. The imprecise source signature determination is also reflected by the low coefficient of determination ($R^2 = 0.368$). In order to investigate whether the total measurement uncertainty is responsible for the uncertainty of 8.58 ‰, or if it's due to methane mixtures from different sources, a Monte Carlo simulation was done with an ensemble of size N = 10000. The linear regressions were calculated for the fitted values, varied by the total uncertainties of 0.64 ppb for methane and 0.34 ‰ for $\delta^{13}C(CH_4)$, as explained in the evaluation of the RF PIKE (see Section 5.2). In Figure 37 100 runs of the ensemble of linear regressions is plotted, in addition, Table 8 gives an overview of the input variables of the Monte Carlo simulation and the corresponding results.
Since the fitted values are used for the simulation, a perfect correlation between the data points (they are located on the best fit dashed line) is assumed, what means that this scenario doesn't contain mixing of sources. When running the simulation, the averaged error of all the ensemble intercepts should be equal to the error of the best fit Keeling plot ($\pm$ 8.58 ‰), to be able to say that the uncertainty of the calculated source signature is due to insufficient

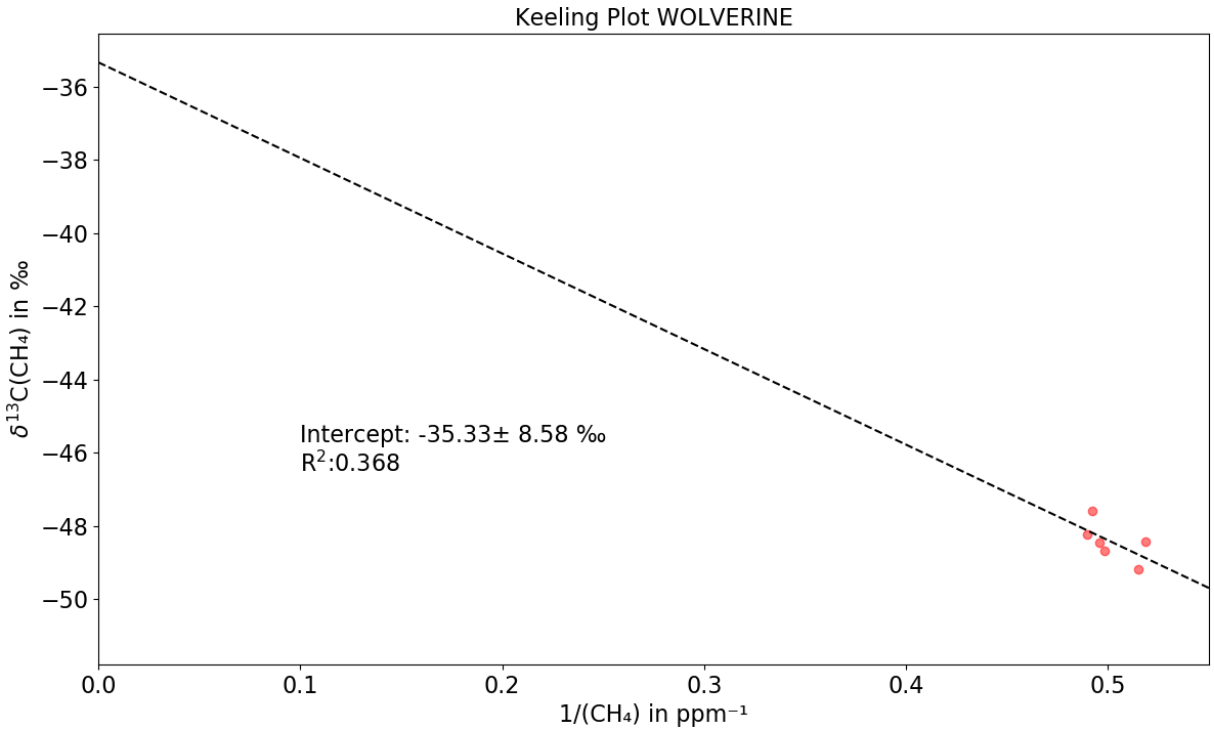

Figure 36: The Keeling plot for the fire plume, sampled during the RF WOLVERINE is plotted. The resulting intercept of -35.33 ‰ is fraught with a relatively large error of ± 8.58 ‰.

measurement resolution. Figure 37 shows, that the ensemble mean intercept error is only 5.92 ‰ with a standard deviation of 2.26 ‰. Thus the best fit intercept error of ± 8.58 ‰ is within 1.18 standard deviations of the ensemble intercept errors, which means that the probability that the best fit error is fully due to measurement inaccuracy is 12 %. Since the mean error of the ensemble is smaller than the best fit error, there is no indication for correlated measurement uncertainty, as it was the case for the evaluation of the RF "PIKE". Thus, the drift of the instrument is superimposed by other and larger sources of uncertainty, compared to "PIKE". When accounting for the 12 % probability, that the best fit error is only due to measurement uncertainty, there remains a not insignificant probability that the error has further contributions. A possible explanation is, that the assumption that there was no mixing of different methane sources was wrong. If the samples contained different amounts of methane from different sources, the correlation between the tanks will be less, which is reflected in a greater uncertainty of the intercept. Another possible explanation derives from the sampling itself. The purge time of 20 s is optimized for flows that the metal bellows pump is capable of delivering within the PBL. It may that at the fire plume sampling height, the reduced flow did not allow for a complete exchange of the gases in the tanks, even though the tanks were flushed for 40 s. A residual stock of old gas would have remained in the tanks and falsified the samples, if the flow was to low.

Monte Carlo simulation for WOLVERINE	
Input:	
Ensemble size	N = 10000
Best fit intercept	-35.33 ‰
Best fit intercept error	-8.58 ‰
Input parameters	data projected on best fit
Variations	$u_{tot}(1/CH_4)$, $u_{tot}(\delta^{13}C(CH_4))$
Output:	
Spread of ensemble intercepts	6.38 ‰
Mean of intercept error	5.92 ‰
Standard deviation of mean intercept error	2.26 ‰

Table 8: Setup and Output of the Monte Carlo simulation for the data of the fire plume.

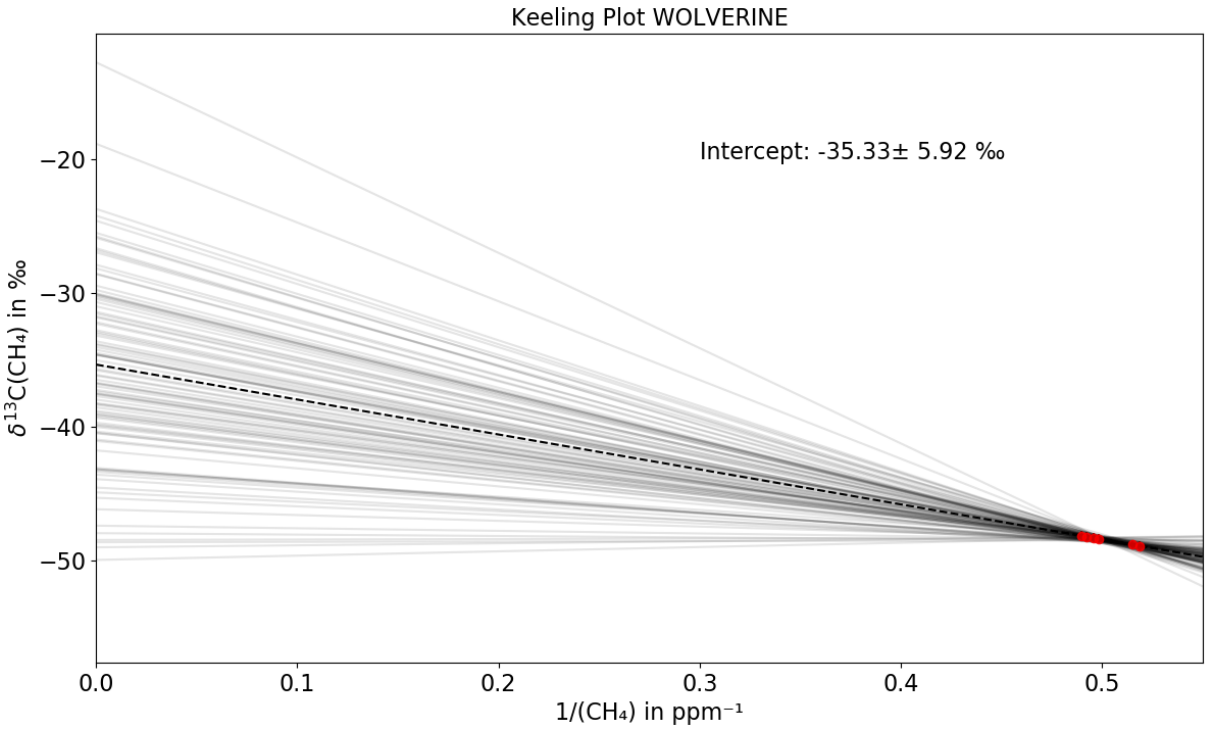

Figure 37: The best fit linear regression is shown with the corresponding intercept of -35.33 ‰. 100 out of the 10000 performed linear regressions are plotted. The regressions were calculated for variations of the fitted data by the total measurement uncertainty. The error of the intercept ($\pm$ 5.92 ‰) is computed from the mean of the individual intercept errors of the Monte Carlo ensemble.

Discussion and classification of the results in the context of literature

The classification of the determined source signature on the basis of literature again results in a correspondence with the biomass burning signatures compiled in Sherwood et al. (2017). The mean C3 biomass burning signature is given with -26.7 ‰ (see Table 2), which is more

enriched by the heavier isotope than the fire plume isotope ratio from the RF "WOLVERINE". Nevertheless, there is a long tail in the distribution that extends to -40 ‰ in Figure 3 and thus also covers the biomass burning signature determined here. There is even more overlap, when accounting for the large uncertainty interval of the fire plume signature, which is $\pm$ 8.58 ‰. Fisher et al. 2011 found $\delta^{13}C(CH_4)$ signatures of -28.7 $\pm$ 0.7 ‰ for a mature pine forest fire in the Northwest Territories, Canada. This value is limited in its comparability to the signature determined in this work, since the burning biomass was also a boreal forest, but located near Jasper in the Rockie Mountains and thus possibly influenced by other vegetation. A second $\delta^{13}C(CH_4)$ signature for a forest fire located in Ontario, Canada, was found to be -27.8 $\pm$0.3 ‰ (Fisher et al., 2011). Therefore, although the magnitude of the signature agrees with other biomass burning events, the more detailed comparison reveals discrepancies with measurements from similar sources. Table 9 summarises the signatures from the literature and this work.

Comparison of the determined forest fire $\delta^{13}C(CH_4)$ signatures

Study	$\delta^{13}C(CH_4)$	$\Delta\delta^{13}C(CH_4)$
Fisher et al. 2011	-27.8 ‰	0.3 ‰
Fisher et al. 2011	-28.7 ‰	0.7 ‰
this work	-35.33 ‰	8.58 ‰

Table 9: Compilation of the signatures identified in this work and in Fisher et al. 2011.

6 Discussion and comparison of the measurement technology and $\delta^{13}C(CH_4)$ analysis of MIRACLE

6.1 Comparison of MIRACLE and other airborne measurements of $\delta^{13}C(CH_4)$

The MIRACLE instrument offers several advantages compared to conventional methods of determining the isotope ratio. In Lowe and Bergamaschi 2002 a list of established techniques for measurements of isotopes of atmospheric methane is given.

6.1.1 Comparison with IRMS and airborne sampling

The standard method of analysis is the isotope ratio mass spectrometry (IRMS), which requires large sample gas volumes of 20-500 litres and the methane has to be converted to CO_2 for the analysis. The latter is a complex process, including the removal of water, N_2O, CO_2, CO and non-methane hydrocarbons, the sequential cyrogenic trapping of the gas and the combustion of the remaining methane (Lowe and Bergamaschi, 2002). Thus, this technique is suitable for laboratory applications, but hardly offers the possibility to carry out airborne in situ measurements The MIRACLE instrument does not require large volumes of gas, nor do samples need to be prepared prior to analysis. Large gas volumes sampled aboard the aircraft would lead to greater spatial blur, as a sample would be taken over longer periods of time and thus longer flight distances. The sampler unit of MIRACLE collects the gas within 2400 m travelled distance, thus allows for spatially high resolved scanning. Preparation of the samples would mean an increased time effort and thus a lower number of samples per flight. The MIRACLE instrument analyses a new sample every 10 minutes and could have an even higher throughput if the measurement time is shortened. This, in turn, would lead to lower precision of the instrument. The precision of conventional IRMS is approximately 0.05 ‰, which is more precise compared to the laser spectrometer used in MIRACLE by almost a factor of 10. A precision of 0.1 ‰ is possible with the technique of CRDS, but requires an extended averaging of 1 hour (Rella et al., 2015). Thus, only a few samples could be analysed within the duration of a single research flight. The MIRACLE measurement time selection has been optimized to measure as many samples as possible (up to 30 per flight) with sufficient precision, but can be adjusted as required.

IRMS analysis of atmospheric $\delta^{13}C(CH_4)$ is possible, when air sampling is decoupled from the subsequent analysis in the laboratory.
This was done for example by Lampert et al. 2020 with a quadrocopter, which collected air samples at altitudes up to 1 km. The study site was 4.2 km^2 in size and each flight was performed within 10-11 min. 12 samples per flight were collected. The measurement uncertainty of the isotopic analysis in the laboratory was 0.5 ‰, hence in the same order of magnitude as the one of MIRACLE. The quadrocopter can be used to study small-scale areas, but it would not be possible to study large-scale sources, e.g. to probe the lake Winnipeg wetlands as it was done with the MIRACLE instrument. Furthermore, due to the small range of the quadrocopter, areas that are poorly developed in terms of infrastructure, e.g. remote study sites in high northern latitudes, can only be sampled with great effort. Since the maximum

flight altitude of the quadcopter is limited to 1 km, it would not be possible to investigate methane emissions at higher altitudes, such as the fire plume that was sampled by MIRACLE in the RF "WOLVERINE". Thus, with HALO as a platform for $\delta^{13}C(CH_4)$ analysis, there are various advantages compared to the quadrocopter.
France et al. 2022 determined methane carbon isotopic signatures of tropical wetlands, rice fields and wild fires. They used either the twin-otter research aircraft or the BAE 146-FAAM (Facility for Airborne Atmospheric Measurement) aircraft and collected samples via tedlar bags respectively stainless steel tanks for subsequent laboratory analysis. The sampling strategy was to collect 12-19 samples for each areal wetland study site, thus approximately as many as for MIRACLE. Accounting for the maximum ranges of both of the airplanes (approx. 1500 km for the twin otter, <3000 km for the BAE 146-FAAM), they are suitable for areal sources, but could not sample as many and distant target areas as was done with HALO during the CoMet 2.0 campaign (see Chapter 3). Moreover, the in situ measurement method of MIRACLE offers the possibility to evaluate the $\delta^{13}C(CH_4)$ data directly after a research flight and thus immediately adapt the flight and sampling strategy within the course of the campaign.
Gałkowski et al. 2021 presented the isotopic signature for the Upper Silesian Coal Basin determined by the analysis of airborne flask samples, with $\delta^{13}C(CH_4)$ of -50.9 $\pm$ 1.1 ‰. The JAS (Jena Air Sampler) flask sampler was part of the instrumentation of CoMet 1.0 and CoMet 2.0. It has a capacity of 12 glass bottles per flight, which are analysed in the laboratory by IRMS. The JAS sampler aboard HALO has the advantage of more precise (<0.05 ‰) $\delta^{13}C(CH_4)$ analysis compared to MIRACLE (0.34 ‰), but is limited to 12 samples per flight (up to 30 for MIRACLE) and delayed analysis afterwards. Since both instruments were part of the CoMet 2.0 campaign, a measurement comparison in the course of the data analysis is possible. This allows the measurement method of MIRACLE to be directly compared with the analysis by IRMS and offers an additional quality check for the data.

6.1.2 Comparison with airborne $\delta^{13}C(CH_4)$ in situ measurements

The direct airborne in situ measurement of $\delta^{13}C(CH_4)$ was done over the north slope of Alaska (Healy, 2016). Since the IRMS technique is not suitable to be used airborne, a quantum cascade laser (QCL) was deployed aboard a research aircraft in combination with an additional cavity, to allow for enhanced absorption. In this method, the magnitude of infrared absorption by methane molecules is measured by laser spectroscopy. The instrument was supplied directly with ambient air, without previous sampling. Although a continuous and high spatial resolution over the target area could be achieved, the analysis was limited due to the lower precision of the instrument. The data were averaged over intervals of 20 s, with a resulting instrument precision of 4.87 ‰. The instrument precision is significantly worse compared to IRMS (0.05 ‰) and MIRACLE (0.34 ‰for 10 min averaging) and approximately of the same size as the MIRACLE uncertainty for the non-averaged data (3.7 ‰).
Vertical profiles of $\delta^{13}C(CH_4)$ values were determined over the north slope of Alaska, with CH_4 concentrations more depleted in ^{13}C found near the surface (-68 ‰) and CH_4 consisting of more ^{13}C for the free troposphere (-45 ‰ above approx. 250 m above mean sea level). The $2\,\sigma$ uncertainty intervals were approximately $\pm$ 25 ‰ for the near surface $\delta^{13}C(CH_4)$ signature, respectively $\pm$ 10 ‰ for the free troposphere signature. In the context of these uncertainties, it is not possible to make a clear distinction between sources, especially not if the aim is to investigate a more precise gradation within a given source, e.g. dependencies on vegetation,

latitude, etc. for wetlands. The source signature analysis of the RF "PIKE" demonstrated, that the MIRACLE instrument is suitable for clearly defined $\delta^{13}C(CH_4)$ determination, in this case the assignment of the signature to boreal wetlands in central North America. The instrument of Healy 2016 is capable to observe large gradients in $\delta^{13}C(CH_4)$ and distinguish between sources with a low and a high ^{13}C content, i.e. between microbial and biomass burning, due to the limited precision. As noted above, the MIRACLE analyser has a comparably low precision in the raw data, but improved by the additional sampler unit, enables accurate source signature determinations.
In addition to the discontinuity of the measurement, a disadvantage of MIRACLE is also the dependence of the targeted sampling on further in situ methane measurement, since the ambient concentrations are not monitored during the analysis of tanks (see Section 5.1). During the CoMet 2.0 campaign, sampling was therefore carried out on the basis of JIG measurements - a similar instrument with fast response time would also be useful for coordinating the sampling in the context of future deployments of MIRACLE.

6.2 Discussion of the source signature uncertainty analysis

In Section 5.2 it was shown, that the MIRACLE instrument aboard HALO was capable to determine the $\delta^{13}C(CH_4)$ signature for an areal methane source, the lake Winnipeg wetland area with -61.95 ‰. This result was consistent with other studies, e.g. Bellisario 1996. In order to make a statement about the quality of the signature determined by MIRACLE, the collection isotopic signatures from Sherwood et al. 2017 is used. This data set contains 39 studies investigating the signatures of wetlands. The 1σ standard deviation of the signature determination, averaged over all 39 studies, is 2.7 ‰. The 1σ uncertainty interval resulting from the lake Winnipeg signature measurement of MIRACLE is 2.56 ‰and thus in the same order of magnitude as the average uncertainties of the other studies. This underlines the suitability of the instrument for investigating the $\delta^{13}C(CH_4)$ signatures of areal methane sources. Since the majority of the 39 signatures were determined by mass spectrometry and from samples, collected on the ground, neither the use of laser spectrometry, nor the implementation of the instrument on the aircraft does restrict the accuracy of the methane carbon isotope measurement.

The second evaluation of data was done for a spatially confined biomass burning methane source. The analysis yielded a $\delta^{13}C(CH_4)$ signature of -35.33 ± 8.58‰, hence more uncertain, than the signature of the lake Winnipeg wetlands. Reasons for these discrepancies are on the one hand the smaller methane enhancements of the "WOLVERINE" fire plume compared to the background concentration. On the other hand, the Monte Carlo simulation pointed out, that the uncertainty probably cannot be explained by the measurement inaccuracy alone, but that there might have been influences from different methane sources. This could be due to the sampling process itself. Nevertheless the tanks were flushed for 40 s, since the plume was located above the PBL in 3000-4000 m altitude, a contamination of the samples by residual gas of prior tank fillings, with consequent falsification of the samples, cannot be excluded. A possible improvement for further deployments of the MIRACLE instrument would be a flow controlled flushing time. This would ensure that each tank is filled only after a certain flushing volume has been passed through beforehand, thus reducing possible contamination.

Another possible explanation is, that there may have been a mixing of different methane sources in the samples. The samples would therefore have to be checked more closely for their purity, for example by investigating the history of the air parcels, which were probed. Back trajectory analysis for the air masses collected within the individual tanks would give indication whether the methane could originate from different sources. Especially for the sampled region of the free troposphere, where influences from long range transport, as well as from the PBL, by e.g. convective events as thunderstorms, cannot be ruled out, trajectory calculation could be an important criterion for the purity of the samples. Therefore, this method should be used for the analysis of all flights of the CoMet 2. 0 campaign.

7 Conclusion

A innovative setup for airborne in situ measurements of methane carbon isotope ratios was developed and for the first time deployed during the CoMet 2.0 campaign aboard the research aircraft HALO. The aim of this work was to investigate, to what extent it is possible to determine methane source signatures with this system. This included the description of the functionality and structure of the instrument, the determination of the precision, the overall measurement uncertainty and the reliability of MIRACLE in terms of contamination of the gas by the sampler unit. The main achievements of the instrument characterisation are:

- A Picarro G2210-i GHG analyser was supplemented by a sampler unit. CH_4, CO_2, C_2H_6 and $\delta^{13}C(CH_4)$ can be measured directly from ambient air or from previous storage in the sampler unit.
- 6 stainless steel tanks are used for the intermediate storage of gas to allow for extended measurement time, including long time averages for improved precision of the analysis.
- GHG concentrations and $\delta^{13}C(CH_4)$ remain stable during the storage in the tanks
- The total measurement uncertainties for CH_4 and $\delta^{13}C(CH_4)$ were determined to be 0.64 ppb respectively 0.34 ‰.
- Both measurement modes, directly from ambient and tank analysis, are consistent with the measurements from the well established airborne GHG analyser JIG.

Furthermore, the aim was to analyse the results of the measurement of the isotope ratio on the basis of selected research flights of the CoMet 2.0 Arctic campaign, to carry out the corresponding error estimation and to discuss the results in the context of literature. The main findings of the $\delta^{13}C(CH_4)$ analysis are as follows:

- The MIRACLE instrument is suitable for determining the $\delta^{13}C(CH_4)$ of areal and small-scale methane sources
- The $\delta^{13}C(CH_4)$ signature of the lake Winnipeg wetland area was investigated and amounts to -61.95 $\pm$ 2.56 ‰. A Monte Carlo simulation revealed, that the uncertainty is likely caused by measurement uncertainties, again demonstrating that the sampling has not affected the isotopic ratio. The result is consistent with several already existing measurements in the area and thus implies, that the underlying methane formation processes are constant over time. Due to the airborne implementation of the measurement, the result is representative for a much larger area than the results of previous studies, and thus more relevant for calculating the global methane budget.
- The $\delta^{13}C(CH_4)$ analysis of the plume from a boreal forest fire resulted in a signature of -35.33 $\pm$ 8.58‰. The result is consistent with literature in the context of the measurement uncertainty, but has a very ^{13}C poor signature for methane emitted by biomass combustion. The Monte Carlo simulation for identifying the cause of the uncertainty of the result, showed, that there was likely a mixing of different methane sources, which demonstrates the urgency to examine the purity of the individual samples.

The measurement methodology and the obtained results were compared with other, airborne investigations of $\delta^{13}C(CH_4)$. The following differences and similarities emerged:

- The MIRACLE instrument combines the advantages of airborne sampling followed by laboratory analysis with the direct in situ measurement of the signature, as the sampler unit allows high precision of the analysis, the immediate availability of the results and a large number of samples, due to the reuse of the tanks after the in flight measurement.
- The uncertainty of the $\delta^{13}C(CH_4)$ signature of lake Winnipeg is of same size compared to other wetland methane carbon isotope ratio measurements by IRMS. Hence, the airborne implementation of the instrument does not reduce the accuracy of the source signature determination.
- The uncertainty of the fire plume signature was probably due to the mixing of different methane sources. This underlines the need for detailed testing of samples for their purity. On the one hand, the sampling itself can be improved by a flow-controlled flushing time. On the other hand, the data analysis has to include additional information about the circumstances during the sampling, e.g. PBL height, contained co tracers like CO or trajectory analysis to investigate the influence of different methane sources.
- Additional in situ methane instruments, like JIG, offer great advantages for the sampling with MIRACLE and the data analysis.

In summary, MIRACLE is an innovative instrument, which performs $\delta^{13}C(CH_4)$ measurements, with an accuracy of the results comparable to other existing methane signature analyses and in combination with the benefits of the airborne implementation. Hence, the data set obtained in the course of the CoMet 2.0 Arctic campaign can contribute to the determination of methane source signatures and thus also to the determination of the global methane budget.

References

Amediek, A., Ehret, G., Fix, A., Wirth, M., Büdenbender, C., Quatrevalet, M., Kiemle, C. and Gerbig, C. (2017). Charm-f-a new airborne integrated-path differential-absorption lidar for carbon dioxide and methane observations: measurement performance and quantification of strong point source emissions, *Applied optics* **56**(18): 5182–5197.

American rubber Corp (n.d.). Chemical compatibility.
URL: *https://www.americanrubbercorp.com/chemical-compatibility/*

Andrews, A. E., Kofler, J. D., Trudeau, M. E., Williams, J. C., Neff, D. H., Masarie, K. A., Chao, D. Y., Kitzis, D. R., Novelli, P. C., Zhao, C. L., Dlugokencky, E. J., Lang, P. M., Crotwell, M. J., Fischer, M. L., Parker, M. J., Lee, J. T., Baumann, D. D., Desai, A. R., Stanier, C. O., de Wekker, S. F. J., Wolfe, D. E., Munger, J. W. and Tans, P. P. (2014). Co₂, co, and ch₄ measurements from tall towers in the noaa earth system research laboratory's global greenhouse gas reference network: instrumentation, uncertainty analysis, and recommendations for future high-accuracy greenhouse gas monitoring efforts, *Atmospheric Measurement Techniques* **7**(2): 647–687.

Archer, D., Eby, M., Brovkin, V., Ridgwell, A., Cao, L., Mikolajewicz, U., Caldeira, K., Matsumoto, K., Munhoven, G., Montenegro, A. and Tokos, K. (2009). Atmospheric lifetime of fossil fuel carbon dioxide, *Annual Review of Earth and Planetary Sciences* **37**(1): 117–134.

Basu, S., Lan, X., Dlugokencky, E., Michel, S., Schwietzke, S., Miller, J. B., Bruhwiler, L., Oh, Y., Tans, P. P., Apadula, F., Gatti, L. V., Jordan, A., Necki, J., Sasakawa, M., Morimoto, S., Di Iorio, T., Lee, H., Arduini, J. and Manca, G. (2022). *Estimating Emissions of Methane Consistent with Atmospheric Measurements of Methane and d¹³C of Methane*.

Bellisario, L. (1996). *Net ecosystem exchange and methane emissions from a boreal peatland, Thompson, Manitoba*, PhD thesis, McGill University.
URL: *https://escholarship.mcgill.ca/concern/theses/m039k7180*

Berden, G., Peeters, R. and Meijer, G. (2000). Cavity ring-down spectroscopy: Experimental schemes and applications, *Int. reviews in physical chemistry* .

Byrom, R. E. and Shine, K. P. (2022). Methane's solar radiative forcing, *Geophysical Research Letters* **49**(15).

Craig, H., Chou, C. C., Welhan, J. A., Stevens, C. M. and Engelkemeir, A. (1988). The isotopic composition of methane in polar ice cores.

Demtröder, W. (2010). *Experimentalphysik 3*, Springer Berlin Heidelberg, Berlin, Heidelberg.

Dlugokencky, E. J. (2003). Atmospheric methane levels off: Temporary pause or a new steady-state?, *Geophysical Research Letters* **30**(19).

E. G. Nisbet, M. R. Manning, E. J. Dlugokencky, R. E. Fisher, D. Lowry, S. E. Michel, C. Lund Myhre, S. M. Platt, G. Allen, P. Bousquet, R. Brownlow, M. Cain, J. L. France, O. Hermansen, R. Hossaini, A. E. Jones, I. Levin, A. C. Manning, G. Myhre, J. A. Pyle, B. H. Vaughn, N. J. Warwick and J. W. C. White (2019). *Research article*.

Etheridge, D. M., Steele, L. P., Francey, R. J. and Langenfelds, R. L. (1998). Atmospheric methane between 1000 a.d. and present: Evidence of anthropogenic emissions and climatic variability, *Journal of Geophysical Research: Atmospheres* **103**(D13): 15979–15993.

Fisher, R. E., Sriskantharajah, S., Lowry, D., Lanoisellé, M., Fowler, C. M. R., James, R. H., Hermansen, O., Lund Myhre, C., Stohl, A., Greinert, J., Nisbet-Jones, P. B. R., Mienert, J. and Nisbet, E. G. (2011). Arctic methane sources: Isotopic evidence for atmospheric inputs, *Geophysical Research Letters* **38**(21): n/a–n/a.

Formolo, M. (2010). The microbial production of methane and other volatile hydrocarbons, *in* K. N. Timmis (ed.), *Handbook of Hydrocarbon and Lipid Microbiology*, Springer Berlin Heidelberg, Berlin, Heidelberg, pp. 113–126.

France, J. L., Fisher, R. E., Lowry, D., Allen, G., Andrade, M. F., Bauguitte, S. J.-B., Bower, K., Broderick, T. J., Daly, M. C., Forster, G., Gondwe, M., Helfter, C., Hoyt, A. M., Jones, A. E., Lanoisellé, M., Moreno, I., Nisbet-Jones, P. B. R., Oram, D., Pasternak, D., Pitt, J. R., Skiba, U., Stephens, M., Wilde, S. E. and Nisbet, E. G. (2022). d13c methane source signatures from tropical wetland and rice field emissions, *Philosophical transactions. Series A, Mathematical, physical, and engineering sciences* **380**(2215): 20200449.

Gałkowski, M., Jordan, A., Rothe, M., Marshall, J., Koch, F.-T., Chen, J., Agusti-Panareda, A., Fix, A. and Gerbig, C. (2021). In situ observations of greenhouse gases over europe during the comet 1.0 campaign aboard the halo aircraft, *Atmospheric Measurement Techniques* **14**(2): 1525–1544.

Ganesan, A. L., Stell, A. C., Gedney, N., Comyn-Platt, E., Hayman, G., Rigby, M., Poulter, B. and Hornibrook, E. R. C. (2018). Spatially resolved isotopic source signatures of wetland methane emissions, *Geophysical Research Letters* **45**(8): 3737–3745.

Gedney, N., Huntingford, C., Comyn-Platt, E. and Wiltshire, A. (2019). Significant feedbacks of wetland methane release on climate change and the causes of their uncertainty, *Environmental Research Letters* **14**(8): 084027.

Ghosh, A., Patra, P. K., Ishijima, K., Umezawa, T., Ito, A., Etheridge, D. M., Sugawara, S., Kawamura, K., Miller, J. B., Dlugokencky, E. J., Krummel, P. B., Fraser, P. J., Steele, L. P., Langenfelds, R. L., Trudinger, C. M., White, J. W. C., Vaughn, B., Saeki, T., Aoki, S. and Nakazawa, T. (2015). Variations in global methane sources and sinks during 1910–2010, *Atmospheric Chemistry and Physics* **15**(5): 2595–2612.

Gordon E.I. (2022). Hitran online.
URL: *https://hitran.org/lbl/2?6=on*

Healy, C. H. (2016). *Mapping and Characterizing the Alaskan North Slope Methane Flux With Airborne EddyCovariance Flux Measurements*, PhD thesis, Harvard University.
URL: *http://nrs.harvard.edu/urn-3:HUL.InstRepos:33840711*

IPCC AR6 Working Group I (2021). Climate change 2021: The physical science basis.

Klausner, T. (2020). *Aircraft-based in situ measurements of CH4 and CO2 downstream of European and Asian urban centres at local to synoptic scales*, Dissertation.

Lampert, A., Pätzold, F., Asmussen, M. O., Lobitz, L., Krüger, T., Rausch, T., Sachs, T., Wille, C., Sotomayor Zakharov, D., Gaus, D., Bansmer, S. and Damm, E. (2020). Studying boundary layer methane isotopy and vertical mixing processes at a rewetted peatland site using an unmanned aircraft system, *Atmospheric Measurement Techniques* **13**(4): 1937–1952.

Lan, X., Basu, S., Schwietzke, S., Bruhwiler, L. M. P., Dlugokencky, E. J., Michel, S. E., Sherwood, O. A., Tans, P. P., Thoning, K., Etiope, G., Zhuang, Q., Liu, L., Oh, Y., Miller, J. B., Pétron, G., Vaughn, B. H. and Crippa, M. (2021). Improved constraints on global methane emissions and sinks using d13c-ch4, *Global biogeochemical cycles* **35**(6): e2021GB007000.

Lan, X., K.W. Thoning, and E.J. Dlugokencky (2022). Trends in globally-averaged ch4, n2o, and sf6 determined from noaa global monitoring laboratory measurements.
URL: *https://doi.org/10.15138/P8XG-AA10*

Landau, D. and Binder, K. (2021). *A Guide to Monte Carlo Simulations in Statistical Physics*, Cambridge University Press.

Li, M., Karu, E., Brenninkmeijer, C., Fischer, H., Lelieveld, J. and Williams, J. (2018). Tropospheric oh and stratospheric oh and cl concentrations determined from ch4, ch3cl, and sf6 measurements, *npj Climate and Atmospheric Science* **1**(1).

Lowe, D, W. J. L. I. W. M. M. J. B. and Bergamaschi, P. (2002). Isotope measurement techniques for atmospheric methane.

Milkov, A. V. (2011). Worldwide distribution and significance of secondary microbial methane formed during petroleum biodegradation in conventional reservoirs, *Organic Geochemistry* **42**(2): 184–207.

Mook, W. G. (2000). *Environmental Isotopes in the Hydrological Cycle Vol 1.indd*.

Myhre (2014). Anthropogenic and natural radiative forcing, *in* I. P. o. C. Change (ed.), *Climate Change 2013 – The Physical Science Basis*, Cambridge University Press, pp. 659–740.

NASA Worldview (2022). Nasa worldview.
URL: *https://worldview.earthdata.nasa.gov/*

Nickl, A.-L. (2022). *Numerical simulation of CH4 and its stable isotopologues on regional and global scale*, Dissertation, TUM School of Life Sciences, München.
URL: *https://mediatum.ub.tum.de/?id=1634302*

Nisbet, E. G., Dlugokencky, E. J., Manning, M. R., Lowry, D., Fisher, R. E., France, J. L., Michel, S. E., Miller, J. B., White, J. W. C., Vaughn, B., Bousquet, P., Pyle, J. A., Warwick, N. J., Cain, M., Brownlow, R., Zazzeri, G., Lanoisellé, M., Manning, A. C., Gloor, E., Worthy, D. E. J., Brunke, E.-G., Labuschagne, C., Wolff, E. W. and Ganesan, A. L. (2016). Rising atmospheric methane: 2007-2014 growth and isotopic shift, *Global Biogeochemical Cycles* **30**(9): 1356–1370.

Pataki, D. E., Ehleringer, J. R., Flanagan, L. B., Yakir, D., Bowling, D. R., Still, C. J., Buchmann, N., Kaplan, J. O. and Berry, J. A. (2003). The application and interpretation of keeling plots in terrestrial carbon cycle research, *Global Biogeochemical Cycles* **17**(1).

Picarro Inc. (2021). Picarro g2210-i certificate of compliance.

Picarro Inc. (2022). Cavity ring-down spectroscopy (crds).
URL: *https://www.picarro.com/company/technology/crds*

Picarro Inc. (ed.) (2020). *Picarro G2210-i*.

Prather, M. J., Holmes, C. D. and Hsu, J. (2012). Reactive greenhouse gas scenarios: Systematic exploration of uncertainties and the role of atmospheric chemistry, *Geophysical Research Letters* **39**(9).

Quay, P., Stutsman, J., Wilbur, D., Snover, A., Dlugokencky, E. and Brown, T. (1999). The isotopic composition of atmospheric methane, *Global Biogeochemical Cycles* **13**(2): 445–461.

Ravishankara, A. R. (1988). Kinetics of radical reactions in the atmospheric oxidation of ch4, *Annual Review of Physical Chemistry* **39**(1): 367–394.

Rella, C. (2010). Accurate greenhouse gas measurements in humid gas streams using the g1301 carbon dioxide / methane / water vapor gas concentration analyzer - g1301.

Rella, C. W., Hoffnagle, J., He, Y. and Tajima, S. (2015). Local- and regional-scale measurements of ch₄, d¹³ch₄, and c₂h₆ in the uintah basin using a mobile stable isotope analyzer, *Atmospheric Measurement Techniques* **8**(10): 4539–4559.

Rigby, M., Montzka, S. A., Prinn, R. G., White, J. W. C., Young, D., O'Doherty, S., Lunt, M. F., Ganesan, A. L., Manning, A. J., Simmonds, P. G., Salameh, P. K., Harth, C. M., Mühle, J., Weiss, R. F., Fraser, P. J., Steele, L. P., Krummel, P. B., McCulloch, A. and Park, S. (2017). Role of atmospheric oxidation in recent methane growth, *Proceedings of the National Academy of Sciences of the United States of America* **114**(21): 5373–5377.

Saunois, M., Stavert, A. R., Poulter, B., Bousquet, P., Canadell, J. G., Jackson, R. B., Raymond, P. A., Dlugokencky, E. J., Houweling, S., Patra, P. K., Ciais, P., Arora, V. K.,

Bastviken, D., Bergamaschi, P., Blake, D. R., Brailsford, G., Bruhwiler, L., Carlson, K. M., Carrol, M., Castaldi, S., Chandra, N., Crevoisier, C., Crill, P. M., Covey, K., Curry, C. L., Etiope, G., Frankenberg, C., Gedney, N., Hegglin, M. I., Höglund-Isaksson, L., Hugelius, G., Ishizawa, M., Ito, A., Janssens-Maenhout, G., Jensen, K. M., Joos, F., Kleinen, T., Krummel, P. B., Langenfelds, R. L., Laruelle, G. G., Liu, L., Machida, T., Maksyutov, S., McDonald, K. C., McNorton, J., Miller, P. A., Melton, J. R., Morino, I., Müller, J., Murguia-Flores, F., Naik, V., Niwa, Y., Noce, S., O'Doherty, S., Parker, R. J., Peng, C., Peng, S., Peters, G. P., Prigent, C., Prinn, R., Ramonet, M., Regnier, P., Riley, W. J., Rosentreter, J. A., Segers, A., Simpson, I. J., Shi, H., Smith, S. J., Steele, L. P., Thornton, B. F., Tian, H., Tohjima, Y., Tubiello, F. N., Tsuruta, A., Viovy, N., Voulgarakis, A., Weber, T. S., van Weele, M., van der Werf, G. R., Weiss, R. F., Worthy, D., Wunch, D., Yin, Y., Yoshida, Y., Zhang, W., Zhang, Z., Zhao, Y., Zheng, B., Zhu, Q., Zhu, Q. and Zhuang, Q. (2020). The global methane budget 2000–2017, *Earth System Science Data* **12**(3): 1561–1623.

Schaefer, H., Mikaloff Fletcher, S. E., Veidt, C., Lassey, K. R., Brailsford, G. W., Bromley, T. M., Dlugokencky, E. J., Michel, S. E., Miller, J. B., Levin, I., Lowe, D. C., Martin, R. J., Vaughn, B. H. and White, J. W. C. (2016). A 21st-century shift from fossil-fuel to biogenic methane emissions indicated by ^{13}ch$_4$, *Science (New York, N.Y.)* **352**(6281): 80–84.

Schwietzke, S., Sherwood, O. A., Bruhwiler, L. M. P., Miller, J. B., Etiope, G., Dlugokencky, E. J., Michel, S. E., Arling, V. A., Vaughn, B. H., White, J. W. C. and Tans, P. P. (2016). Upward revision of global fossil fuel methane emissions based on isotope database, *Nature* **538**(7623): 88–91.

Sherwood, O. A., Schwietzke, S., Arling, V. A. and Etiope, G. (2017). Global inventory of gas geochemistry data from fossil fuel, microbial and burning sources, version 2017, *Earth System Science Data* **9**(2): 639–656.

Skoog, D. A. and Leary, J. J. (1996). *Instrumentelle Analytik*, Springer Berlin Heidelberg, Berlin, Heidelberg.

Stecher, L., Winterstein, F., Dameris, M., Jöckel, P., Ponater, M. and Kunze, M. (2021). Slow feedbacks resulting from strongly enhanced atmospheric methane mixing ratios in a chemistry–climate model with mixed-layer ocean, *Atmospheric Chemistry and Physics* **21**(2): 731–754.

Stolper, D. A., Lawson, M., Davis, C. L., Ferreira, A. A., Santos Neto, E. V., Ellis, G. S., Lewan, M. D., Martini, A. M., Tang, Y., Schoell, M., Sessions, A. L. and Eiler, J. M. (2014). Gas formation. formation temperatures of thermogenic and biogenic methane, *Science (New York, N.Y.)* **344**(6191): 1500–1503.

Stull, R. B. (2015). *Meteorology: For scientists and engineers*, UBC, Vancouver.
URL: *https://www.eoas.ubc.ca/books/Practical*$_M eteorology$

Tohjima, Y., Tominaga, T., Makide, Y. and Fujii, Y. (1991). Determination of methane concentration in air extracted from antarctic ice core samples, *Bulletin of the Chemical Society of Japan* **64**(11): 3457–3459.

Turner, A. J., Frankenberg, C. and Kort, E. A. (2019). Interpreting contemporary trends in atmospheric methane, *Proceedings of the National Academy of Sciences of the United States of America* **116**(8): 2805–2813.

Wahlen M. (1989). Carbon-14 in methane sources and in atmospheric methane: The contribution from fossil carbon.
URL: *https://www.science.org/doi/epdf/10.1126/science.245.4915.286*

Wallace, J. M. and Hobbs, P. V. (2008). *Atmospheric science: An introductory survey*, Vol. 92 of *International geophysics series*, 2. ed., [2. repr.] edn, Academic Press, Amsterdam and Heidelberg.

Werner, R. A. and Brand, W. A. (2001). Referencing strategies and techniques in stable isotope ratio analysis, *Rapid communications in mass spectrometry : RCM* **15**(7): 501–519.

Winterstein, F., Tanalski, F., Jöckel, P., Dameris, M. and Ponater, M. (2019). Implication of strongly increased atmospheric methane concentrations for chemistry–climate connections, *Atmospheric Chemistry and Physics* **19**(10): 7151–7163.

Worden, J. R., Bloom, A. A., Pandey, S., Jiang, Z., Worden, H. M., Walker, T. W., Houweling, S. and Röckmann, T. (2017). Reduced biomass burning emissions reconcile conflicting estimates of the post-2006 atmospheric methane budget, *Nature communications* **8**(1): 2227.

Wrubleski, D., Badiou, P. and Goldsborough, G. (2016). Coastal wetlands of manitoba's great lakes (canada), *in* C. M. Finlayson, G. R. Milton, R. C. Prentice and N. C. Davidson (eds), *The Wetland Book*, Springer Netherlands, Dordrecht, pp. 1–15.

Xue, J., Leung, Y. and Ma, J.-H. (2015). High-order taylor series expansion methods for error propagation in geographic information systems, *Journal of Geographical Systems* **17**(2): 187–206.

Zhang, Z., Poulter, B., Knox, S., Stavert, A., McNicol, G., Fluet-Chouinard, E., Feinberg, A., Zhao, Y., Bousquet, P., Canadell, J. G., Ganesan, A., Hugelius, G., Hurtt, G., Jackson, R. B., Patra, P. K., Saunois, M., Höglund-Isaksson, L., Huang, C., Chatterjee, A. and Li, X. (2022). Anthropogenic emission is the main contributor to the rise of atmospheric methane during 1993-2017, *National science review* **9**(5): nwab200.

Acknowledgements

The results of this work would have been unthinkable without the energetic support of many colleagues. I would like to thank Prof. Martin Dameris for supervising my work and his constructive feedback during the phase of writing. My special thanks go to Dr. Alina Fiehn, who was my supervisor at the DLR, familiarized myself with the subject and was always available for questions despite her maternity leave. In addition, my best thanks go to Paul Stock and Michael Lichtenstern, for the great and instructive help regarding instrument setup and in the laboratory and to Dr. Anke Roiger, who was always interested and supported me in many ways. I am grateful for the comments and feedback from Magdalena Pühl. A big thank goes to my ATS campaign colleagues, Michael Lichtenstern, Dr. Helmut Ziereis, Dr. Friedemann Reum and furthermore to Dr. Michal Galkowski (MPI Jena), who gave me great scientific support during and after CoMet 2.0. Thanks to the entire CoMet team for a marvelous campaign time that I look back on fondly!

Declaration of authorship

I hereby declare that the report submitted is my own unaided work. All direct or indirect sources used are acknowledged as references. I am aware that the Thesis in digital form can be examined for the use of unauthorized aid and in order to determine whether the report as a whole or parts incorporated in it may be deemed as plagiarism. For the comparison of my work with existing sources I agree that it shall be entered in a database where it shall also remain after examination, to enable comparison with future Theses submitted. Further rights of reproduction and usage, however, are not granted here. This paper was not previously presented to another examination board and has not been published.

Location, date

Name